ABSTRACT

MULTIFUNCTIONAL REACTIVE NANOCOMPOSITE MATERIALS

by
Demitrios Stamatis

Many multifunctional nanocomposite materials have been developed for use in propellants, explosives, pyrotechnics, and reactive structures. These materials exhibit high reaction rates due to their developed reaction interfacial area. Two applications addressed in this work include nanocomposite powders prepared by arrested reactive milling (ARM) for burn rate modifiers and reactive structures. In burn rate modifiers, addition of reactive nanocomposite powders to aluminized propellants increases the burn rate of aluminum and thus the overall reaction rate of an energetic formulation. Replacing only a small fraction of aluminum by $8Al{\cdot}MoO_3$ and $2B{\cdot}Ti$ nanocomposite powders enhances the reaction rate with little change to the thermodynamic performance of the formulation; both the rate of pressure rise and maximum pressure measured in the constant volume explosion test increase.

For reactive structures, nanocomposite powders with bulk compositions of $8Al{\cdot}MoO_3$, $12Al{\cdot}MoO_3$, and $8Al{\cdot}3CuO$ were prepared by ARM and consolidated using a uniaxial die. Consolidated samples had densities greater than 90% of theoretical maximum density while maintaining their high reactivity. Pellets prepared using $8Al{\cdot}MoO_3$ powders were ignited by a CO_2 laser. Ignition delays increased at lower laser powers and greater pellet densities. A simplified numerical model describing heating and thermal initiation of the reactive pellets predicted adequately the observed effects of both laser power and pellet density on the measured ignition delays.

To investigate the reaction mechanisms in nanocomposite thermites, two types of nanocomposite reactive materials with the same bulk compositions $8Al\cdot MoO_3$ were prepared by different methods. One of the materials was manufactured by ARM and the other, so called metastable interstitial composite (MIC), by mixing of nano-scaled individual powders. Clear differences in the low-temperature redox reactions, well-detectable by differential scanning calorimetry (DSC), were established between MIC and ARM-prepared materials. However, the materials behaved similarly to each other in the ignition experiments. It is proposed that the ignition of both MIC and ARM-prepared materials at the same temperature can be explained by a thermodynamically driven transformation of a protective amorphous alumina into a crystalline polymorph.

Low temperature redox reactions in ARM-prepared Al-CuO nanocomposites were characterized using DSC and isothermal microcalorimetry. The results were interpreted using a Cabrera-Mott reaction model. Simultaneous processing of both experimental data sets identified the parameters for the respective Cabrera-Mott kinetics. The low temperature kinetic model was coupled with a multi-step oxidation model describing diffusion-controlled growth of amorphous and γ-Al_2O_3 polymorphs. The kinetic parameters for the multistep oxidation model from previous research were adjusted based on DSC measurements. The combined heterogeneous reactions model was used to interpret results of ignition experiments. It is proposed that the heterogeneous reactions considered serve as ignition triggers and ensuing gas release processes contributes to additional heat release and temperature runaway.

MULTIFUNCTIONAL REACTIVE NANOCOMPOSITE MATERIALS

by
Demitrios Stamatis

A Dissertation
Submitted to the Faculty of
New Jersey Institute of Technology
in Partial Fulfillment of the Requirements for the Degree of
Doctor of Philosophy in Chemical Engineering

Otto H. York Department of
Chemical, Biological, and Pharmaceutical Engineering

August 2011

APPROVAL PAGE

MULTIFUNCTIONAL REACTIVE NANOCOMPOSITE MATERIALS

Demitrios Stamatis

Dr. Edward L. Dreizin, Thesis Advisor Date
Professor of Chemical Engineering, NJIT

Dr. Rajesh Dave, Committee Member Date
Distinguished Professor of Chemical Engineering, NJIT

Dr. Norman Loney, Committee Member Date
Professor of Chemical Engineering, NJIT

Dr. Robert Barat, Committee Member Date
Professor of Chemical Engineering, NJIT

Dr. Joel Carney, Committee Member Date
Senior Research Scientist, NSWC, Indian Head

BIOGRAPHICAL SKETCH

Author: Demitrios Stamatis

Degree: Doctor of Philosophy

Date: August 2011

Undergraduate and Graduate Education:

- Doctor of Philosophy in Chemical Engineering,
  New Jersey Institute of Technology, Newark, NJ 2011
- Master of Science in Mechanical Engineering,
  New Jersey Institute of Technology, Newark, NJ 2008
- Bachelor of Science in Mechanical Engineering,
  New Jersey Institute of Technology, Newark, NJ 2006

Major: Chemical Engineering

Presentations and Publications:

D. Stamatis, E. L. Dreizin, "Thermal Initiation of Consolidated Reactive Nanocomposite Powders," *New Trends in Research of Energetic Materials*, Pardubice, Czech Republic, **April 2011**.

D. Stamatis, E. L. Dreizin, "Thermal Initiation of Consolidated Nanocomposite Thermite Powders," *AIAA Annual Sciences Meeting*, Orlando, FL, **January 2011**.

D. Stamatis, E. L. Dreizin, "Thermal Initiation of Consolidated Reactive Nanocomposite Materials," *American Institute of Chemical Engineers Annual Meeting*, Salt Lake City, UT, **November 2010**.

D. Stamatis, E. L. Dreizin, P. Redner, "Preparation and characterization of Consolidated Samples of Reactive Nanocomposite Materials," *Central States Section of the Combustion Institute Technical Meeting,* Champaign, IL, **March 2010**.

D. Stamatis, A. Ermoline, E. L. Dreizin, "Ignition of Consolidated Reactive Nanocomposite Powders," *American Institute of Chemical Engineers Annual Meeting*, Nashville, TN, **November 2009**.

D. Stamatis, X. Zhu, A. Ermoline, M. Schoenitz, E. L. Dreizin, "Consolidation of Reactive Nanocomposite Powders," *45th AIAA/ASME/SAE/ASEE Joint Propulsion Conference and Exhibit*, Denver, CO, **August 2009**.

D. Stamatis, X. Zhu, M. Schoenitz, E. L. Dreizin, "Preparation and Testing of Consolidated Reactive Materials," *National Capital Region Energetics Symposium*, La Plata, MD, **April 2009**.

D. Stamatis, X. Jiang, E. Beloni, E. L. Dreizin, "Aluminum Burn Rate Modifiers Based on Reactive Nanocomposite Powders," *American Institute of Chemical Engineers Annual Meeting*, Philadelphia, PA, **November 2008**.

D. Stamatis, Z. Jiang, V. K. Hoffmann, M. Schoenitz, E. L. Dreizin, "Fully Dense Al-Rich AlCuO Nanocomposite Powders for Energetic Formulations," *44th AIAA/ASME/SAE/ASEE Joint Propulsion Conference and Exhibit*, Hartford, CT, **July 2008**.

D. Stamatis, Z. Jiang, V. K. Hoffmann, M. Schoenitz, E. L. Dreizin, "Fully Dense Al-Rich AlCuO Nanocomposite Powders," *Gordon Research Conference: Energetic Materials*, Tilton, NH, **June 2008**.

D. Stamatis, E. L. Dreizin, "Nanocomposite Powders as Burn Rate Modifiers," *Annual Provost Student Research Showcase,* Newark, NJ, **April 2008**.

D. Stamatis, E. L. Dreizin, "Fully Dense Al-CuO Nanocomposite Powders for Energetic Formulations," *AIAA International Student Conference*, Reno, NV, **January 2008**.

D. Stamatis, Z. Jiang, V. K. Hoffmann, M. Schoenitz, E. L. Dreizin, "Fully Dense AlCuO Nanocomposite Powders for Energetic Formulations," *American Institute of Chemical Engineers Annual Meeting*, Salt Lake City, UT, **November 2007**.

D. Stamatis, E. L. Dreizin, "Fully Dense AlCuO Nanocomposite Powders for Energetic Formulations," *AIAA Region 1-NE Student Conference*, Cambridge, Massachusetts, **April 2007**.

D. Stamatis, E.L. Dreizin, K. Higa, "Thermal Initiation of Al·MoO_3 Nanocomposite Materials Prepared by Different Methods," *Journal of Propulsion and Power*, **2011**.

P. Dupiano, D. Stamatis, E.L. Dreizin, "Hydrogen Production by Reacting Water with Mechanically Milled Composite Aluminum-Metal Oxide Powders," *International Journal of Hydrogen Energy*, 36, **2011**.

D. Stamatis, E.L. Dreizin, "Thermal Initiation of Consolidated Nanocomposite Thermites," *Combustion and Flame*, 158, **2011**.

D. Stamatis, X. Zhu, M. Schoenitz, E.L. Dreizin, P. Redner, "Consolidation and Mechanical Properties of Reactive Nanocomposite Powders," *Powder Technology*, 208, **2011**.

D. Stamatis, X. Jiang, E. Beloni, E.L. Dreizin, "Aluminum Burn Rate Modifiers Based on Reactive Nanocomposite Powders," *Propellants, Explosives, Pyrotechnics*, 35, **2010**.

D. Stamatis, P. Redner, E.L. Dreizin, "Preparation and Characterization of Consolidated Samples of Reactive Nanocomposite Materials," *Technical Meeting of the Central States Section of the Combustion Institute Conference Proceedings*, **2010**.

D. Stamatis, X. Zhu, A. Ermoline, M. Schoenitz, E.L. Dreizin, "Consolidation of Reactive Nanocomposite Powders," *45th AIAA/ASME/SAE/ASEE Joint Propulsion Conference and Exhibit Conference Proceedings*, **2009**.

D. Stamatis, Z. Jiang, V.K. Hoffmann, M. Schoenitz, E.L. Dreizin, "Fully Dense Al-Rich Al-CuO Nanocomposite Powders for Energetic Formulations," *Combustion Science and Technology,* 181, **2009**.

D. Stamatis, X. Jiang, E. Beloni, E.L. Dreizin, "Aluminum Burn Rate Modifiers Based on Reactive Nanocomposite Powders," *AIChE Annual Meeting Conference Proceedings*, **2008**.

D. Stamatis, Z. Jiang, V.K. Hoffmann, M. Schoenitz, E.L. Dreizin, "Fully Dense, Aluminum-rich Al-CuO Nanocomposite Powders for Energetic Formulations," *44th AIAA/ASME/SAE/ASEE Joint Propulsion Conference and Exhibit Conference Proceedings*, **2008**.

D. Stamatis, V.K. Hoffmann, M. Schoenitz, E.L. Dreizin, "Fully Dense, Aluminum-rich Al-CuO Nanocomposite Powders for Energetic Formulations," *AIChE Annual Meeting Conference Proceedings*, **2007**.

Dedicated to my brother and parents.

ACKNOWLEDGMENT

First of all, I would like to express my sincere gratitude to Dr. Edward Dreizin for being an excellent advisor and mentor during my graduate studies. His tireless efforts to ensure the success of my research as well as guiding it in the right direction are deeply appreciated.

I would like to give special thanks to my committee members, Dr. Rajesh Dave, Dr. Norman Loney, Dr. Robert Barat, and Dr. Joel Carney for their interest in my work and their participation in my defense committee. Also, I would like to thank Dr. Mirko Schoenitz for helping me in many parts of my research, particularly in many of the material characterization work. I learned a lot about material characterization working with him. Thanks go to Dr. Alexandre Ermoline for patiently working with me and for his important contributions to my research.

Special recognition is deserved for Vern Hoffmann and the rest of my colleagues in Dr. Dreizin's group, Dr. Robert Gill and Dr. Salil Mohan, for their friendly advice and help. Vern's vast laboratory experience was of great value. My fellow PhD students Ervin Beloni, Priya Santhanam, Shasha Zhang, Shashank Vummidi, Yasmine Aly, Carlo Badiola, Paul Dupiano, Bing Wang, and Rayon Williams, also deserve recognition for not only being helpful in my research but also by being friends and making for a wonderful working environment.

Finally, I would like to acknowledge my sponsors, DTRA, RDECOM-ARDEC, Picatinny, US Edwards Airforce Base, and The Emil Beuhler Perpetual Trust, who helped fund this work and support my graduate studies.

TABLE OF CONTENTS

TABLE OF CONTENTS
(Continued)

Chapter **Page**

TABLE OF CONTENTS
(Continued)

Chapter **Page**

TABLE OF CONTENTS
(Continued)

Chapter **Page**

TABLE OF CONTENTS
(Continued)

LIST OF TABLES

Table **Page**

LIST OF FIGURES

LIST OF FIGURES
(Continued)

LIST OF FIGURES
(Continued)

LIST OF FIGURES
(Continued)

LIST OF FIGURES
(Continued)

LIST OF FIGURES
(Continued)

LIST OF FIGURES
(Continued)

NOMENCLATURE

A	Surface area of volume element
A_r	Reactive interface area of a particle
a	Laser radiation absorption coefficient
a	Constant in linear function describing the Mott potential term E_2
b	Coefficient in linear function describing the Mott potential term E_2
C_{am}	Preexponent for thermally activated diffusion term describing oxidative growth of amorphous Al_2O_3
C_{γ}	Preexponent for thermally activated diffusion term describing oxidative growth of γ–Al_2O_3
C_v	Constant volume heat capacity
c_{am}	Coefficient for reaction progress for growth of amorphous Al_2O_3
c_{γ}	Coefficient for reaction progress for growth of γ–Al_2O_3
E_1	Activation energy of Cabrera-Mott reaction
E_2	Mott potential term from Cabrera-Mott reaction
E_a	Activation energy used in Arrhenius term
E_{am}	Activation energy for thermally activated diffusion term describing oxidative growth of amorphous Al_2O_3
$E_{am\rightarrow\gamma}$	Activation energy for the amorphous to γ–Al_2O_3 polymorphic phase transformation
E_{γ}	Activation energy for thermally activated diffusion term describing oxidative growth of γ–Al_2O_3
$F_{am\rightarrow\gamma}$	Preexponent the amorphous to γ–Al_2O_3 polymorphic phase transformation
Fo	Fourier number
f_{am}	Progress function for growth of amorphous Al_2O_3 by diffusion

f_{γ}	Progress function for growth of $\gamma-Al_2O_3$ by diffusion
h	Convection heat transfer coefficient
h_0	Initial thickness of amorphous Al_2O_3interfacial layer
h_{am}	Thickness of amorphous Al_2O_3 layer
h_{γ}	Thickness of $\gamma-Al_2O_3$ layer
h_{γ}^{min}	Minimum thickness of $\gamma-Al_2O_3$ for which its diffusion resistance is computed using the literature data for polymorphic $\gamma-Al_2O_3$
i	Iteration number used in numerical model
K	Arrhenius term in the Cabrera-Mott oxidation equation
$K_{am\rightarrow\gamma}$	Exponential coefficient used to describe the amorphous to $\gamma-Al_2O_3$ polymorphic phase transformation
k_b	Boltzmann constant
k_0	Thermal conductivity
k_0	Preexponent for the Cabrera-Mott reaction
L	Total length of a pellet
l	Axial position along a pellet
m	Mass of volume element
m_p	Mass of particle
m_{Al2O3}	Mass of alumina formed
m_{am}^{CM}	Mass of amorphous Al_2O_3 formed due to Cabrera-Mott reaction
m_{am}^{Diff}	Mass of amorphous Al_2O_3 formed due to oxidation by diffusion
$m_{am\rightarrow\gamma}^{tr}$	Mass of $\gamma-Al_2O_3$ formed due to polymorphic phase transformation
m_{CuO}^{cum}	Cumulative mass of CuO consumed during reaction
m_{CuO}^{ini}	Initial mass of CuO in the core
m_{γ}^{ox}	Mass of $\gamma-Al_2O_3$ formed due to oxidation by diffusion

Q_{chem}	Chemical heat flow term
Q_{cond}	Conductive heat flow term
Q_{conv}	Convective heat flow term
Q_{laser}	Laser radiation heat flow term
Q_{rad}	Radiation loss heat flow term
q_0''	Laser power flux
R	Universal gas constant
r_1	Radius of core
r_2	Radius of shell
r_{10}	Initial radius of core
r_{20}	Initial radius of shell
r_{am}	Radius of amorphous oxide layer
$r_{am,0}$	Initial radius of amorphous oxide layer
r_{core}	Radius of core
$r_{core,0}$	Initial radius of core
r_γ	Radius of $\gamma-Al_2O_3$ layer
T	Temperature
T_∞	Environment temperature
t	Time
$v_{am\rightarrow\gamma}$	Amorphous to $\gamma-Al_2O_3$ transformation velocity
Z	Preexponent in Arrhenius term
Z^*	Gravimetric preexponent in Arrhenius term
z	Ratio of the oxide volume formed over the volume of the oxidizer consumed per reaction of one oxygen ion
α	Global reaction progress

α^*	Global reaction process at the onset of $\gamma-Al_2O_3$ growth
α_{am}	Reaction progress for growth of amorphous Al_2O_3 by diffusion
α_{th}	Thermal diffusivity of nanocomposite particle
α_{γ}	Reaction progress for growth of γ-Al_2O_3 by diffusion
ΔH_{Al2O3}	Enthalpy of formation per mass of alumina
Δt	Time step used in numerical model
ε	Surface emissivity of pellet surface
ρ_{am}	Density of amorphous Al_2O_3
ρ_{γ}	Density of $\gamma-Al_2O_3$
σ	Stefan-Boltzmann constant
χ	Number of CuO inclusion per unit of mass in the nanocomposite

CHAPTER 1

INTRODUCTION

1.1 Background

Various multifunctional nanocomposite materials are currently under development as potential components of different energetic formulations, from propellants to explosives, pyrotechnics, and reactive structures. [1-10] The advantages anticipated from such materials are primarily due to a very developed reactive surface that facilitates rapid initiation of the exothermic reaction and results in a nearly adiabatic reaction temperature. The main process used to prepare the nanocomposite materials used in this research is Arrested Reactive Milling (ARM). [1, 7-9] ARM is based on high energy mechanical milling whereby regular micron-sized powders capable of highly exothermic reaction are ball milled together. The mechanically initiated exothermic reaction is prevented by arresting (or stopping) the milling when the desired powder refinement is achieved. The product is a metastable, fully dense, reactive nanocomposite powder. The mixing takes place at the nanoscale level while the particle sizes are in the micron-range. Therefore, each micron-sized particle represents a nanocomposite structure of two or more reactive components.

In addition to the ARM-prepared powders, nanocomposite materials prepared by ultrasonically mixing nanopowders, commonly referred to as metastable interstitial composites (MIC), were used in parts of this research. [10]

Many different reactive nanocomposite materials have been prepared at New Jersey Institute of Technology using ARM and mechanical alloying as listed in Table 1.1. Note that each composition has its own set of properties making it of interest for a specific range of applications. For example, Al-based thermites with Fe_2O_3 as an oxidizer combine a relatively high density and a capability of rapid gasless reaction. Such materials also produce molten iron as a product, making them of interest to joining applications.

Table 1.1 Reactive Nanomaterials Prepared at NJIT

Nanocomposite Thermites							
Fuel	Oxidizer						
	Fe_2O_3	MoO_3	CuO	Bi_2O_3	WO_3	SrO_2	$NaNO_3$
Al	x*	x*	x*	x*	x	X	x**
Mg		x	x				x**
$Al_{0.5}Mg_{0.5}$							x**
MgH_2		x	x				
Si		x	x	x			
Zr		x	x	x			x**

Reactive Metal-Metalloid composites	
B	Reactive metals: Ti, Zr, Hf

Nanostructured Al-based alloys	
Al	Alloying components: Mg, MgH_2, Ti, Li, Zr, W, Hf, Fe, Ni, Zn, C, I

* Metal-rich nanocomposites have been synthesized
** Oxidizer-rich nanocomposites have been synthesized

The Al-based thermites with MoO_3 used as an oxidizer have some of the highest reaction enthalpies among all the thermite compositions. They also have a relatively high density and low gas production upon reaction. These materials are of interest as additives to solid propellants and enhanced blast explosives. The Al-based thermite with CuO as an oxidizer produces boiling Cu as a combustion product. Thus, a readily condensable gas is produced altering regime of combustion of such material and making it of interest for weapons systems when a gas release is desired, but the effect of gas release should be observed only at a very short distance from the weapon, e.g., to minimize collateral effects. Following the sequence of oxides, Bi_2O_3, used as an oxidizer in a thermite composition, similarly to CuO, produces a condensable vapor of boiling Bi. However, that gas condenses at a much lower temperature than Cu, so that the effect of gas release is more far-reaching than for CuO. These materials have a smaller reaction enthalpy compared to Al-MoO_3 thermites, but substantially increased reaction rates, making them of interest for primers and related pyrotechnic systems. The thermite with WO_3 as an oxidizer has a very high density and that with SrO_2 used as an oxidizer produces a useful optical emission upon combustion, so it can be used for decoy flares and other pyrotechnic components. Using $NaNO_3$ as an oxidizer for Al produces a nanocomposite material capable of permanent gas generation upon combustion. Such materials are of interest for reactive darts, reactive bullets, and other devices where ballistic and pyrotechnic effects need to be combined. Metal-metalloid compositions do not require external oxidizer and can react anaerobically. At the same time, when the eternal oxidizer is present, these materials follow on to oxidize releasing an even greater heat. Finally, mechanically alloyed compositions offer a fine tuning of the metal burn rates and have reaction enthalpies similar to those of the pure metal fuels.

As a group, these materials combine high reactivity with interesting thermal and mechanical properties, making them good candidates for development of multifunctional reactive materials. One of the functions will always be associated with the materials' potential for highly exothermic reactions. The other functions can take advantage of the high density (for ballistic and other applications), high heat capacity (for thermal stabilization), high strength (for mechanical components), capability to release permanent or condensable gases, capabilities to contain biocidal components, etc. Finally, it is worth noting that because of the convenient, micron-sized particle size distribution making these materials easy to handle, they can be readily combined with other metallic and non-metallic materials making multi-scale composite structures with customized and fine-tuned properties.

One potential use for reactive nanocomposites explored in this research is to replace or augment energetic metal powders used as burn rate modifiers. For example, aluminum powders have been used as additives in propellants, pyrotechnics, and explosives. Aluminum has a high enthalpy of combustion but relatively low burn rate. In a solid propellant it also serves as a component with a high specific heat, which prevents temperature instabilities and thus helps to stabilize combustion. Comparatively, aluminum burn rates are lower than those of other solid propellant components such as ammonium perchlorate (or AP), so that the burn rate of the final formulation is difficult to optimize or adjust. In addition, aluminum combustion is not always complete within the motor, so that its combustion efficiency is reduced, especially in smaller scale devices. Complete or partial replacement of aluminum with aluminum-based reactive nanocomposite powders may improve combustion efficiency and increase the overall heat release despite a small reduction in the theoretical combustion enthalpy. Furthermore, such additives are expected to enable an increase in the burn rates for the energetic formulations.

A different potential application for these materials is in reactive structural materials and components. Reactive structural materials are needed to replace common structural components and, at the same time, be capable of a highly exothermic reaction when initiated. Reactive nanocomposite powders prepared by ARM can be consolidated to high densities to achieve characteristics of structural materials while maintaining their inherently high reactivity. Potential applications of such materials include waveshapers and liners of the shaped charges, munitions casings, reactive fragments, and other weapons components.

In all reactive nanocomposite materials, the mass transfer rates and respective reaction rates are increased due to a highly developed interface area between reactive components, typically fuel and oxidizer, but also including metal-metal and metal-metalloid reactive compositions. However, depending on the method used to prepare a nanocomposite material, the nature of interfaces between reactive components can change. Therefore, reaction mechanisms may differ even for materials with nominally the same chemical compositions. Very little is currently known about the types of interfaces formed between reactive components. It is clear that such interfaces will need to be well characterized so that respective heterogeneous reactions can be described quantitatively. Such reaction descriptions are critical for predictions of sensitivity, initiation kinetics, and aging of respective materials.

1.2 Objectives

This research is focused on two specific types of applications of reactive nanocomposite materials and on developing a mechanistic description for heterogeneous reactions driving ignition in nanocomposite thermites prepared by ARM. The experimental and modeling efforts are restricted to a limited set of nanocomposite materials.

The objective for the burn rate modifier work is to use reactive nanocomposite powders as an additive to increase the burn rate of the Al fuel and improve its combustion efficiency in solid propellants.

In the case of reactive structures there are two primary objectives. First, it is desired to show that mechanically sound consolidated bulk shapes can be prepared using ARM-prepared nanocomposite powders. Secondly, it is investigated whether the bulk components consolidated to nearly full densities retained the high reactivity of the starting nanocomposite powders.

The development of the reaction mechanisms driving ignition of nanocomposite powders prepared by different methods is based on a detailed experimental study using different types of materials with the same nominal chemical compositions. The objective is to develop a reaction mechanism to describe the thermally initiated exothermic reactions in the nanocomposite materials at a range of temperatures. The final objective is to implement the developed mechanism into a numerical model capable of describing the initiation behavior of nanocomposite materials subjected to different ignition stimuli.

CHAPTER 2

ALUMINUM BURN RATE MODIFIERS BASED ON NANOCOMPOSITE POWDERS

2.1 Introduction

Aluminum powders have long been used as additives in propellants, pyrotechnics and explosives [11-13]. Aluminum has a high enthalpy of combustion but relatively low burn rate. Addition of reactive nanocomposite powders can increase the burn rate of aluminum and thus the overall reaction rate of the energetic formulation. Replacing only a small fraction of the fuel by a nanocomposite material can enhance the reaction rate with little change to the thermodynamic performance of the formulation. The overall energy outputs from many exothermic reactions employed in such materials, including thermites, intermetallic, and metal-metalloid compositions, are smaller than the benchmark values for aluminum combustion in air or in other practically important oxidizers (e.g., ammonium perchlorate). Thus, replacement of aluminum used as a fuel in most metallized energetic formulations with almost any of the nanocomposite materials currently under development would result in an overall reduction of the theoretical reaction enthalpy. This negative effect may be offset by an increase in the efficiency of metal combustion, so that the overall increase in practical performance is still anticipated. Therefore, the optimized composition would combine the high energetic output with the accelerated reaction rate. An approach discussed in this research suggests that replacing only a fraction of aluminum fuel with a reactive nanocomposite material could result in an acceleration of the ignition kinetics for all metal fuel. Aluminum particles located in vicinity of the igniting reactive nanocomposite particles would be heated more efficiently and ignite sooner. It is anticipated that a relatively small addition of the reactive nanocomposite material would provide a number of localized hot spots within the igniting energetic formulation, which would accelerate ignition of the nearby aluminum particles, which, in turn, will accelerate ignition of their own particles-neighbors. Effectively, the nanocomposite material will serve as a burn rate modifier for an aluminized energetic formulation. The amount of such modifier is expected to be a function of the specific formulation. In this study, the proposed concept is initially explored for aluminum particles burning in a gaseous oxidizer in presence of products of hydrocarbon combustion. Such environments are relevant for both enhanced blast explosives and metallized solid propellants.

2.2 Materials

Reactive nanocomposite powders were prepared by ARM. Samples of three micron-sized, fully dense nanocomposite powders with bulk compositions $2B\cdot Ti$, $8Al\cdot 3CuO$, and $8Al\cdot MoO_3$ were produced using a Retsch 400 PM planetary mill. Further details on the material synthesis are available elsewhere [9, 14]. Typically, the nanocomposite materials consist of micron-sized particles whereas each particle is a fully-dense, three-dimensional composite with characteristic dimension of material mixing of about 100 nm. Commonly, the morphology of the composite is that of inclusions of one component, e.g., B, CuO, or MoO_3, embedded into a matrix of another component such as Ti or Al. In this study, the nanocomposite materials prepared by ARM were added to a spherical aluminum powder, 10 – 14 μm nominal particle size by Alfa Aesar. The mixing of aluminum and nanocomposite powders was performed using a SPEX Certiprep 8000 shaker mill operated without milling balls for three minutes. The particle size distributions for all powders used in this project were measured using a Coulter LS 230

Enhanced Laser Diffraction particle size analyzer. The size distributions and respective volume mean particle sizes for all powders are shown in Figure 2.1.

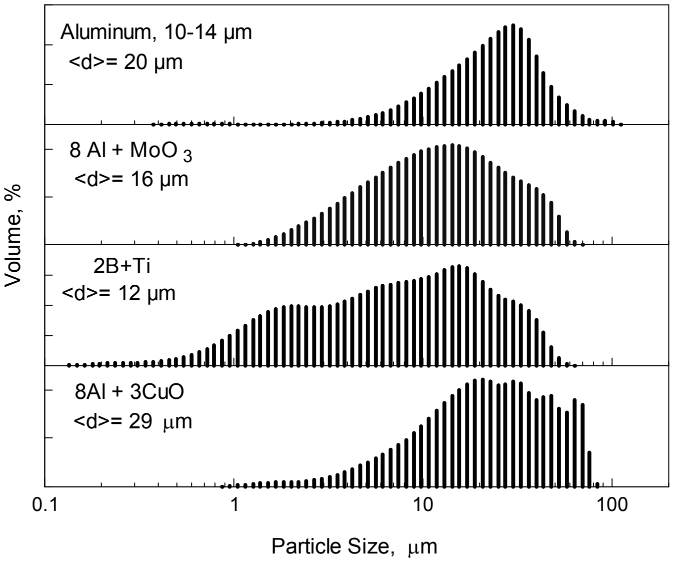

Figure 2.1 Particle size distributions for the different powders used in this project. Volume mean particle sizes are shown for each material.

2.3 Experimental

A common concern for all reactive metal powder additives is their sensitivity to electrostatic discharge (ESD) ignition. All the materials used in this project were tested using a firing test system model 931 by Electro-tech Systems, Inc., according to Mil-1751A standard. Constant Volume Explosion (CVE) experiments were performed with a set of materials including aluminum and aluminum mixed with different amounts of added nanocomposite burn rate modifiers. The details of the CVE experimental methodology and setup are described elsewhere [15 – 17]. Figure 2.2 shows a simplified diagram of the CVE apparatus.

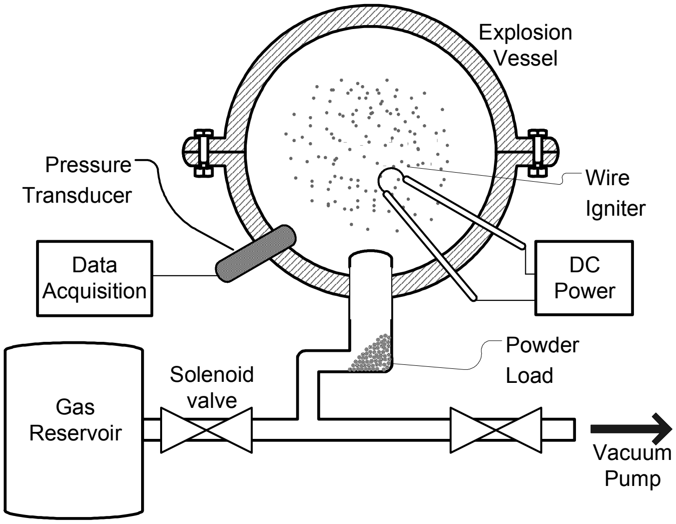

Figure 2.2 Schematic diagram of the constant volume explosion apparatus.

The powders were introduced into a nearly spherical 9.2 liter vessel as an aerosol and ignited at the center of the vessel. The powder load was selected considering results of thermodynamic equilibrium calculations for combustion of aluminum in different gas mixtures used in experiments. It was predicted that the maximum adiabatic flame temperature for the 9.2 liter vessel filled with air occurs at an aluminum load of 2.64 g. Respectively, all experiments were performed with 2.64 g of powder loaded, while both the powder composition and the environment composition were varied. Before the powder was introduced into the vessel, the vessel was evacuated to less than 1 torr. It was then filled with the 171 torr of O_2. The powder was introduced with a blast of a gas mixture typically comprising nitrogen and methane. The blast was produced by opening a solenoid valve connecting the vessel with a 2-gallon gas reservoir filled with nitrogen/methane gas mixture at 4,200 torr. Before each experiment, the gas mixture was prepared by evacuating the gas reservoir and re-filling it with 81.3 to 243.8 torr of methane and the balance of nitrogen. The duration of the gas blast pulse was 200 ms. At the end of the blast, the pressure in the vessel was close to 1 atm. To reduce the turbulence in produced gas powder mixture and mix different gaseous components, the gas blast was followed by a 300 ms waiting period. This wait time was used in multiple previous experiments [15 – 17] and was limited to minimize settling of the aerosolized powders in the gravity field. Because of the initial turbulence induced by the gas blast, this time is expected to be sufficient to fully mix gaseous components and distribute the powder uniformly within the vessel. Finally, the powder was ignited using an electrically heated tungsten wire placed in the center of the vessel. The combustion pressure traces were measured in real time using an American Sensor Technology AST 4700 transducer. The values and the rates of pressure rise produced by the combustion were compared for different powders. Condensed combustion products were collected after each run for subsequent assessment of their compositions using x-ray diffraction (XRD) analysis. After collecting combustion products, the amount of powder trapped in the injector (and not aerosolized) was measured. The vessel was again closed and evacuated. The gas from the reservoir was blasted into the vessel several times so that eventually all residual powder was cleaned off from the injector and introduced into the combustion vessel. This powder was collected and weighed. The results were kept for each experiment and used to estimate the reaction efficiency, as discussed below. The average mass of residual powder was 0.3 g.

In one set of experiments, the oxidizing environment was fixed to nominally include 3% CH_4, 22% O_2, and 75% N_2. The amounts of the nanocomposite powders added to aluminum were 10, 20, and 30 mass %. The gaseous combustion products included water, CO, and CO_2, imitating the environment in actual propellants better than the previous CVE experiments performed in air [15, 16]. The second set of experiments was carried out using a constant mass % of additive for each modifier in the aluminum powder load. The methane concentration varied between 1.5 and 4.5 % while the oxygen concentration remained constant.

2.4 Thermodynamic Equilibrium Calculations

Thermodynamic equilibrium calculations were carried out for pure aluminum and aluminum with different amounts of the nanocomposite additives. The calculations were performed using the NASA chemical equilibrium and applications (CEA) code. A constant volume combustion mode was used. The atmosphere was set at a pressure of 1 atm and composition of 3% CH_4, 22% O_2, and 75% N_2. Amounts of the modifiers used were 10, 20, and 30 mass %. Figure 2.3 shows the maximum pressures and temperatures from the CEA calculations. Pure aluminum exhibits the highest temperature and pressure. Both temperature and pressure decrease as more modifier material is added, but the decrease is relatively small. Based on the calculations, the $8Al+MoO_3$ nanocomposite additive is expected to result in a slightly higher flame temperature than any other additive considered. The differences in the predicted temperatures and pressures for different additives taken at the same mass % are very minor.

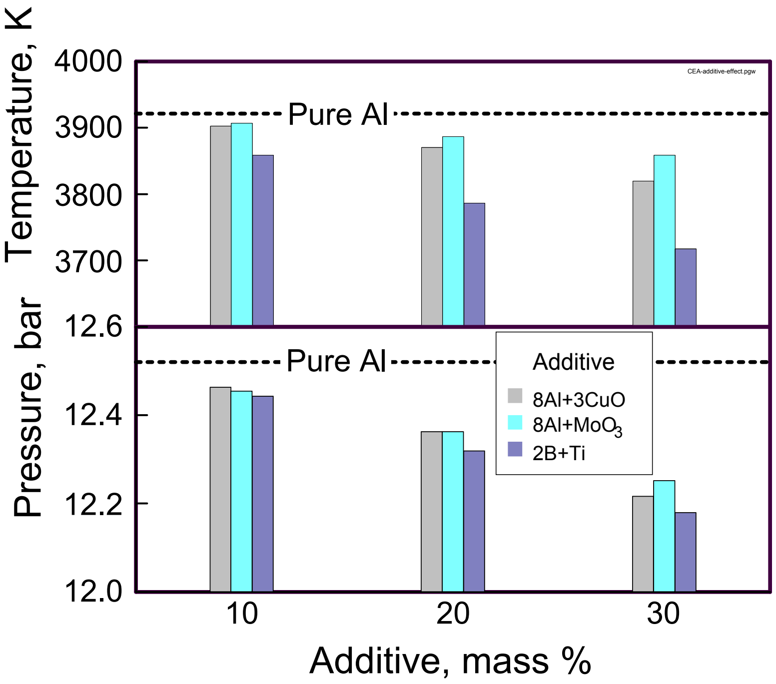

Figure 2.3 Adiabatic flame temperatures and respective pressures predicted by CEA calculations for constant volume combustion of different solid fuels in a fixed environment: 3%CH4, 22% O2; 75% N2, initially at 1 atm. Solid fuels are aluminum with different mass % of burn rate additives.

The effect of gas composition was also considered using the CEA calculations. The pressure and combustion temperatures of the powders in the constant volume combustion were calculated for the amount of modifier fixed at 20 mass %. Combustion atmospheres with 1.5, 3.0, and 4.5 % CH$_4$, constant 22 % O$_2$ and balance of N$_2$ were used. Figure 2.4 shows the calculated values for the flame pressure and temperature. Pure aluminum flames are characterized by both higher temperature and pressure. Comparatively, the differences in the predicted pressures and temperatures for pure Al and for Al with modifiers are quite small. An increase in the combustion pressure is anticipated with increase in the methane concentration for all fuels. Conversely, the flame temperatures decrease with the increasing methane concentration indicating a substantial change in the predicted make-up of the equilibrium combustion products. The predicted pressures and temperatures do not differ much among different modifiers. Both thermite compositions appear to result in slightly higher pressures at greater concentrations of methane compared to the boron-titanium composition, which is predicted to work a bit better for dry environments.

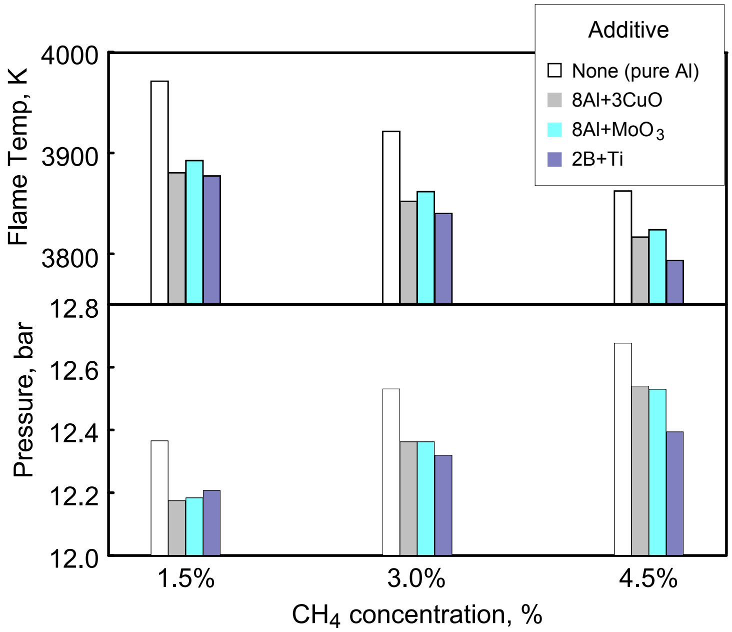

Figure 2.4 Adiabatic flame temperatures and respective pressures predicted by CEA calculations for constant volume combustion of aluminum with 20 wt % of different additives in different gas environments. For each case, 75% N_2 is balanced by O_2 and CH_4 initially at 1 atm.

Finally, the equilibrium calculations were used to predict the compositional make-up of the condensed products anticipated for different burn rate modifiers. Two separate calculations were performed. In the first calculation, products formed at the adiabatic flame temperature were determined. In the second calculation, main species present in the adiabatic combustion products were considered as reagent species initially at the adiabatic flame temperature and pressure. They were equilibrated to room temperature (300 K). This calculation predicted the final pressure in the combustion vessel and the mole fraction of the condensed products present. Figure 2.5 shows the result of these calculations. Consistently with the previous calculation results, the lowest final pressures, and thus the most substantial consumption of the gaseous oxidizers is predicted for the pure Al flames. The increase in the initial concentration of methane, which is an additional fuel, generally results in a decrease in the final pressure. This effect is diminished for pure Al at higher methane concentrations. The main condensed species predicted to be present in the combustion products are listed in Table 2.1.

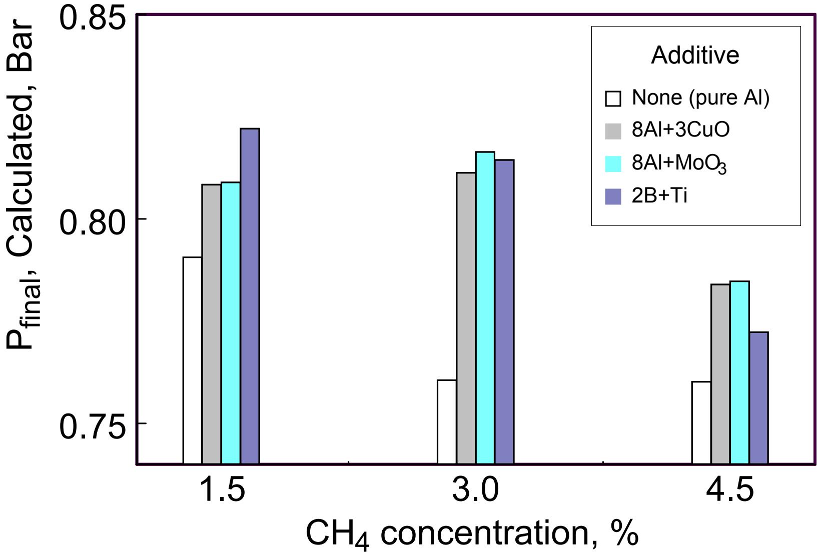

Figure 2.5 Final pressure in the explosion vessel after combustion is completed predicted by a CEA calculation using the adiabatic pressure, temperature, and combustion products as the input and preset to equilibrate to room temperature. For each case, 75% N_2 is balanced by O_2 and CH_4 initially at 1 atm.

Table 2.1 Condensed Combustion Products Predicted by CEA Calculation and Identified by XRD

Species	Calculated	Experimental (XRD)
Al		X
Al_2O_3	X	X
$Al(OH)_3$	X	
Cu	X	
CuO	X	X
Cu_2O		X
$CuAl_2$		X
MoO_3	X	X
MoO_2	X	
B_2O_3	X	X
HBO_2	X	
TiO_2	X	X
C (graphite)	X	

2.5 Results and Discussion

Table 2.2 shows the measured values of the minimum ignition energy (MIE) for each material ignited by an electric spark. According to the standard testing methodology, ignition is registered if individual burning particles are observed. Such particles may or may not be accompanied by a self-sustaining flame.

Table 2.2 Ignition Sensitivity of Materials to Electro-Static Discharge

Material	MIE (mJ)	Self-sustaining flame
Spherical Al 10-14 micron	25.7	No
8Al+3CuO nanocomposite	3.8	Yes
8Al+MoO_3 nanocomposite	<0.8	Yes
2B+Ti nanocomposite	1.2	No
Al (10-14 micron) + 20%(8Al+3CuO) blend	13.2	No
Al (10-14 micron) + 20%(8Al+MoO_3) blend	6.9	No
Al (10-14 micron) + 20%(2B+Ti) blend	1.9	No

It is noted in Table 2.2 whether the spark ignition resulted in a self-sustaining flame, which clearly indicated more sensitive powders. The data indicate that mixing the nanocomposite powders with aluminum results in a powder that is more sensitive than the pure aluminum but substantially less sensitive than the nanocomposite material by itself. In particular, it is worth noting that the flame did not propagate in the powder mixtures, unlike in the individual nanocomposite powders.

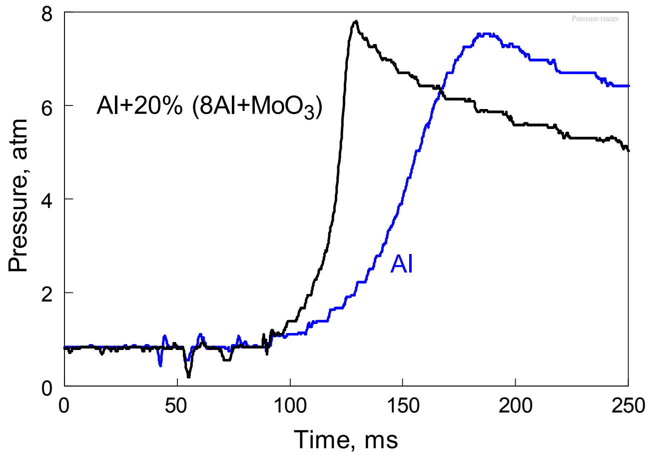

Figure 2.6 Pressure traces from constant volume explosion experiments for pure aluminum powder and aluminum powder with 20 wt % of a nanocomposite additive. The gas environment is 3% CH_4, 22% O_2, and 75% N_2.

Shown in Figure 2.6 are two characteristic pressure traces from the CVE experiment. The measured maximum combustion pressures are substantially lower than those predicted by equilibrium calculations (cf. Figures. 2.3, 2.4). This difference is likely caused by two factors: radiation heat losses and incomplete combustion of the solid fuel. Indeed, in experiments where aluminum flame temperature is measured optically, the temperatures are typically limited to 3000 K, e.g., [18, 19]. At higher temperatures, radiation becomes a very efficient heat loss mechanism for a relatively small flame enclosed in a room temperature metal vessel. As the experimental flame temperatures are reduced, the pressure decreases according to the equation of state, with the effect amplified substantially by the rapid reduction in concentration of the volatile species, such as AlO, Al_2O, AlO_2, as well as other metastable and atomic gas species, such as O, OH, N, NO, etc. The incomplete combustion is primarily due to the fact that a large portion of the flammable mixture remains unconsumed in vicinity of the vessel walls, where the wall quenching effects extend for about 1 cm, i.e., a distance equal to the flame front thickness in the burning aerosol. The flame thickness is readily estimated as the product of the flame speed and the time between the instants the maximum rate of pressure rise and maximum pressure are observed. The flame speed, close to 0.5 m/s, can also be estimated from the measured pressure trace and considering the vessel dimensions. Note that for the spherical vessel used in these experiments, the external layer with thickness of 1 cm contains close to 40 volume % of the initial flammable mixture. Considering nearly adiabatic compression of the unburned mixture by the propagating flame front, the amount of the mixture affected by the wall quenching is increased further. Consistently with the expected limitations on the reaction completeness, unoxidized Al is detected in the combustion products, as shown in Table 2.1. While accurate calculations quantifying the effects of both radiation heat loss and incomplete combustion on the pressure are difficult, qualitatively, the observed systematic difference between the predicted in equilibrium and experimental pressures is hardly surprising.

The aluminum powder with the burn rate modifier additive shows both increased maximum pressure and the rate of pressure rise. The accelerated burn rate was indeed observed for all experiments using nanocomposite powders as burn rate modifiers. However, the maximum measured pressure could be both higher and lower than that measured for pure Al powder.

Initial CVE experiments were carried out to determine the effect of various amounts of modifier as was done in the CEA calculations shown in Figure 2.3. While the targeted initial pressure in the vessel before ignition was always 1 atm, the actual initial pressures varied in the range of .94 – 1.06 atm. To minimize the effect of this initial pressure variation, the results are consistently shown in terms of the measured explosion pressures divided by the measured initial pressures. Figure 2.7 shows respective ratios for the maximum pressures observed in explosions over corresponding values of the initial gas pressures in the vessel for different modifiers at different additive mass percents. Results for the maximum rates of pressure rise, $(dP/dt)_{max}$, are shown in Figure 2.8.

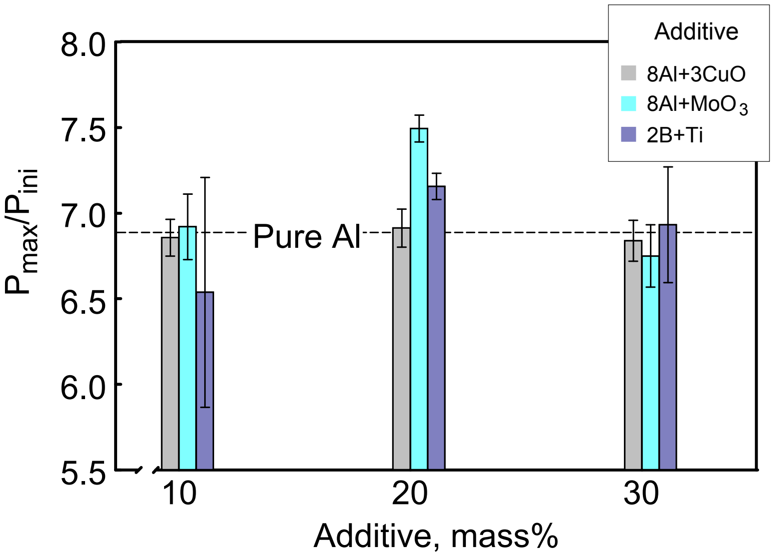

Figure 2.7 Normalized maximum combustion pressure measured in CVE experiments for aluminum powders with varied amounts of fuel additives. The gas environment is fixed at 3% CH_4, 22% O_2, and 75% N_2.

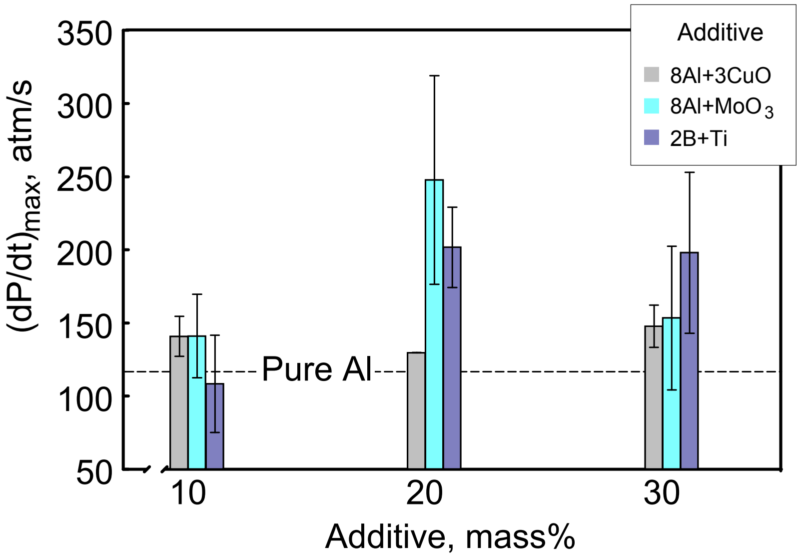

Figure 2.8 Maximum rates of pressure rise measured in CVE experiments for aluminum powders with varied amounts of fuel additives. The gas environment is fixed at 3% CH_4, 22% O_2, and 75% N_2.

The error bars here and below represent the standard deviations among the experimental data points. The maximum rate of pressure rise is generally proportional to the flame speed and serves as an indicator of the burn rate. Dashed lines in both Figures 2.7 and 2.8 indicate respectively the measured values of pressure and the rate of pressure rise for the pure aluminum powder. Unlike the calculated pressures, the experimental pressures for the powders with burn rate modifiers are mostly as high as or higher than that for pure aluminum. Interestingly, the modifier predicted to result in a higher flame temperature, nanocomposite 8Al+MoO_3, results in experimental explosion pressures exceeding those measured for pure aluminum when the additive concentration is less than 30%. The maximum rates of pressure rise shown in Figure 2.8 are all higher for aluminum powders mixed with additives than for the pure aluminum. The most significant improvements in the burn rate are observed for 8Al+MoO_3 and 2B+Ti nanocomposite additives at 20 wt %. The effect is consistently small for 8Al+3CuO.

The effect of methane concentration was studied experimentally while the amount of the burn rate modifier was fixed at 20 wt%, similar to the calculations presented in Figure 2.4. The results for both the maximum pressures and rates of pressure rise are shown in Figure 2.9. The changes in the explosion pressures for the pure aluminum and aluminum with 8Al+3CuO nanocomposite additive are small and the observed trends are similar to those predicted by the equilibrium calculations. Addition of the nanocomposite 8Al+MoO_3 powder results in the explosion pressures exceeding those of the pure Al for all gas compositions. The maximum explosion pressures for aluminum with nanocomposite 2B+Ti additive consistently decrease with an increase in the methane concentration, which is opposite to the trend predicted by the equilibrium calculations (cf. Figure 2.4). For the latter fuel, the maximum explosion pressures are higher than those for pure Al at lower methane concentrations. For all fuels, the rate of combustion proportional to the measured values of $(dP/dt)_{max}$ increase at the increasing methane concentrations. The most substantial improvement over pure aluminum is observed for the fuel with nanocomposite 8Al+MoO_3 powder. The increase in the burn rate is also substantial for the aluminum mixed with nanocomposite 2B+Ti.

The results presented in Figure 2.9 can also be considered in terms of combustion efficiency described based on the direct comparison of the experimental and predicted explosion pressures. Specifically, ratios of the experimental maximum pressures to the respective pressures calculated by CEA code for the same initial conditions (cf. Figure 2.4) are considered as efficiency indicators. To account for the residual powder that was not injected into the vessel, CEA calculations were repeated with the mass of powder reduced according to the experimental data. While the correction for the calculated combustion pressures was relatively small, these corrected pressures were used to estimate the combustion efficiency as shown in Figure 2.10. The trends observed in Figure 2.10 are very similar to those in Figure 2.9.

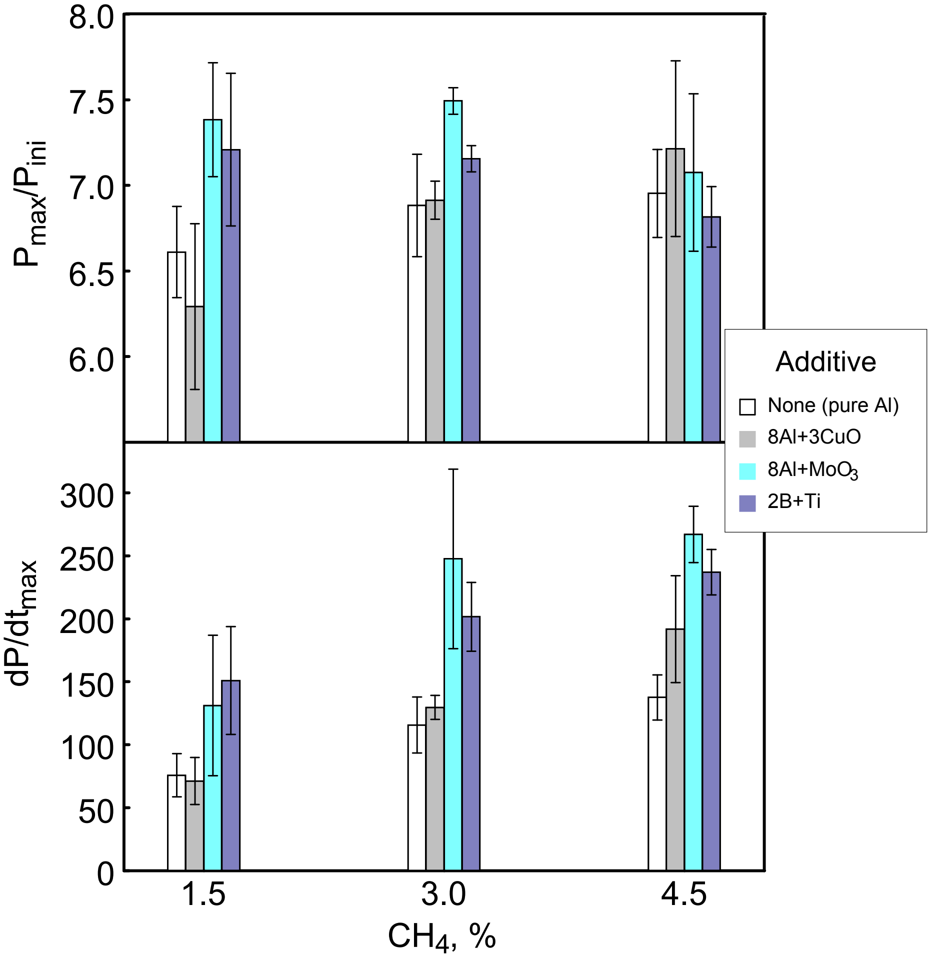

Figure 2.9 Normalized maximum combustion pressures and maximum rates of pressure rise measured in CVE experiments for aluminum powders with 20 wt % of different fuel additives. The gas environments are varied with 1.5, 3, and 4.5 % of CH_4, 22% O_2, and balance of N_2.

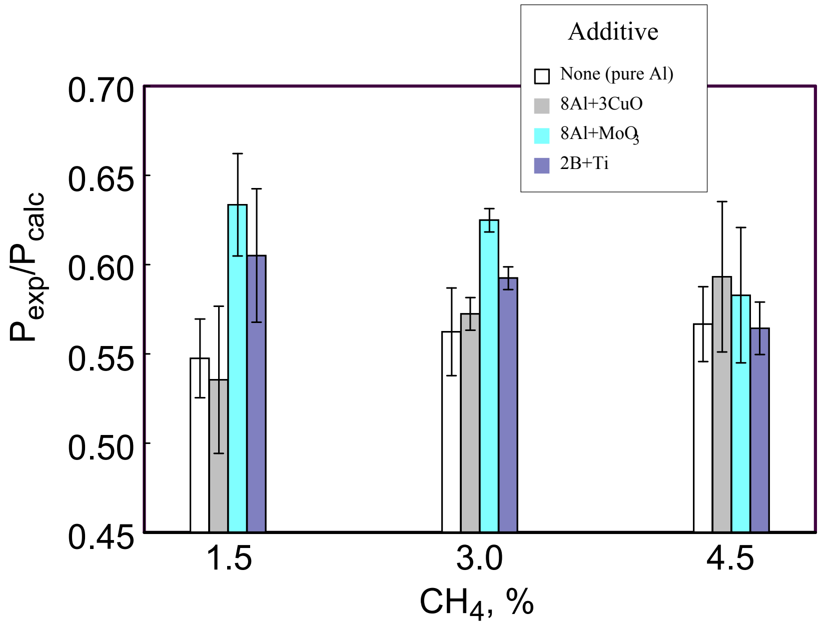

Figure 2.10 Ratios of the experimental maximum pressures to the respective pressures calculated by CEA for the same initial conditions (cf. Figure 2.4, varied oxidizing environments).

The final pressures in the vessel measured after the combustion was completed and the vessel was cooled down to room temperature are indicative of the oxygen consumption. These pressures were compared to the predicted final pressures shown in Figure 2.5. The ratios of the measured over calculated final pressures for different experimental conditions are shown in Figure 2.11.

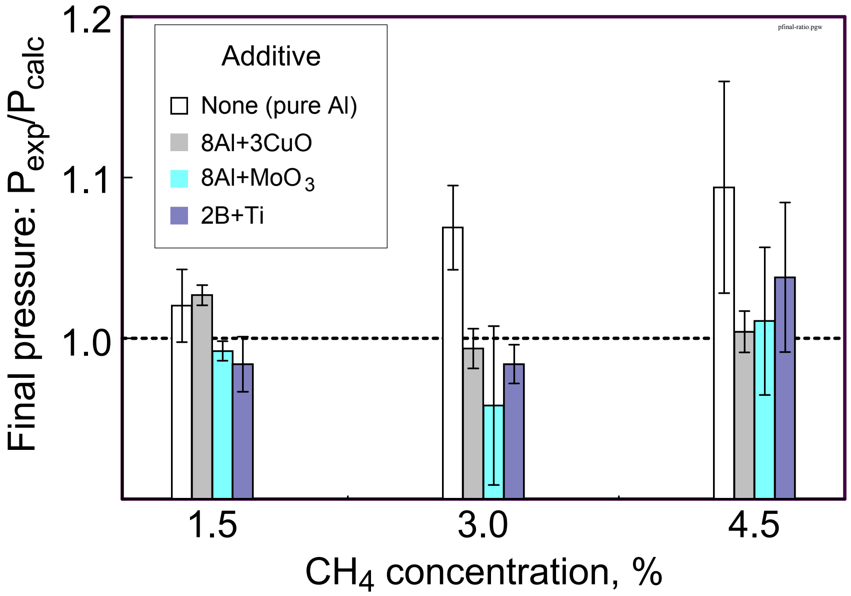

Figure 2.11 Ratios of the measured over calculated final pressures in the explosion vessel for the combustion products cooled to room temperature for varied initial oxidizing environments.

Generally, the higher are the ratios shown in Figure 2.11, the less efficient is the combustion in terms of consumption of gaseous oxidizer. For pure Al, the ratios are always greater than 1 suggesting that, as expected, combustion was less efficient than predicted by equilibrium calculation. It is interesting that for pure Al the pressure ratio shown in Figure 2.11 increases with increased CH_4 concentration. No such trend is observed for aluminum powders burning with nanocomposite additives. It is also interesting that the pressure ratios are in many cases less than 1 (the level of pressure ratio equal to 1 is highlighted by a dashed line). Combustion cannot, of course, be more efficient than predicted by the equilibrium calculations, but it is very possible that the calculations did not take into account complex oxides than can form in presence of multiple fuels. Production of additional condensed fully or partially oxidized compounds can substantially increase the consumption of the gaseous oxygen and thus improve the burning efficiency. In addition, formation of oxy-nitrides and oxy-carbides is possible in the combustion systems considered here. Such complex compounds are difficult to identify from bulk sample XRD analysis described below and a more detailed study of the combustion products would be desired in the future in order to interpret the observed trend in more detail. The trends observed in Figure 2.11 can also be qualitatively correlated to the ratio of the experimental to calculated maximum pressures. The highest maximum pressure attained in the flame corresponds to the lowest final pressure measured after the combustion products are cooled. A simplistic reasoning is that attaining higher pressure means more consumption of gaseous oxidizer in turn resulting in a lower final pressure. This correlation works reasonably well for pure Al and thermite type additives, while the trend is less clear for the 2B+Ti nanocomposite additive. This is likely because the latter additive affects the overall product composition most substantially, chiefly due to a relatively low boiling point of boron oxide.

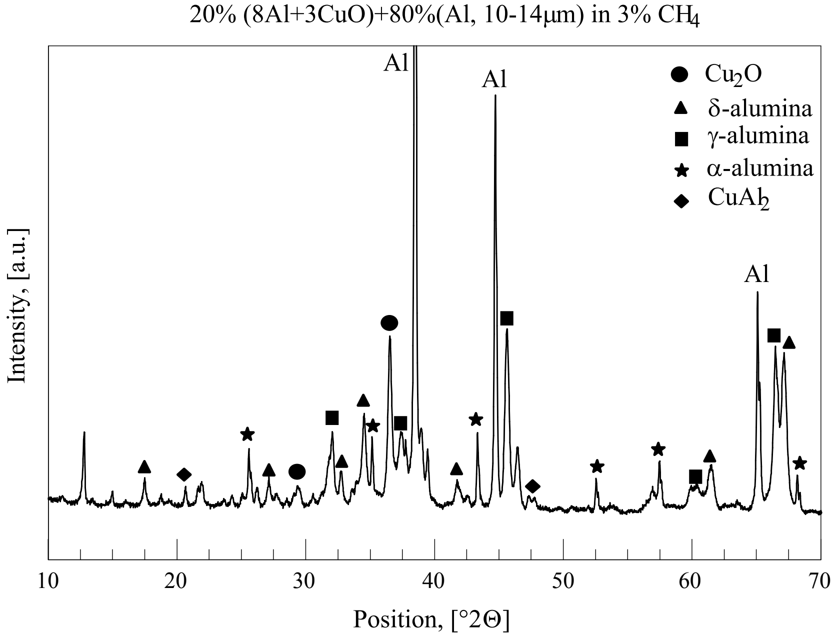

Figure 2.12 Example of XRD pattern of combustion products for case of 20% (8Al+3CuO) modifier in 3% CH_4 environment.

The combustion products from the explosion vessel were collected and analyzed by XRD. Figure 2.12 is an XRD pattern that is typical of the combustion products. It can be clearly seen that pure aluminum peaks are strong, confirming the incomplete combustion. As explained above, part of the material was likely quenched by the vessel walls. Quantitative processing of the measured XRD patterns was difficult because of the lacking crystallographic data for some of the detected transition aluminas (e.g., δ-Al_2O_3) and also because of several peaks that could not be conclusively assigned. Table 2.1 lists the products identified by XRD and the ones predicted from the CEA calculations. Presence of the unreacted Al in the combustion products is the most significant difference between predicted and observed products. Qualitatively, significant additional discrepancies between product species predicted by the CEA calculations and observed by XRD are detected for the fuel system using the nanocomposite 8Al+3CuO additive. In addition to the partially oxidized copper, Cu_2O is not predicted by CEA, and substantial presence of unoxidized Cu-Al alloy, $CuAl_2$, was detected by XRD. It is likely that formation of this alloy resistive to oxidation resulted in a relatively low combustion pressures observed in respective experiments. Note that although some of the predicted products were not identified by XRD, they could still be present in the combustion products and not detected because of a relatively low sensitivity of the bulk XRD analysis.

2.6 Conclusions

Addition of relatively small amounts of nanocomposite burn rate modifiers to aluminum enables substantial increase in its burn rate in gaseous oxidizers without a significant reduction in the overall theoretical combustion enthalpy. The improvements in the burn rates are observed experimentally in the oxygenated environments including products of hydrocarbon combustion. Most importantly, additives of nanocomposite powders of 8Al+MoO_3 and 2B+Ti to micron-sized aluminum were found to be effective in increasing both the rate of pressure rise and maximum pressure in the respective constant volume explosion experiments. It was observed that 20 wt % of additive resulted in the best combination of the achieved burn rate and pressure. Additives of nanocomposite 8Al+3CuO powder did not show appreciable improvements in aluminum combustion, most likely due to formation of an oxidation resistant $CuAl_2$ alloy.

CHAPTER 3

CONSOLIDATION AND MECHANICAL PROPERTIES OF REACTIVE NANOCOMPOSITE POWDERS

3.1 Introduction

There is a rapidly developing interest in exothermically reacting materials that can be used in structural components. Potential applications of these reactive structures and components include munitions casings, fillers for reactive projectiles, liners and waveshapers for shaped charges, reactive fragments, etc. Until recently, the majority of efforts on development and characterization of reactive materials focused on impact-initiated metal-polytetrafluoroethylene (PTFE) composites [20-27]. In such materials, metal powder filler is contained in a soft and ductile polymer binder. The most common metal filler is aluminum. The strength and stiffness of Al-PTFE mixtures with different aluminum particle sizes and morphologies were measured and modeled theoretically in ref. [20]. Performance of the Al-PTFE composites prepared with different size aluminum particles was investigated using a gas gun to initiate the material by high velocity impact [21]. The tensile strength as a function of sintering time and thermal program was explored in ref. [22]. In refs. [23] and [24], related materials with an increased density were studied. The density increase was achieved by adding tungsten powder and the consolidated Al-W-PTFE mixture was subjected to dynamic compression tests to understand its composite behavior under high strain and high strain rate conditions. Related work was reported in ref. [25], where the dynamic compression results showed a correlation between the size of tungsten particles and strength of the composite material. Numerical deformation models were used to predict the effect of particle size on the strength of the composite [25]. Al-PTFE properties were measured as a function of strain rate using split Hopkinson pressure bar and a universal strength tester in ref. [26]. The effect of aluminum content was also investigated. Reference [27] further explained how metal particle size affected the dynamic mechanical properties of the Al-PTFE-W composite by forming force chains. The density and strength of metal-PTFE composites are generally relatively low and thus their practical applications are limited.

General interest in reactive structures was further stimulated by development of various nanocomposite reactive materials including intermetallic and thermite systems, and recent reports describe related consolidated samples and components prepared by sol-gel synthesis followed by spark plasma sintering [28], using epoxy as a binder [29], using multilayer reactive nanofoils prepared by magnetron sputtering [30], and other techniques, e.g,, filled laminate structures [31]. In many cases, consolidated structures are produced with little or no binder. Preparation and characterization of one type of such reactive materials are discussed. This study explores the use of reactive nanocomposite powders prepared by arrested reactive milling (ARM) [7] and consolidated using uniaxial die compaction into cylindrical pellets.

3.2 Materials and Methods

3.2.1 Material Preparation

The samples were consolidated from a set of reactive nanocomposite powders synthesized by ARM. The nanocomposite powders were Al-rich thermite compositions: $12Al\cdot MoO_3$, $8Al\cdot MoO_3$, and $8Al\cdot 3CuO$. These thermite systems were chosen due to their reactivity and high aluminum metal content. Details of synthesis and properties are found in the literature [14, 32]. All powders had particle sizes in the range of 1 – 100 µm. Reference samples were consolidated from spherical aluminum powder by Alfa Aesar (3 – 4.5 µm nominal size, 97.5% pure). Finally, additional reference samples were consolidated using unmilled powder blends of Al and commercial CuO and MoO_3 mixed in the same proportions as in the nanocomposite materials. The powder blends contained the same materials that were used to prepare reactive nanocomposites, including Al powders by Atlantic Equipment Engineers, -325 mesh (<45µm), 99.5% pure, CuO powders by Sigma Aldrich (25µm), 99+% pure, and MoO_3 by Alfa Aesar, 99.95% pure. The MoO_3 powder contained flake-like particles; SEM images showed thickness of 1-3 µm. The lengths and widths of the flakes varied broadly reaching up to ~ 100 µm. Materials added in small amounts as binders for selected consolidated samples included polyethylene glycol (PEG) and indium powder from Advanced Machine and Materials -325 mesh, 99.99% pure.

3.2.2 Calculated Enthalpies of Reaction

Figure 3.1 shows the calculated enthalpies of reaction and theoretical maximum densities (TMD) of the $Al{\cdot}MoO_3$ and $Al{\cdot}CuO$ thermite compositions as a function of their composition. In addition to the specific heat released assuming the aerobic reaction (e.g., $Al+MO_x+O_2 \rightarrow Al_2O_3+MO_x$), shown are the ratios of the enthalpy of the anaerobic (i.e., thermite) reactions to the enthalpies of the respective aerobic reactions. The reaction enthalpies increase with increasing aluminum content, while the bulk densities decrease, in both cases approaching characteristics of the pure aluminum.

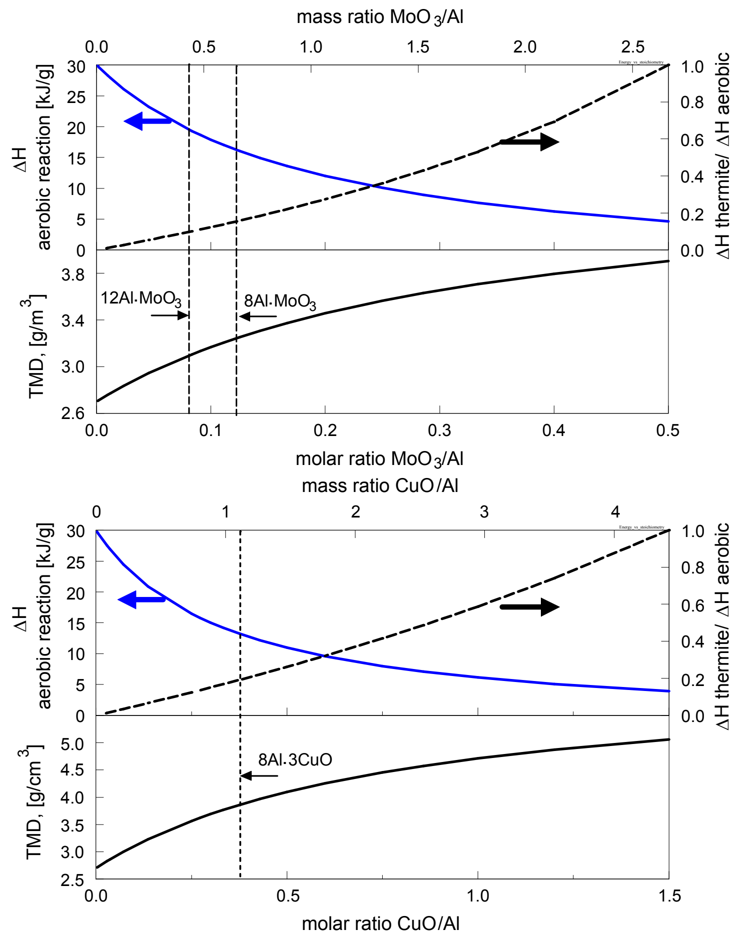

Figure 3.1 Reaction enthalpy and material density as a function of stoichiometry for Al·MoO_3 and Al·CuO thermites.

Vertical dashed lines indicate the compositions prepared in this study. The enthalpies of aerobic reaction are in the 15 – 20 kJ/g range for the MoO_3 nanocomposites, and in the 10-15 kJ/g range for the CuO nanocomposite. These enthalpies are greater than, but still of the order of magnitude of full oxidation of monomolecular energetic materials such as RDX and HMX (8.8 kJ/g) [33].

3.2.3 Consolidation Details

Pellets of pressed powders were prepared using a Carver auto-series 25 ton press and two sets of pressing dies. Round cylindrical pellets with diameters of 0.5” and thickness of approximately 0.125” were prepared using a 0.5 inch diameter steel-sleeved tungsten carbide die. These pellets were used for tensile strength testing. In addition, several round cylindrical pellets were prepared using the same 0.5 inch diameter die but pressed using the Instron 5567 universal testing machine to apply controlled pressure at compression rates lower than achievable using the Carver press. The deformation and applied forces were recorded while preparing these latter pellets to characterize the entire consolidation process and properties of the powders being consolidated. Rectangular pellets with dimensions of 1.25”× 0.50”× 0.25” were prepared for flexural strength testing. The samples for the flexural strength test were made with a steel-sleeved tungsten carbide die machined according to the ASTM standard specifications [34]. The ASTM standard also provides the methodology for compaction for these rectangular pellets. The powders were compacted in two steps. The first step involved pressing with the die elevated with spacers and the lower punch not fully inserted. In the second step, the spacers were removed and the lower punch was fully inserted. This helped increasing the compaction of the pellet by overcoming some of the wall friction effects. As a result, the densities of the pellets prepared using this two-step procedure were higher than for the rest of the pellets consolidated in one step.

For all consolidation experiments, the walls of the dies were lubricated with Teflon spray. When using the Carver automatic press, the compression rate was kept constant using the built-in medium setting. The dwell time was set at 60 seconds.

Compaction pressures used were in the range of 105 – 500 MPa. A slower compression rate of 0.5 mm/min was achieved for the samples consolidated using the Instron universal testing machine.

When additional binders were used, compaction conditions were adjusted. Specifically, when indium powder was added for additional bonding in the consolidated samples, the samples were pressed by the Instron 5567 inside a controlled environment and temperature chamber. The chamber temperature was preset to 200ºC to melt indium. The PEG polymer was incorporated by first dissolving it in a solution of 100% ethanol. The powder was then added to the solution and mixed well. The mixing continued until all the ethanol evaporated and left a PEG coating on all particles.

3.2.4 Mechanical Testing

Two mechanical tests were used in this project to determine flexural strength and tensile strength of the prepared samples.

The standard testing method for green strength of compacted metal powders is given by ASTM B312-96 (2002). The test specified is the three-point bend also known as the flexural strength test. The configuration used for the test is shown in Figure 3.2. A rectangular specimen of uniform cross-section is supported at each end with the distance *l* between the support points. A load, *P*, is applied at the center of the beam. The test specimen preparation and test itself are performed according to the ASTM standard for testing the green strength of metal powder compacts.

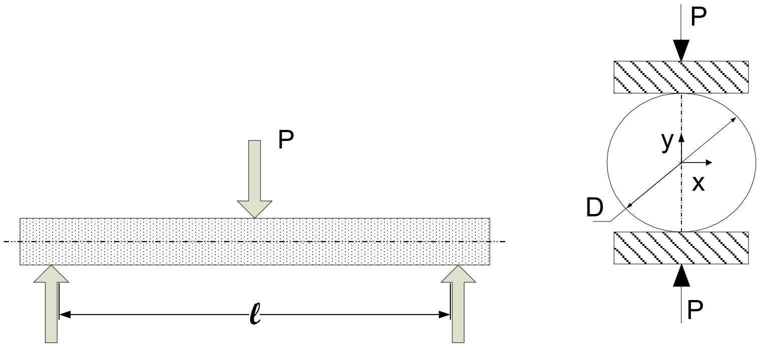

Figure 3.2 Setup of three-point flexural strength test (left) and DC test (right).

Conventional tensile strength tests are difficult to apply for samples prepared as consolidated powders, especially due to unwanted stresses contributed by the gripping devices. An alternative test widely used to quantify the tensile strength of brittle materials (typically prepared by powder consolidation) is the diametrical compression (DC) test also known as the Brazilian test [35]. In this test, also illustrated in Figure 3.2, a thin disc is transversely compressed (applied load P) resulting in a uniform horizontal tensile force along the vertical (y) axis. This technique provides a way of measuring the tensile strength of brittle materials; it was initially developed to test the tensile strength of concrete and rocks. It is widely used in testing ceramics, rocks, metal composites, dentistry materials, and pharmaceutical compacts [35-37]. An analytical solution for the stress distribution of this system was obtained in 1895 by Hertz and can be found in [37].

The instrument used for the strength measurements was an Instron 5567 universal strength tester. The grips used include standard compression platens and grips for three-point bend test. The cross-head extension rate used for the DC test was 0.2 mm/min. When performing the flexural strength test, a load rate of 89 N/min was used as per the ASTM standard.

3.2.5 Characterization of the Prepared Pellets

The pellets were inspected using scanning electron microscopy (SEM). A LEO 1530 Field Emission Scanning Electron Microscope with backscattered electron (BSE) detector was used. To characterize any changes in reactivity of the nanocomposites due to consolidation, differential scanning calorimetry (DSC) was performed using a Netzsch Instruments STA 409 PC/4/H Luxx Simultaneous Thermal Analyzer. Finally, phase compositions of the prepared samples were investigated using a Philips X'pert MRD X-ray diffractometer system.

3.3 Results and Discussion

3.3.1 Mechanical Testing

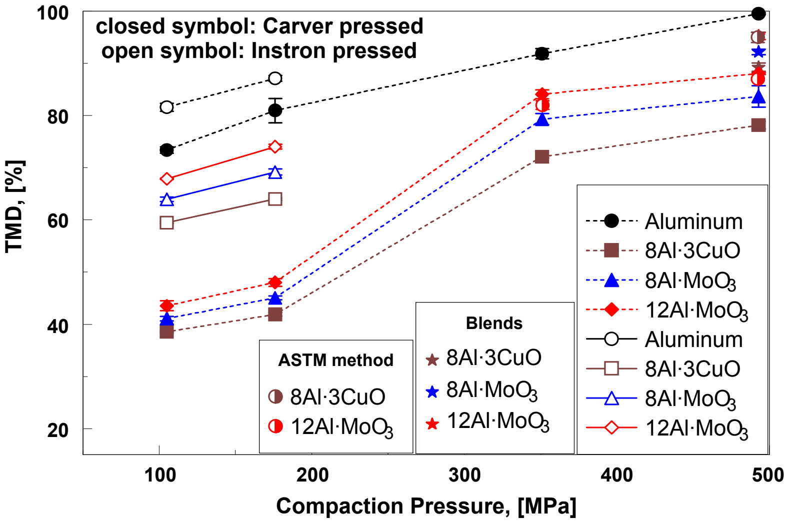

Figure 3.3 Results of density as function of compaction pressure for several materials and two rates of compaction.

Figure 3.3 shows the packing fraction, defined as the measured density over theoretical maximum density, as a function of the compaction pressure. Two main sets of data are shown here and in Figure 3.4 below, where the filled symbols represent compaction using the Carver automatic press, and the open symbols represent samples compacted using the Instron (allowing for a slower consolidation rate). Each data point in Figure 3.3 and 3.4 represents at least three individual measurements. The error bars show standard deviations. In some cases the experimental scatter is so small that the error bars are invisible. In addition, star-shaped symbols represent the measurements for consolidated powders of Al blended with commercial oxides in the same proportions as in the prepared nanocomposite materials. These samples were prepared to observe the effect of mechanical milling on mechanical properties of nanocomposite particles as compared to the particles of the starting materials. The half filled symbols represent the samples consolidated according to the ASTM method. This method results in an improved consolidation for the $8Al{\cdot}3CuO$ sample, while effectively no difference in the achieved density is observed for $12Al{\cdot}MoO_3$.

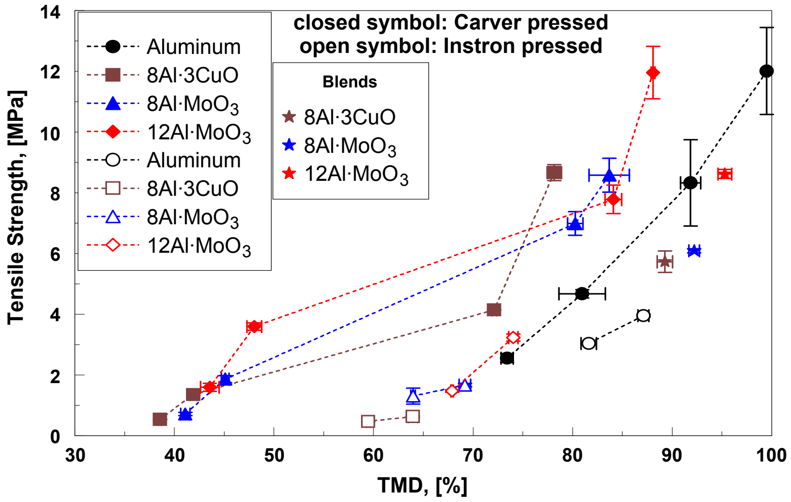

Figure 3.4 Tensile strength as a function of density for several materials and two rates of compaction.

Generally, the packing density increases with the compaction pressure. Higher packing densities are achieved for all materials at the same respective pressures when the samples were consolidated at a slower speed. It is also noted that materials with higher overall aluminum concentrations are consolidated to higher densities. There is a noticeable increase in the density for the nanocomposites when the compaction pressure increases from 200 MPa to 350 MPa, which could indicate the transition between the simple particle packing at lower pressures and induced particle deformations achieved at higher pressures. For pure aluminum, the increase in packing density as a function of pressure appears to be following a nearly linear trend.

Figure 3.4 shows the results obtained from the DC test for the tensile strength of the compacts as a function of their density. For all materials, the strength increases with an increased density. The pellets prepared from nano-composite powders exhibit higher strength than the pure aluminum pellets at the same density. Among all nanocomposite samples, the highest strength was measured for the sample with bulk composition $12Al\cdot MoO_3$. Its strength is equivalent to that of the pure aluminum sample consolidated to a higher density. Interestingly, the compacts made using the Instron, although higher in density, exhibit decreased strength.

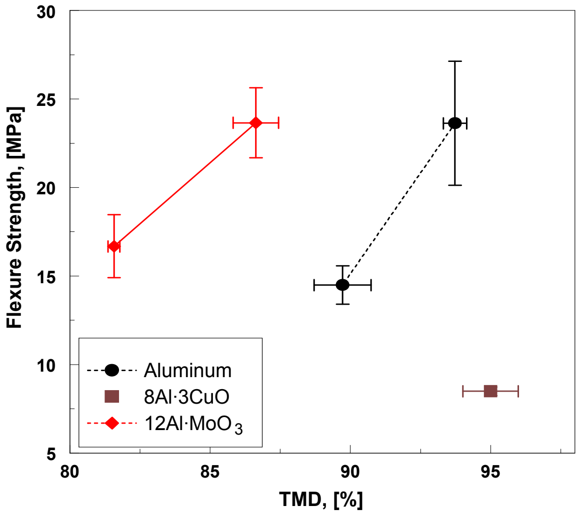

Figure 3.5 Results of three point flexural strength test.

Figure 3.5 shows results of the flexural strength testing for the rectangular pellets of pure aluminum and the 12Al·MoO$_3$ and 8Al·3CuO nanocomposite consolidated following ASTM B312-96 (2002) and using the automatic Carver press. The results are presented as a function of the sample density. As expected, the measured flexural strengths are much higher than those measured by the DC test. Similarly to the results for tensile strength shown in Figure 3.4, the consolidated nanocomposite sample achieves the same flexural strength as aluminum but at a lower density.

High strength is an important property for a structural material and one approach used to increase the strength of shapes prepared by powder consolidation involves addition of binders. As noted above, PEG and indium were used as binders for selected samples. Figure 3.6 shows the comparison of tensile strength measurements for the samples prepared with and without binders. The samples containing indium were pressed at both room temperature and 200°C. Otherwise, all samples were consolidated using the same conditions. The hot pressed samples with indium binder showed the best improvement overall, including both the highest achieved density and tensile strength.

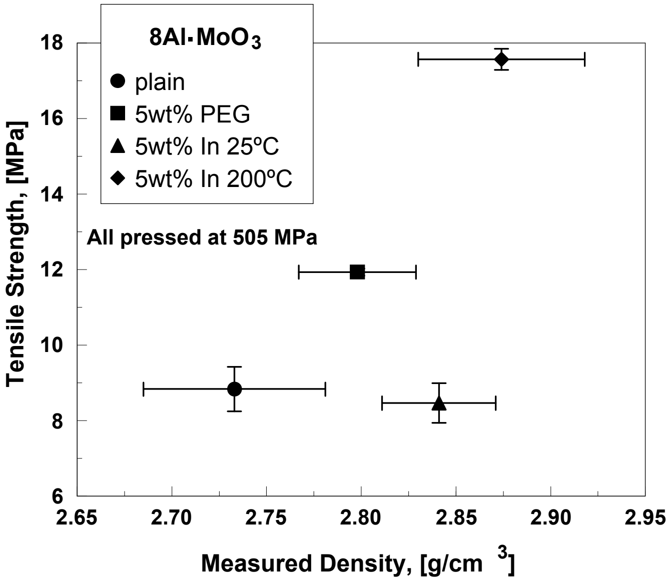

Figure 3.6 Effect of binder addition and processing on strength and compactability of powder.

Compaction curves measured using the Instron machine, were processed for a set of samples to obtain the yield strength of the powders processed by ARM. The yield strength is important for modeling the interaction of powder particles and shock waves, e.g., upon initiation of an explosion or upon collision of a particle with an obstacle (as in the case of reactive fragments or impact initiated energetic components). The yield strength of each material was determined using the Heckel equation [38]; the results are shown in Figure 3.7.

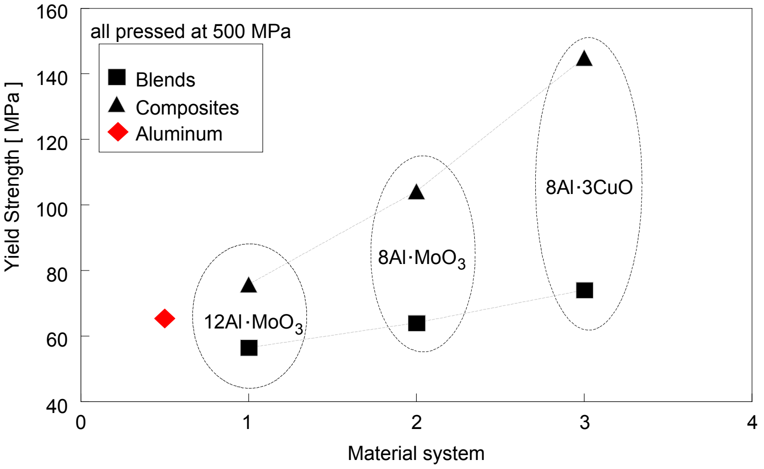

Figure 3.7 Material yield strength for mechanically milled nanocomposite and unmilled (blended) powders with identical bulk compositions.

While similar data have been reported for multiple composite powders [39-40], this is the first assessment of basic mechanical properties of reactive nanocomposite powders prepared by ARM. Also shown is the yield strength implied by the compaction curves for a pure unmilled aluminum powder. This value coincides with that reported in the literature for pure aluminum [41]. For reference, equivalent yield strengths are also shown for the metal-oxidizer blends, which were not ball milled. The powders of milled materials exhibit consistently higher yield strengths than either pure Al or Al blended but not milled with oxide. The higher yield strength for reactive nanocomposites prepared by ARM can be attributed to both, the work hardening effect of milling and the dispersion of metal oxide inclusions within the aluminum matrix. Although it is understood that using the Heckel parameter may result in a systematic error in the identified yield strength of materials, the values and, more importantly, trends reported here are useful as a starting point. More accurate methods are described in [42] which explore micromanipulation techniques for analyzing single particles.

3.3.2 Pellet Characterization

Pellets were embedded into epoxy, cross-sectioned, and inspected using an SEM with a BSE detector. Figure 3.8 shows two SEM images of the 8Al·3CuO material consolidated at different pressures to achieve different percentages of TMD.

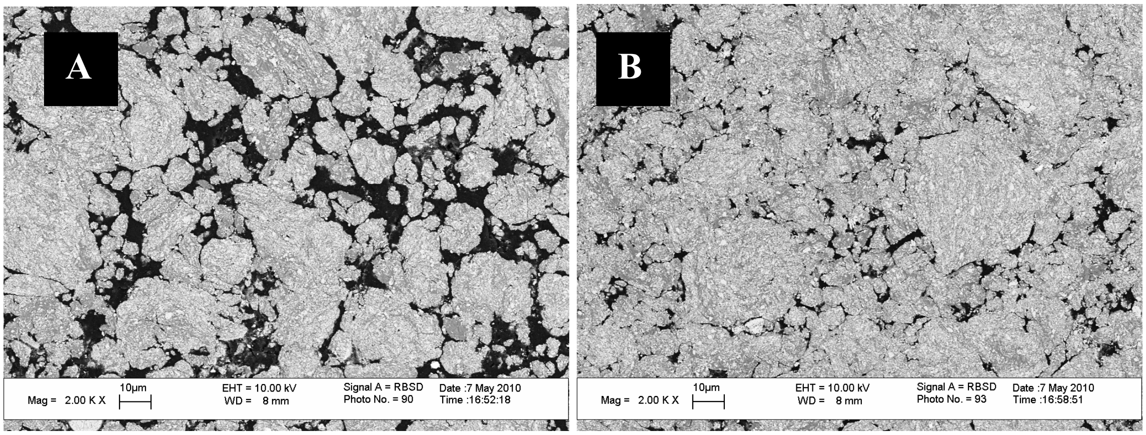

Figure 3.8 SEM images of cross-sectioned 8Al·3CuO pellets at a) 41.5% of TMD and b) 78.9% of TMD.

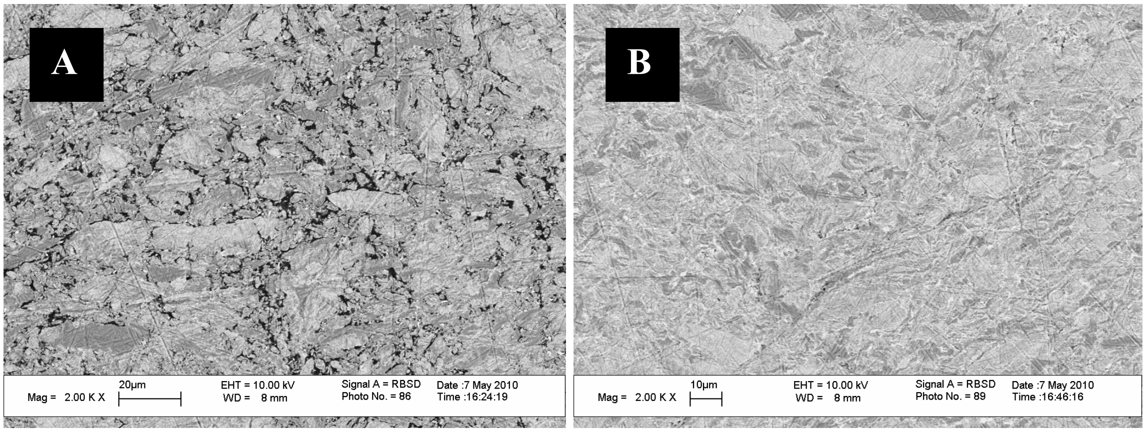

Figure 3.9 SEM images of cross-sectioned 8Al·MoO3 pellets at a) 41.2% of TMD and b) 85.1% of TMD.

Within the particles, the light colored areas represent the metal oxide inclusions. The darker gray areas represent the aluminum matrix. Substantial porosity (black areas, filled with epoxy in the cross-sectioned specimen) and multiple particles barely touching one another are visible in Figure 3.8a, showing a cross-sectioned pellet with a relatively low density (41.5 % TMD). Also, it can be seen that the particles are generally equiaxial, so that there is no noticeable particle deformation as a result of consolidation. In comparison, Figure 3.8b shows that the cross-sectioned pellet of a higher density (78.9 % TMD) contains fewer voids. Particles are in intimate contact with one another, which is consistent with the higher mechanical strength measured for denser pellets. While some particles are apparently bonded to each other, it is difficult to clearly detect deformation of individual particles.

Figure 3.9 shows cross-sections for consolidated nanocomposite pellets of $8Al{\cdot}MoO_3$ prepared by ARM with different densities. Like in the case of $8Al{\cdot}3CuO$, the low density pellet, Figure 3.9a, shows significant porosity. In Figure 3.9b the particles are more closely packed similar to the case in Figure 3.8b.

In order to assess any changes in the material reactivity due to consolidation the pellets were analyzed using DSC. The samples were not cross-sectioned or polished for the DSC analyses, so that the possible effects of such sample processing were removed. Figure 3.10 shows the baseline-corrected DSC traces obtained for samples heated in an argon flow at 5 K/min. The traces are shown for an unconsolidated $8Al{\cdot}MoO_3$ nanocomposite powder and for the respective sample consolidated to 85.1 % TMD (the same as shown in Figure 3.9b.) The DSC trace for the powder is similar to that reported previously in [14].

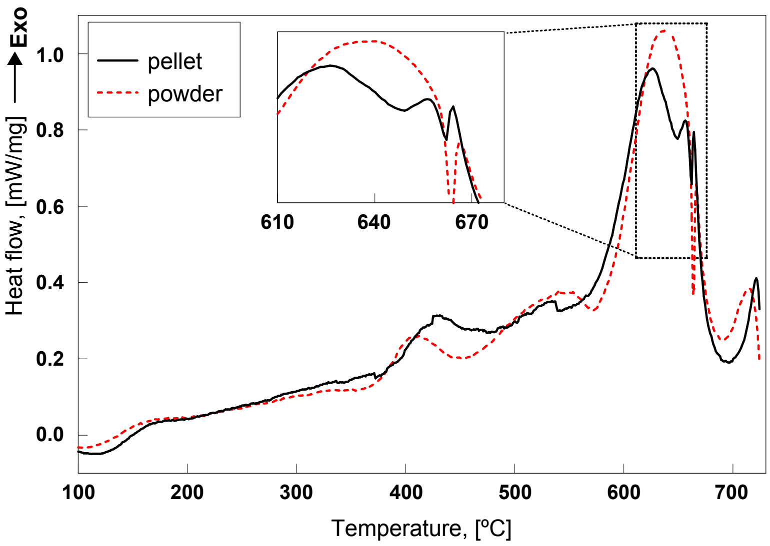

Figure 3.10 DSC traces for $8Al \cdot MoO_3$ pellet (85.1% of TMD) and $8Al \cdot MoO_3$ powder heated at 5 K/min in argon flow.

The DSC trace for the pellet is very similar to that of the unconsolidated powder. It exhibits the same exothermic peaks as the powder, with the main differences detected in the temperature region magnified in the inset shown in Figure 3.10. In particular, the differences between the traces are noticeable in the vicinity of 630 – 670 ºC for both the strongest exothermic peak and for the following Al melting endotherm. The magnitude of the strongest exothermic peak for the pellet is slightly smaller than that for the powder; while the magnitude of the endothermic Al melting peak for the pellet is substantially smaller than that for the powder. Both differences point to a reaction that could have occurred during consolidation or shortly thereafter, at low temperatures, and consumed some of the metallic aluminum prior to the strongest thermally activated thermite reaction.

Integration of the DSC curves yields a reaction enthalpy of about 1.92 kJ/g for both cases. For this approximate assessment, the entire area under the curve was integrated using the Netzsch Proteus software. A straight horizontal baseline was used. Clearly, selection of a different and, probably, more accurate baseline would result in a different value of the integral; regardless, the baselines are likely similar for both measurements. Therefore, for this analysis aimed only to compare the DSC signals for the pellet and powder, selection of a flat baseline was acceptable. The difference between the integrated values was less than 1% for the consolidated pellet and the powder. This integrated reaction enthalpy value represents about 75% of the total reaction enthalpy for the thermite reaction for the 8Al·MoO_3 nanocomposite, so that any possible effect of partial reaction occurring during consolidation is not quantifiable from the integrated DSC traces.

Further, the effect of possible partial reactions caused by the sample consolidation on its phase composition was studied using x-ray diffraction (XRD). Figure 3.11 shows the XRD patterns for nanocomposite powder and for the respective consolidated pellets (41.2 and 81.5 % TMD).

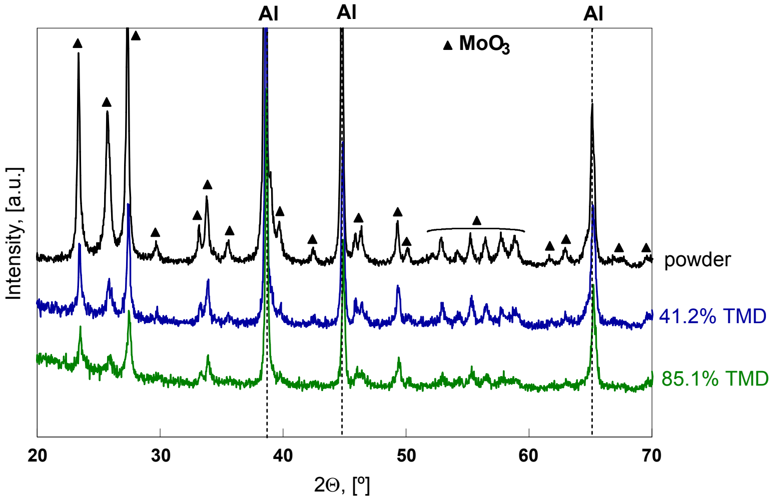

Figure 3.11 XRD patterns for 8Al·MoO_3 powder and pellets.

The powder sample shows presence of Al and MoO_3 which are the initial starting materials. No other phase is detected. The two pellet samples also show the same starting phases and no additional phases formed during consolidation. Note that poorly crystalline phases or phases present as nano-inclusions may be undetectable by XRD patterns. One noticeable change between the XRD patterns for powder and consolidated samples is the reduced ratio of the integrated intensity of the MoO_3 peaks over the integrated intensity of Al peaks. The MoO_3 peak intensities decrease in comparison to the Al peaks as the pellet is compacted to higher densities. This may indicate partial reduction of MoO_3 resulting in smaller MoO_3 inclusions and/or smaller overall MoO_3 concentration.

Additionally, consistent with the DSC analyses, no substantial presence of any reaction products in the consolidated samples was detected. Note finally, that as briefly described elsewhere [43], all consolidated samples were successfully ignited using a CO_2 laser beam. Upon ignition, all samples described in this paper completely disintegrated with multiple fragments ejected and burning in the surrounding gas, demonstrating high reactivity of the prepared materials. Details of the laser ignition experiments and their interpretation will be reported separately.

3.4 Conclusions

Reactive nanocomposite powders prepared by ARM with bulk compositions $8Al{\cdot}3CuO$, $8Al{\cdot}MoO_3$ and $12Al{\cdot}MoO_3$ were successfully consolidated into reactive pellets with diameters varied from 0.25” to 0.5”. Rectangular pellets with dimensions of 1.25”× 0.50”× 0.250” were also prepared. Densities close to or exceeding 90% TMD were achieved while maintaining high reactivity of the consolidated samples. The mechanical properties of the consolidated samples are similar to those of consolidated inert powders. An increase in the tensile strength was achieved with addition of small amounts of binders. For $8Al{\cdot}MoO_3$, the highest density (~ 2.9 g/cm^3) and strongest (~ 17.5 MPa tensile strength) samples were obtained when indium was added as a binder and consolidation was performed at the temperature exceeding the melting point of indium.

Yield strength of the reactive nanocomposite powders was determined from compaction load vs. displacement curves using the Heckel equation and was found to be greater by about 20 – 100% for the ARM prepared powders as compared to the starting materials and pure aluminum. Comparisons between the phases present in the unconsolidated powders and respective pellets and between reactions occurring in the powders and pellets upon heating showed differences that were smaller than could be quantified from the DSC and XRD analysis. This indicates that consolidation did not cause significant reduction in the material reactivity.

CHAPTER 4

THERMAL INITIATION OF CONSOLIDATED NANOCOMPOSITE THERMITES

4.1 Introduction

Reactive materials with compositions capable of highly exothermic combustion but not capable of detonating are being developed for multiple applications, including energetic formulation modifiers and fuel additives. Another interesting application of these materials is in reactive structural components. Such components replacing inert casings, liners, fillers, penetrators, and other parts made currently of chemically inert solid materials can be used to substantially improve performance of various munitions, including shaped charges, projectiles, and reactive fragments. For such dual type applications, reactive materials need to have adequate mechanical properties as well as the proper reactivity. This study explores reactive nanocomposite powders prepared by arrested reactive milling (ARM) [8] and consolidated using uniaxial die compaction into cylindrical pellets. Pressing of these powders into pellets and mechanical properties of the obtained compacts were described previously in Chapter 3. This chapter focuses on thermal initiation of the prepared pellets.

In many practical applications, reactive materials are initiated by shock or impact. Impact initiation was studied for Al/Polytetrafluoroethylene (PTFE) reactive spheres in ref. [44]. However, the results of such tests are difficult to interpret in terms of ignition mechanisms because of multiple phenomena involved, including breaking up the initial sample and further initiation of produced fragments. Thermal initiation is better suited for mechanistic interpretations and it was used to ignite Ni-Al consolidated samples, which were resistively heated by an electric current [45]. Preliminary experiments with a similar, resistive heating approach applied to consolidated nano-thermites explored here showed that ignition was poorly reproducible. The difficulty was most likely due to a lower electric conductivity of thermites as compared to all metal Ni-Al composites. Therefore, when voltage was applied, a uniform sample heating was not achieved. Instead, narrow electrically conductive channels formed inside the pellets resulting in their local ignition and loss of the sample integrity. The dimensions of the initially ignited portions of the sample were poorly reproducible depending on the shape of the initially formed conductive channels. In another thermal initiation study, samples were ignited after being placed inside a furnace [46]. While simple experimentally, that approach can only explore relatively low heating rates, which may be irrelevant for initiation in practical configurations.

A laser beam provides a conveniently controlled and intensive energy source and it was exploited to ignite consolidated samples of metastable interstitial composites (MIC), prepared by mixing starting metal and oxide nanopowders [47]. The experimental technique developed in this study also involves thermal initiation of consolidated samples by a CO_2 laser. A numerical model is developed to complement the experimental study and describe the heat transfer and an exothermic chemical reaction occurring in the sample and leading to its ignition.

4.2 Materials

Cylindrical pellets were consolidated from a reactive nanocomposite powder synthesized by ARM. The nanocomposite powder was an Al-rich thermite composition $8Al{\cdot}MoO_3$. This thermite system was chosen due to its high reactivity and a relatively high aluminum metal content, attractive for applications where aerobic reaction is expected to follow up the thermite initiation. Al powder by Atlantic Equipment Engineers, -325 mesh (<45μm), 99.5% pure and MoO_3 powder by Alfa Aesar, 99.95% pure, were used as starting materials for ARM. Details of synthesis and properties of the prepared nanocomposite powders are found in the literature [14].

Theoretical maximum density (TMD) and maximum reaction enthalpies for both aerobic, ($8Al+MoO_3+6O_2 \rightarrow 4Al_2O_3+MoO_3$), and anaerobic reactions, ($8Al+MoO_3 \rightarrow Al_2O_3+Mo+6Al$), for the consolidated $8Al{\cdot}MoO_3$ and for a reference Al/PTFE reactive material, are presented in Table 4.1. (Note that for Al/PTFE, two slightly different reaction enthalpies from two sources [48, 49] are shown in Table 1.) The anaerobic reaction enthalpy for the metal-rich $8Al{\cdot}MoO_3$ is less than the stoichiometric Al/PTFE, however, the aerobic reaction enthalpy for the metal-rich thermite is very high warranting interest in such compositions. In these metal-rich materials, the thermite reaction is expected to provide a powerful initiating mechanism followed by the complete aerobic reaction.

Table 4.1 Theoretical Maximum Density and Maximum Reaction Enthalpies for Both Aerobic and Anaerobic Reactions for Consolidated Material

Material	TMD, g/cm^3	Heat of reaction, kJ/g	
		Anaerobic	Aerobic
$8Al{\cdot}MoO_3$	3.25	2.55	18.02
Al/PTFE	2.31	8.66 [48], 9.10 [49]	-

In addition to the reactive materials pellets, inert pellets comprising blends of Al and Al_2O_3 powders were prepared and used for calibration of the heat transfer model, as described below.

4.3 Experimental

4.3.1 Consolidation Details

Pellets of pressed powders were prepared using a Carver Auto-Series 25 ton press and a 0.635 cm diameter steel die. Round cylindrical pellets with diameters of 0.635 cm and thicknesses of 0.177 - .254 cm were prepared. The mass of powder used per pellet was 200 mg. Compaction pressures varied in the range of 0.14 – 1.96 GPa. For consolidation, the inner wall of the die was lubricated with DuPont Teflon® dry film spray for each pressing. Further consolidation details are available elsewhere [50].

4.3.2 Pellet Characterization

Thermal diffusivity of the prepared pellets was required for modeling conductive heat transfer and ignition; it was measured using the flash method [51]. A pellet surface was heated by a short laser pulse and the temperature increase at the back of the pellet was measured. The time the temperature reached one half of its peak value was used to quantify the thermal diffusivity. The measurement was performed using the same setup as used for ignition (see below). In particular, very low energy of 11±1 W and a short laser pulse of 50 ms were used. Instead of a single thermocouple, a thermopile was mounted on the rear surface of the pellet to amplify the relatively weak signal produced by a small temperature increase. The thermopile was made of four type E thermocouples connected in series. The junctions were positioned on the rear surface of the pellet at its center and a small amount of thermal paste was applied to improve the heat transfer between the surface and junctions. The thermal paste used was Arctic Silver by Ceramique, which is electrically insulating and highly thermally conductive.

Pellet densities were determined based on their mass and physical dimensions. The mass of the pellet was measured using a digital analytical scale with the accuracy of 0.1 mg. The diameter and thickness of the pellet were measured using a caliper with the accuracy of 0.0025 cm. The TMD was calculated assuming a fully dense composite of $8Al{\cdot}MoO_3$. Finally, the packing fraction was determined as the ratio of the experimental density and the calculated TMD.

4.3.3 Ignition

The consolidated samples were ignited using a defocused CO_2 laser beam. The experimental setup is shown in Figure 4.1.

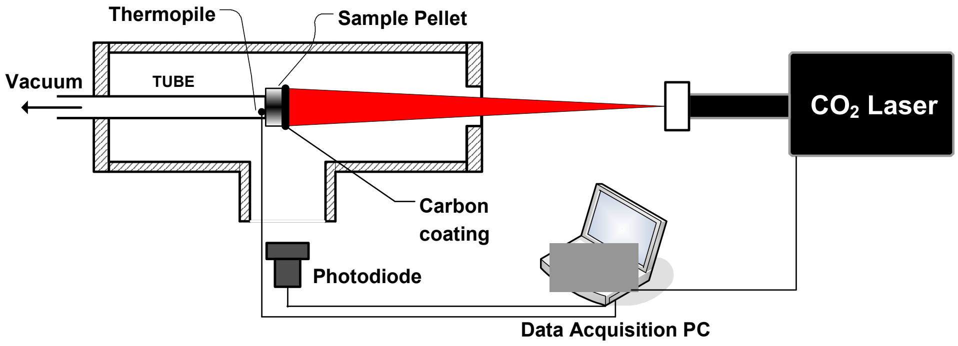

Figure 4.1 Experimental setup for ignition of pellets. A thermopile at the back of the pellet was used for the thermal diffusivity measurements by flash method. For ignition tests, the thermopile was removed and in selected experiments replaced with an individual E-type thermocouple.

In the experiment, the pellet is held by vacuum suction on the end of a thin tube. Ignited pellets disintegrate explosively, so the holder tube and the pellet itself are located inside a chamber containing fragments and combustion products produced during the pellet initiation. The pellet is heated from one side by the Evolution 125 Synrad CO_2 laser beam (10.6 μm wavelength). A ZnSe lens (not shown in Figure 4.1) was used to adjust the diameter of the beam heating the pellet to be equal to the pellet diameter. This way the heat flux is applied nearly uniformly to the entire pellet surface. Although the laser beam profile is often described using a Gaussian distribution, the laser beam profile was found to be nearly uniform when analyzing the imprint on a fluorescing board. Also, implementing a Gaussian distribution into the numerical model gives unrealistic results when finding ignition delay due to highly concentrated heating of the center of the pellet even when adjusting absorption coefficient. In addition, the pellets were coated with a thin layer of carbon powder to achieve a uniformly enhanced absorption of the laser power independently of the surface properties of individual consolidated samples. Preliminary tests showed that without the coating, the pellets reflected a greater fraction of the laser power and were somewhat more difficult to ignite. A photodiode sensor model DET110 by Thorlabs was placed perpendicular to the pellet surface and was used to determine the ignition moment accompanied by a strong light emission. The laser-heated pellet surface ignited first, with the following reaction propagation and disintegration of the entire pellet. In selected tests, a type E thermocouple was mounted to the rear surface of the pellet to record the temperature history of the pellet preceding its ignition. Upon ignition of the last layer, the thermocouple was typically damaged and replaced for each experiment.

Figure 4.2 shows an example of the data signals obtained from the ignition experiment. The laser pulse is triggered after a 250 ms delay from the beginning of signal acquisition. The photodiode signal indicates ignition by a sharp spike. The ignition delay is measured from the beginning of the laser pulse to the front of the photodiode signal.

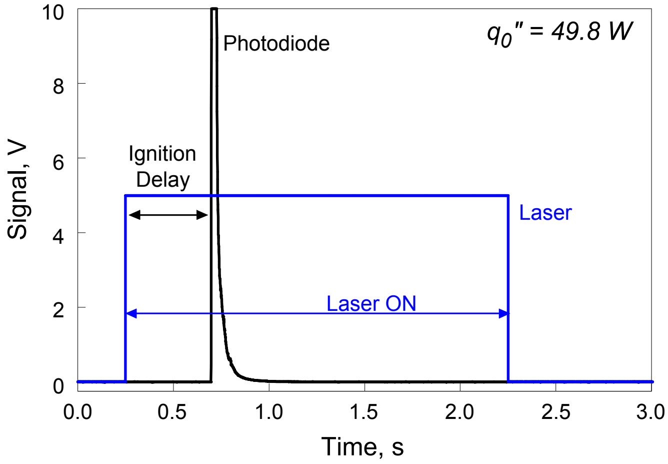

Figure 4.2 Example of data acquired for ignition delay experiment of 8Al·MoO_3 86.74% TMD.

4.3 Heat Transfer Model

A numerical model was created to describe the heat transfer in the cylindrical pellet and describe the pellet ignition as a result of the thermal stimulation. The heat transfer is described in the radial and axial dimensions. Figure 4.3 illustrates the configuration considered in the model.

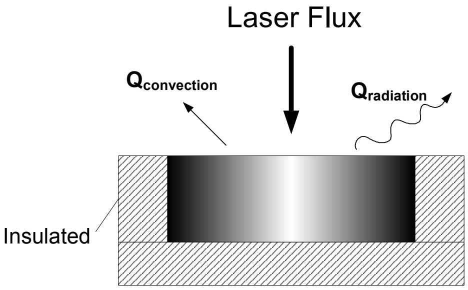

Figure 4.3 Configuration used in the numerical heat transfer model.

The laser beam directly heats up the top surface of the pellet. The same surface loses heat to surroundings by natural convection and radiation. The circumferential as well as the bottom surfaces are assumed to be thermally insulated. Convective heat losses on the circumferential surface were considered in preliminary calculations and were found to be insignificant for the relatively short heating times prior to the pellet ignition. Thus, an insulated boundary condition for the pellet circumference was justified. This configuration effectively resulted in a one dimensional heat transfer analysis performed along the pellet axis.

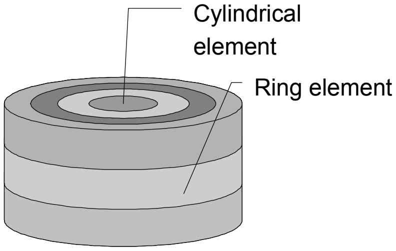

Figure 4.4 Discretization of pellet into volume elements.

The elemental volume geometry is that of rings stacked on top of one another, except for the central elements, which are stacked cylinders as shown in Figure 4.4. There are 20 radial elements and 50 axial elements. The heat transfer solution is obtained using the explicit finite difference method to balance energy for each volume element:

$$mC_V \frac{\partial T}{\partial t} = \dot{Q}_{laser} + \dot{Q}_{cond,z} + \dot{Q}_{cond,r} + \dot{Q}_{rad} + \dot{Q}_{conv} + \dot{Q}_{chem} \qquad (4.1)$$

where T is temperature and t is time, m is the element mass, C_v is its specific heat. The change in C_v as a function of temperature was considered using respective reference data for Al and MoO_3 [52]. The right hand side of Equation (4.1) includes the heat transfer rate terms denoted by respective subscripts; the last heat transfer term in the RHS of Equation (4.1) represents the exothermic chemical reaction leading to ignition. Aluminum melting was accounted for by fixing the elemental volume temperature at the Al melting point until the volume absorbed the energy equal to the latent heat of melting for the Al contained in it. Note, specifically, that ignition was predicted to occur at temperatures lower than the Al melting point, as discussed below.

Based on the selected configuration Figure 4.3 and respective boundary conditions, the only volume elements that experience convective, radiative, and laser flux heat transfer are those in the top surface. The applied laser power is described as:

$$\dot{Q}_{laser} = a \cdot A \cdot q_0'' \tag{4.2}$$

where A, is the top surface area of the element, q_0'' is the laser power and a is the absorption coefficient. The value of the absorption coefficient was obtained from additional experiments with inert composite pellets which were carbon coated in the same way as reactive material pellets, and for which the calculated and measured temperature profiles at the back of the pellets were matched to each other. The axial and radial conductive heat transfer rates are computed respectively as:

$$\dot{Q}_{cond,z} = -k_0 A_z \frac{\partial T}{\partial z} \tag{4.3}$$

$$\dot{Q}_{cond,r} = -k_0 A_r \frac{\partial T}{\partial r} \tag{4.4}$$

The thermal conductivity, k_0, is found based on the measured thermal diffusivity, sample density, and specific heat. The changes in the thermal conductivity as a function of temperature are neglected and the samples are assumed to be isotropic. These assumptions are reasonable if the sample temperature does not change substantially prior to its ignition.

The radiation heat transfer rate is calculated as:

$$\dot{Q}_{rad} = \varepsilon\sigma A(T^4 - T_\infty^4) \tag{4.5}$$

The emissivity of the surface, ε, is assumed to be that of the carbon powder and σ is the Stefan-Boltzmann constant. A simple estimate for the heat transfer due to natural convection from the top surface is made using Newton's law:

$$\dot{Q}_{conv} = hA(T - T_\infty) \tag{4.6}$$

where the heat transfer coefficient, h, is calculated using an expression derived for a circular heated plate oriented vertically [53]. In both Equations (4.5) and (4.6), the temperatures of surrounding surfaces and surrounding gas were assumed to be equal to the room temperature T_∞.

The heat release in the chemical reaction leading to ignition was described by a simple Arrhenius term assuming a zero order reaction:

$$\dot{Q}_{chem} = Zm\triangle He^{(-E_a/RT)} \tag{4.7}$$

where ΔH is the gravimetric heat of the thermite reaction, R is the universal gas constant, and Z and E_a are the pre-exponent and activation energy, respectively. The oxidation of the excess aluminum with air was neglected for the reactions leading to ignition of the consolidated samples. The activation energy, E_a, =106.2 kJ/mol was obtained from the heated filament experiments for unconsolidated powders described elsewhere [14, 54]. The activation energy for the process leading to ignition should not be affected by particle morphology or for consolidated samples. The kinetic preexponent, Z in units of sec^{-1}, was treated as an adjustable parameter since it is more likely to change with experimental condition. This pre-exponent defining the rate of heat release per gram of material is not directly comparable to the pre-exponent introduced in ref. [54] describing ignition of the powder-like material and normalized per unit of particle surface. Furthermore, even for unconsolidated nanocomposite thermite powders, the external particle surface is of little significance because the thermite reaction occurs at the Al-metal oxide interfaces existing within the particles. Thus, the comparison between pre-exponents characterizing the wire ignition experiments of unconsolidated powders [14] and present laser ignition experiments of consolidated samples can only be made assuming the average dimension of the oxide inclusions to be the same in both cases, as further discussed below. It should be noted that using Equation 4.7 does not imply that a specific zero-order chemical reaction can be identified as responsible for thermal initiation of the prepared materials. Instead, Equation 4.7 should be considered as the simplest possible description for a process that likely includes several different overlapping reactions. This simplified description can only predict reasonable initiation behavior for a limited range of experimental conditions. In the future, it can be compared with data obtained using a broader range of experimental conditions (especially, heating rates) in order to derive a more complete and detailed description of the reactions responsible for thermal initiation in these composite materials.

4.4 Results

The measured thermal diffusivity as a function of pellet density is shown in Figure 4.5. Each point represents the average of three measurements for a particular pellet. Generally, the thermal diffusivity seems to increase with higher density pellets and levels off at about 85 – 90% TMD. There is substantial scatter in the experimental values, most likely associated with minor non-homogeneities in the consolidated samples.

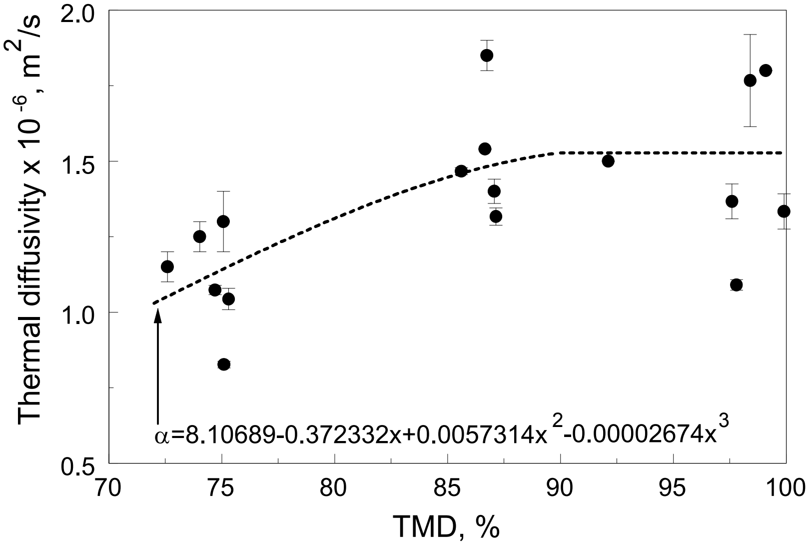

Figure 4.5 Measured thermal diffusivity as a function of pellet density for $8Al{\cdot}MoO_3$ pellets. The trendline used to estimate the thermal diffusivity for pellets used in ignition experiments is shown by a dashed line. Laser power used is 11±1 W with a pulse of 50 ms.

The thermal diffusivity was not measured for each individual pellet used for ignition experiments because mounting the thermopile on the back of the pellet is a tedious and time consuming procedure. Additionally, the thermopile would have to be removed prior to the ignition experiments to prevent it from being destroyed. Therefore, a dashed trendline following the experimental data shown in Figure 4.5 was used to estimate the thermal diffusivity for the pellets used in ignition tests. The trendline is a combination of a polynomial fit used for pellets with up to 90% TMD (the equation is given in Figure 4.5) and a constant value for the pellets with greater densities.

In order to validate the heat transfer model, experiments were performed using inert pellets composed of blended Al and Al_2O_3 powder. As for the reactive material pellets, their thermal diffusivities were measured using the flash method. Following the thermal diffusivity measurements, the laser power was increased to the levels used in ignition experiments and the temperature rise at the back of the pellet was recorded. A characteristic example of a recorded temperature profile is shown in Figure 4.6.

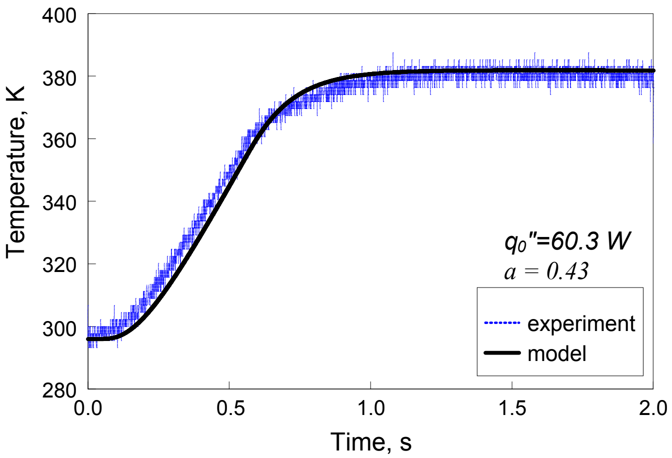

Figure 4.6 Experimental and calculated temperature rise on rear surface of an inert $Al \cdot Al_2O_3$ pellet with 97.32% TMD using a laser pulse of 500 ms.

The zero-time corresponds to the instant when the laser beam was turned on. Also shown is the numerically calculated temperature rise. Adjustment of the absorption coefficient was needed to achieve the match of the measured and calculated curves as shown in Figure 4.6. Based on several measurements of different pellets, it was found that the absorption coefficient varied from 0.30 to 0.43. An average value of the absorption coefficient was close to 0.40 and it was used to interpret the ignition delay measurements for which no experimental pellet temperature profiles were available.

A typical temperature trace for the back side of an igniting reactive pellet is shown in Figure 4.7. As in Figure 4.6, the zero time corresponds to the instant when the laser beam was turned on. For the period slightly exceeding the first half of a second, the pellet temperature is slowly increasing, very similar to the behavior observed for the inert material in Figure 4.6. Moreover, this initial, relatively slow increase is followed by a rapid temperature jump. This jump signifies ignition for the rear surface layer of the pellet, where the thermocouple was mounted. The solid line shows a calculated temperature at the back of the pellet with the chemical reaction heat flow turned off. As in Figure 4.6, the value of absorption coefficient is adjusted to match the experimental trace. Following this match, the chemical reaction was turned on in the model and the value of the pre-exponent Z was adjusted to predict a temperature jump on the front surface of the pellet coinciding with the photodiode spike from the experiment. The time difference for ignition between the front and rear surface was 25-35 ms. This procedure was repeated for several recorded temperature traces yielding effectively the same pre-exponent equal to $6 \cdot 10^9$ s^{-1}. This value was used in all further calculations.

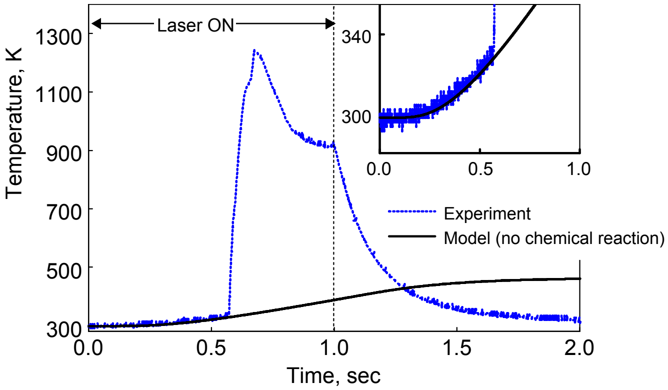

Figure 4.7 Experimental and numerical temperature rise at rear surface for reactive 8Al·MoO_3 pellet with 98.70% TMD.

With all the model parameters defined, temperature distributions inside the pellet heated by the laser beam can be examined until the ignition moment. Characteristic temperature traces predicted for the pellets ignited when heated by the laser beams with different powers are shown in Figure 4.8. It is apparent that significant temperature gradients can exist across the pellet. For high density pellets (~95%TMD), depending on the laser power, the temperature difference between the front and rear surface can be up to 200 K near the ignition point. At the front surface, the heating rates reach about 1000 K/s. At such heating rates, the heat contribution due to the chemical reaction becomes significant at about 500 K. Temperature runaway is clearly observed for both front and rear surfaces of the sample. This rapid increase in temperature is associated with ignition. The time when the temperature runaway occurs at the front surface of the pellet can be directly correlated with the instant the optical emission spike (cf. Figure 4.2) is detected experimentally.

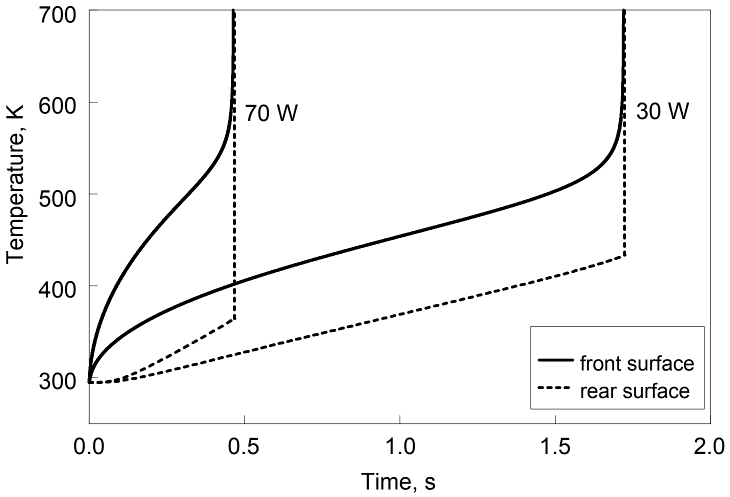

Figure 4.8 Calculated temperature profiles of the front and rear surfaces of an 8Al·MoO$_3$ pellet (95.63 % TMD, 0.25 inch diameter, 0.078 inch thickness) at two laser powers.

The ignition delays measured as a function of the laser power for the pellets consolidated to the same density (95% TMD) are shown in Figure 4.9. A clear trend of reduced delays at greater laser powers is visible despite the scatter among experimental data points. The scatter is most likely due to the combined effects of slight variations in the sample thermal diffusivity and in the laser beam absorption efficiency. Ignition delays measured for the same laser power for the pellets consolidated to different densities are shown in Figure 4.10. Again, despite substantial scatter in the data, a trend of increasing ignition delays for higher density samples is observed.

The numerical model with its adjustable parameters identified as described above was used to predict the trends presented in Figures 4.9 and 4.10. Respective calculated curves, using Z= 6·10^9 s^{-1} and a=0.4 and taking into account variation in the pellet thermal diffusivity as a function of density (cf. Figure 4.5) are shown as solid lines. It is observed that the numerical model describes the experimental points fairly well for the effects of both laser power and pellet density.

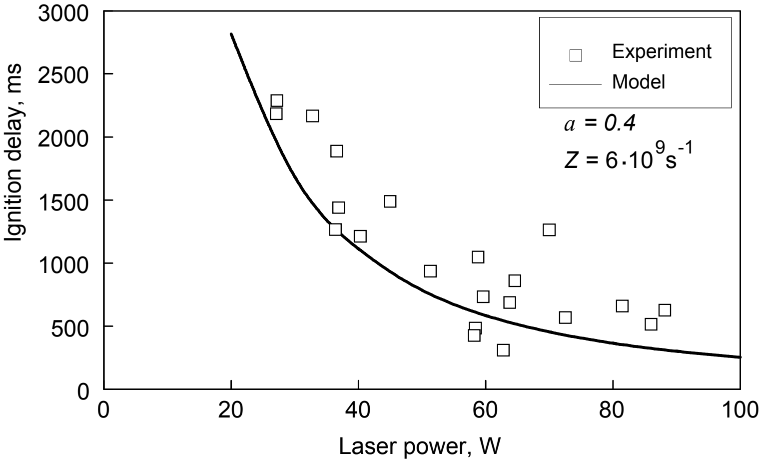

Figure 4.9 Experimental and numerical data points for ignition delay versus laser power of 8Al·MoO$_3$ pellets of 95±0.66 %TMD.

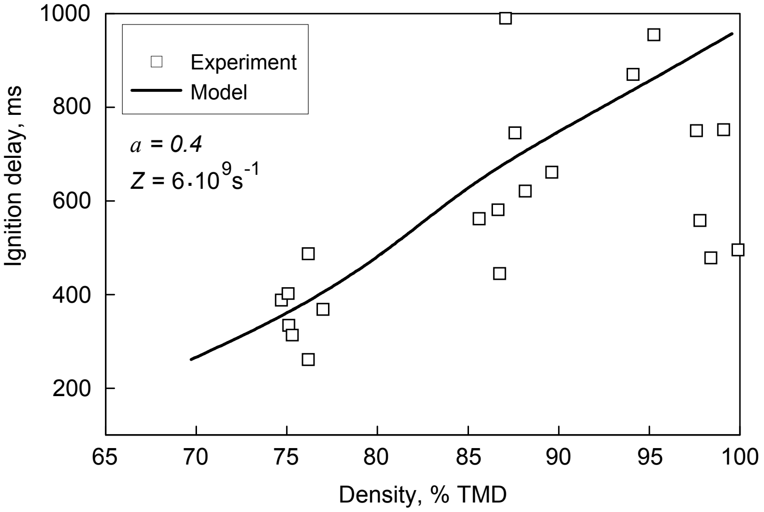

Figure 4.10 Experimental and numerical data points for ignition delay versus pellet density of 8Al·MoO$_3$ pellets using laser power of 49±0.7 W.

4.5 Discussion

Despite a generally good match of the experimental and predicted trends describing the effects of laser power and pellet density on the ignition delays, substantial scatter in the experimental data is observed. The reasons for this scatter were considered taking into account various experimental errors affecting the final definition of the ignition delay. In addition to substantially varied thermal diffusivity determined by the flash method and variation in the laser absorption, parameters affecting the anticipated ignition delay include the pellet mass, thickness, and specific heat. The effect of the latter three parameters, varied within the ranges determined by the accuracy of their respective measurements (or estimates, for the specific heat), on the measured ignition delay was found to be less than 5 %. Thus, apparent random variations in the measured ignition delays are most likely due to the changes in the thermal diffusivities of the prepared pellets and due to some scatter in their laser absorption coefficients.

It is interesting that the activation energy of 106.2 kJ/mol used to describe ignition of unconsolidated powders [14] was also found to be suitable for description of ignition of pellets investigated in this paper. Furthermore, this relatively low activation energy is, within the accuracy of its identification, the same as the activation energy (~ 90 kJ/mol) found in ref. [55] from the thermo-analytical investigation of low-temperature exothermic processes in the nanocomposite powders similar to those consolidated in this study. Therefore, it is reasonable to conclude that the low-temperature exothermic process resulting in broad humps observed in the measured DSC traces is the process governing ignition in the prepared reactive materials. This process was suggested to be controlled by the rate of MoO_3 decomposition rather than diffusion in the growing alumina layers [55]. The conclusion about the critical role of oxide decomposition as the rate limiting process for ignition of nanocomposite thermites is consistent with the recent report [56] dealing with nanocomposite thermites prepared by mixing respective nanopowders.

Finally, it is interesting to compare the pre-exponent Z (units: s^{-1}) treated as an adjustable parameter in the present study with the pre-exponent obtained to describe ignition of respective unconsolidated powders on an electrically heated filament. Note that the model developed to describe ignition of unconsolidated powders [54] and used to process data reported in ref. [14] considers an exothermic surface reaction, whereas Equation (4.7) implies a gravimetric heat release. In other words, the reaction is considered to occur homogeneously within the prepared particles, which is equivalent to assuming that within each composite particle, the reactive interfaces between Al and MoO_3 are well developed and distributed uniformly. Respectively, the pre-exponent factor Z^* (units: $kg \cdot m^{-2} \cdot s^{-1}$) obtained from processing the powder ignition data from ref. [14] was further multiplied by the reactive interface area per individual particle, A_r, and divided by the particle mass, m_p, to be directly compared to the value of Z used in Equation (4.7). The reactive interface area depends on the size of MoO_3 inclusions in the nanocomposite powder; at the same time, greater reactive interface area results in a respectively smaller value of Z^* obtained from the heated filament ignition data processing [14]. Therefore, the value of the corrected pre-exponent $Z^* \cdot A_r / m_p$ expressed in the units of s^{-1}, as in Equation 4.7, does not depend on the size of inclusions or on the assumed reactive interface area.

Using the measured particle mean size, coating thickness, and thermal diffusivity, the value of corrected pre-exponent $Z^* \cdot A_r / m_p$ was $2.2 \cdot 10^9$ s^{-1}. The value of pre-exponent Z obtained as an adjustable parameter in the laser ignition model for pellets was of the same order of magnitude, $6 \cdot 10^9$ s^{-1}. Considering possible inaccuracies in identification of the particle size, powder thermal diffusivity, and coating thickness, the obtained values for the pre-exponents are reasonably close to each other and could represent the same reaction causing ignition in both nanocomposite powder and respective consolidated samples.

4.6 Conclusions

Mechanically sound and chemically reactive consolidated cylindrical samples of nanocomposite thermite $8Al{\cdot}MoO_3$ were prepared by uniaxial die compression of respective powders manufactured by arrested reactive milling. Thermal diffusivity was found to be a weak function of the pellet density. Pellets were ignited by a defocused CO_2 laser beam and the reaction was accompanied by pellet disintegration and violent combustion of the produced fragments. An experimental technique was developed to find ignition delay as a function of the laser power and pellet density. A numerical model was created to describe the heat transfer in the pellet and quantify the chemical reaction leading to its thermal initiation. Experimental ignition delays for different laser powers and pellet densities as well as the pellet temperatures prior to ignition were adequately described by the proposed thermal initiation model. The nanocomposite materials heated by laser ignited at a relatively low temperature, under 600 K. The prepared pellets were not heated uniformly and the temperature difference between the front and rear surface of the pellet was close to 250 K. The activation energy used to describe the heat release term in the developed model was equal to that found from earlier ignition experiments with unconsolidated nanocomposite $8Al{\cdot}MoO_3$ powders. This activation energy is also consistent with that measured by differential scanning calorimetry for the broad, low-temperature exothermic peak identified for these nanocomposite materials. The respective reaction is suggested to represent the reduction of MoO_3 releasing oxygen for the aluminum oxidation as the rate-limiting process governing the thermal initiation.

CHAPTER 5

THERMAL INITIATAION OF ALUMINUM MOLYBDINUM TRIOXIDE NANOCOMPOSITE MATERIALS PREPARED BY DIFFERENT METHODS

5.1 Introduction

This study was designed as a first step for characterization of reactive interfaces found in reactive nanocomposite powders. Two thermite materials with nominally the same chemical composition, $8Al\cdot MoO_3$, are prepared by different methods and characterized. One material is prepared using ARM [8] and the other by ultrasonically mixing nanopowders [10]. The product of ARM is a fully dense micron-sized powder where MoO_3 forms inclusions with dimensions close to 100 nm in the aluminum matrix. The product of ultrasonic mixing is a blend of two nanopowders commonly referred to as metastable interstitial composite (MIC).

It is expected that the interfaces between Al and MoO_3 are qualitatively different for the two materials considered. In the case of ARM, the metal and oxide inclusions are brought together by mechanically shearing material and pressing freshly formed surfaces against each other. This processing occurs at room temperature, even though a brief local heating caused by dissipation of energy transferred from milling tools to milled powder is possible. Such heating is difficult to quantify, and it is often neglected considering rapid heat transfer into steel milling balls. It is hypothesized that a thin protective layer serving as a precursor of the amorphous oxide forms between the reactive components. Recent thermo-analytical studies suggest that such a layer can be described as a mono-molecular, 0.3 nm-thick alumina [57]. On the other hand, aluminum nano-particles used to prepare MIC are naturally passivated with a 2.5 – 4 nm thick aluminum oxide layer [58]. In addition, Al and MoO_3 nanoparticles in MIC are not pressed against each other as in the ARM-prepared material; instead they form a highly porous composite structure.

The experiments are designed to study and describe quantitatively thermal initiation of the above two materials. The thermal initiation is considered for different heating rates and for different heat sources. Reactions in unconsolidated powders as well as in binderless pellets are considered.

5.2 Materials

The powder prepared by ARM used starting aluminum powder from Atlantic Equipment Engineers, -325 mesh (<45μm) 99.5% pure and MoO_3 powder from Alfa Aesar, 99.95% pure. The product powder had mean, volume-based particle size of 16 μm. ARM processing details are available elsewhere [14].

MIC was prepared by ultrasonic mixing of staring nanopowders in hexane. The aluminum nano-powder was provided by Novacentrix and had nominal size of 80 nm. Based on the manufacturer's specification, 26 mass % of the powder was represented by the passivating surface Al_2O_3 layer. For a 80-nm diameter particle, this means that the thickness of the amorphous alumina layer is close to 3.5 nm. A weight increase of the as-received nano Al observed in a thermogravimetric experiment with the peak temperature of 850 ºC indicated an active Al content of 65%. It is likely that the sample did not oxidize completely, so that the active aluminum content is close to that reported by the manufacturer. The active metal content in nano powder of Al specified by the manufacturer was taken into account when preparing MIC. The molybdenum oxide nano-powder was provided by Climax Molybdenum Co.; it is a mixture of the orthorhombic and monoclinic forms of MoO_3.

5.3 Experimental

Reactions in powder-like materials were characterized by differential scanning calorimetry (DSC) and thermal gravimetry (TG), using a Netzsch Instruments STA 409 PC/4/H Luxx Simultaneous Thermal Analyzer. All samples were heated in an argon flow of 50 mL/min. The furnace was sealed and evacuated until the vacuum gage read to its limit of 1 bar of vacuum. It was then allowed to continue pumping for several more minutes. The pump used is a Welch W series vacuum pump rated at $1x10^{-4}$ mbar ultimate vacuum. It was then filled with argon back to the atmospheric pressure. This procedure was repeated twice. To obtain a baseline for each measurement, each sample heated to the target temperature was cooled to room temperature and reheated again using the same heating program.

Fully and partially reacted samples were investigated using x-ray diffraction (XRD). XRD measurements were performed using a Philips X'pert MRD X-ray diffractometer. Consolidation of the powders was performed using a Carver auto series 25-ton press. Details of consolidation can be found in ref [50]. Pellets prepared for ignition experiments were 6.35 mm (¼") diameter and about 2-3 mm thick.

Ignition behavior of unconsolidated powders was investigated using electrically heated metal filaments coated with the powders tested [54]. Nickel-chromium alloy filaments 440 μm diameter were heated by a DC power supply with adjustable voltage and current. The coatings were prepared using thin slurries of the powders in hexane; the slurries were deposited onto the filament using a thin paintbrush and dried prior to experiments. The temperature of the filament was measured using an infrared pyrometer focused on an uncoated filament surface. The ignition event was detected using a photodiode focused on the powder coating [54].

Figure 5.1 shows a schematic diagram of the laser ignition experiment. The pellet was mounted inside a closed chamber required to contain burning fragments and to produce a detectable pressure jump caused by the pellet ignition. The laser beam entered the chamber through a NaCl window that was typically fractured by the pressure pulse or pellet fragments and replaced after every test. The pressure was measured using a model 113B27 ICP transducer from PCB Piezotronics Inc. A model 480C02 ICP sensor signal conditioner was used with its output connected to a multichannel data acquisition board.

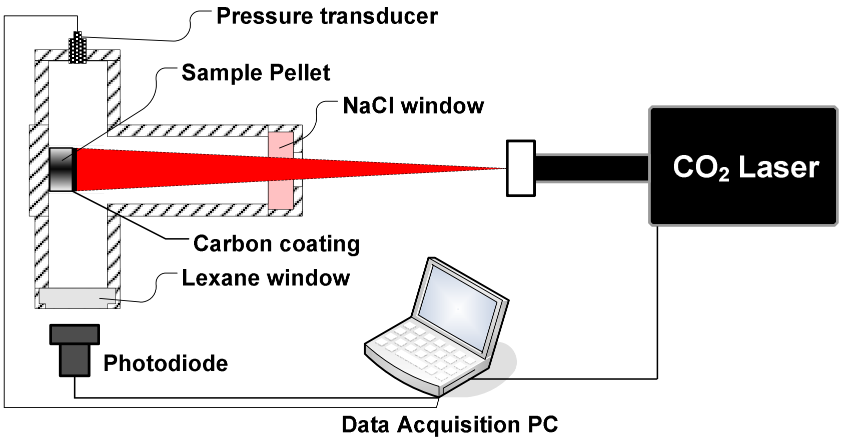

Figure 5.1 Schematic diagram of the experimental setup used to ignite pellets by laser beam.

The pellet was heated from one side by the Evolution 125 Synrad CO_2 laser beam (10.6 μm wavelength). A ZnSe lens (not shown in Figure 5.1) was used to defocus the diameter of the laser beam heating the pellet to make it equal to the pellet diameter. This way the heat flux was applied nearly uniformly to the entire pellet surface. In addition, all pellets were coated with a thin layer of carbon powder to achieve a uniformly enhanced absorption of the laser power independently of the surface properties of individual consolidated samples. A photodiode sensor model DET110 by Thorlabs was positioned perpendicular to the pellet surface and was used to determine the ignition moment accompanied by a strong light emission. The laser-heated pellet surface ignited first, with the following rapid reaction propagation, and disintegration of the entire pellet. In selected tests, a type E thermocouple was mounted to the rear surface of the pellet to record the temperature history of the pellet preceding its ignition.

The thermal diffusivities of different pellets were measured by the flash method [51] using the same CO_2 laser experimental setup. A short heat pulse generated at a reduced laser power was applied to the pellet and the temperature rise at its rear surface was recorded. The time required to reach one half of the maximum temperature at the back of the pellet was used to calculate the thermal diffusivity.

5.4 Results

5.4.1 Thermal Analysis

Figure 5.2 shows the baseline corrected DSC/TG traces for $8Al{\cdot}MoO_3$ ARM-prepared and MIC powders. The samples were heated at 5 K/min. The DSC trace for the ARM-prepared material in Figure 5.2 is consistent with previous measurements [14]. Several exothermic events are observed with the strongest one beginning at about 580 ºC. There is also a broad exothermic event starting just after 100 ºC. A relatively minor and slow weight loss is also observed to start as soon as the material is heated. The weight loss stops at about 500 ºC.

The DSC trace for MIC does not show a low-temperature broad exothermic event as observed for ARM-prepared powder. There is a reproducible weak hump starting at ~150 ºC, which is better observed in the inset in Figure 5.2. In an earlier paper [59], an onset temperature of 265.5 ºC for an exothermic reaction is reported for a similar material heated at 10 K/min in argon. A slow weight loss for MIC begins upon heating, similar to that observed for the ARM-prepared powder. However, the weight loss for MIC accelerates at about 170 ºC. By 400 ºC, the weight loss for MIC, although generally small, is twice as big as that for the ARM-prepared powder. The weight loss stops at about 500 ºC, similar to that for the ARM-prepared powder. A strong exothermic peak is observed to begin for MIC at about 420 ºC and its onset correlates with an additional acceleration in the weight loss.

Note that for both materials, the TG traces show a very small weight increase at temperatures exceeding 500 ºC, which is most likely caused by oxidation of the samples with traces of oxygen present in the DSC/TG furnace despite its repeated flushing with argon prior to each experiment.

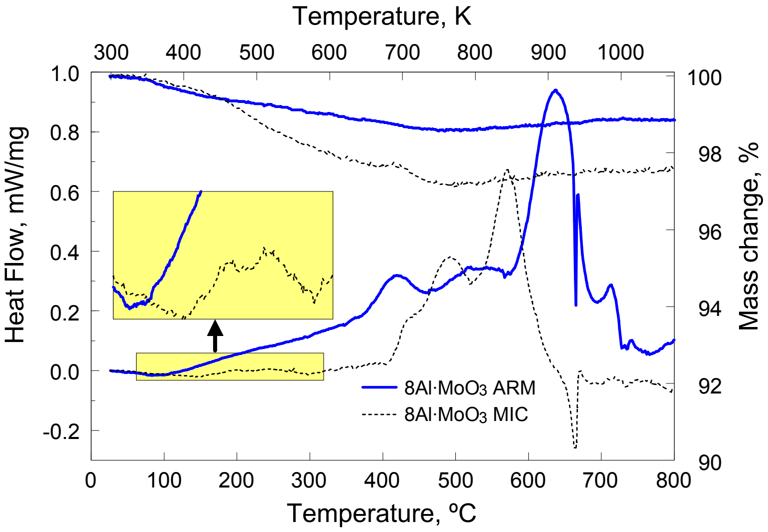

Figure 5.2 DSC/TG of ARM and MIC materials in pure argon flow at 5 K/min.

To understand the mechanisms of reactions occurring at low temperatures, several samples were heated to pre-selected temperatures, cooled off, and examined using XRD.

For the ARM-prepared powder, three samples were analyzed, including an unheated sample, a sample heated to 350 ºC and quenched well after beginning of a broad exothermic event but just before the first relatively sharp exothermic peak was observed in the respective DSC traces, and a sample heated to 800 ºC. The XRD patterns are shown in Figure 5.3.

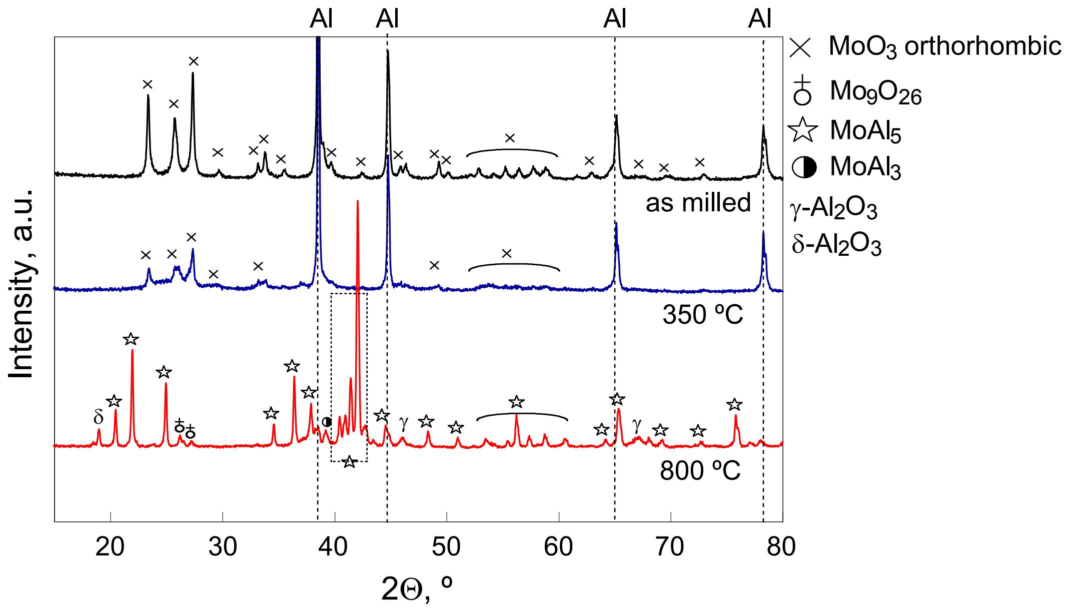

Figure 5.8 XRD traces of ARM-prepared material in progression from as made, heated to 350 ºC, and heated to 800 ºC.

Aluminum and orthorhombic MoO_3 are the only peaks identified for the as milled material. The same peaks are found in the sample quenched at 350 ºC, for which MoO_3 peaks appear weaker and broader. No additional reaction products could be detected. The sample heated to 800 ºC shows several reaction products. The most pronounced peak pattern matched to that of $MoAl_5$ alloy. There is also indication of formation of $MoAl_3$

alloy. Two weak peaks near $2\Theta = 26^{o}$ match most closely with the Mo_9O_{26} pattern. Peaks corresponding to γ and δ alumina are also found.

For MIC, three samples were similarly investigated, including the as-prepared sample and samples heated to 350 and 800 ºC. The temperature of 350 ºC was selected as that following the very first, weak exothermic peak observed in DSC, and the sample heated to 800 ºC was expected to be nearly fully reacted. Respective XRD patterns are shown in Figure 5.4. The pattern for the starting material is substantially more complicated than that for the ARM-prepared powder. Aluminum peaks are clearly visible together with several MoO_3 structures. Interestingly, there is evidence of both hydrated and slightly reduced forms of MoO_3. In ref. [60] it was reported that the nano MoO_3 used displayed hygroscopic and photosensitive behavior. Slightly reduced oxide forms were probably formed due to light exposure while the hydrates could be formed due to exposure to room air. Figure 5.5 shows a narrower range of angles for the XRD patterns shown in Figure 5.4, so that a group of peaks in the 2Θ range of 20 and 30^{o} is better resolved. There are two strong peaks labeled as MoO_x which can be assigned to slightly reduced forms of MoO_3. The sample quenched at 350 ºC indicates loss of $Mo_{17}O_{47}$ peaks, the MoO_x peaks, and the hydrated MoO_3 peaks. A new MoO_3 monoclinic phase is now formed that was not found in the original material. Upon further heating to 800 ºC formation of aluminum oxides becomes evident. Only two alumina phases were identifiable, including δ and γ, polymorphs. Note that δ-alumina is an intermediate structure between γ and α–polymorphs [61]. Also identified were Mo, MoO_2 and Mo_9O_{26}. Additionally, formation of $MoAl_5$ alloy was observed. No MoO_3 was detected in that sample.

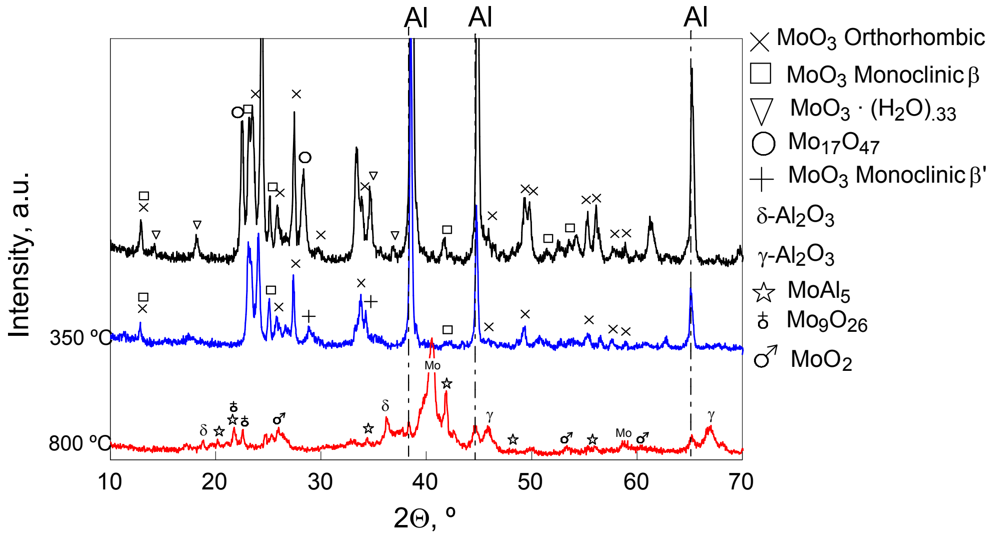

Figure 5.9 XRD traces of MIC material in progression from as made, heated to 350 ºC, and heated to 800 ºC.

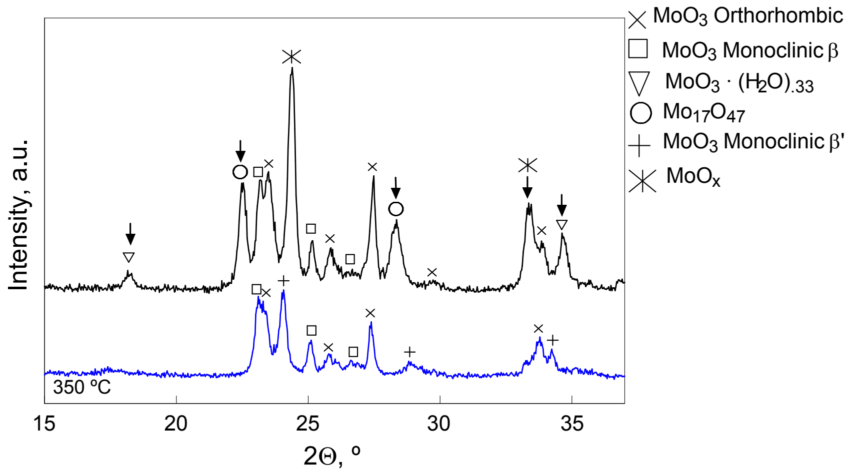

Figure 5.5 XRD of as made and quenched sample showing in detail low angle reflections.

Figure 5.6 shows a set of DSC/TG traces obtained by heating the ARM-prepared powder at different rates. In addition to the broad exothermic event observed for all cases, four exothermic peaks can be identified. Some of these peaks are likely composed of more than one event; for example the second exothermic peak is relatively broad, while its shape is relatively well preserved for different heating rates. The third and strongest peak begins before Al melting and is overlapped with the melting endotherm. All exothermic peaks shift to higher temperatures at greater heating rates, as expected for the thermally activated processes. An additional, relatively small endothermic peak is observed at about 730 ºC, very close to the temperature at which $MoAl_5$ decomposes into liquid Al and $MoAl_4$. All TG curves indicate an early weight loss which stops at about 500 ºC independently of the heating rate. The magnitude of the observed weight loss does not correlate with heating rates.

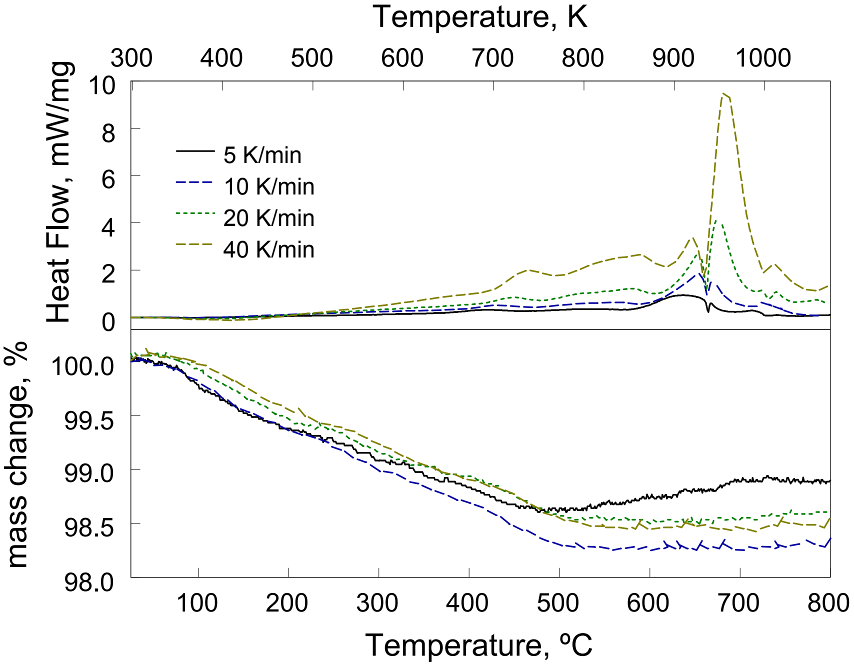

Figure 5.6 DSC/TG results of $8AlMoO_3$ ARM-prepared powder at several heating rates in pure argon flow.

Figure 5.7 shows DSC and TG traces for MIC samples heated at different rates. The low-temperature weak exothermic events are not well distinguished because the experiments were performed with the heating controller operated based on the sample temperature, unlike the experiment presented in Figure 5.6, when the furnace thermocouple was used to control the experiment.

The exothermic peak pattern shifts to higher temperatures when the heating rate increases from 5 to 10 K/min; while no such shift is visible for greater heating rates. Similarly, the shift to higher temperatures is only observed between the TG patterns collected at 5 and 10 K/min, with the other patterns effectively overlapped. For DSC traces, an unusual shift to lower temperatures for the main two exothermic peaks is visible between 20 and 40 K/min. This is likely an indication that the detected peaks are composed of several overlapped exothermic processes. At different heating rates, individual events vary in strength resulting in the changing shapes of the resulting composite peaks, which masks the shift of individual events to higher temperatures at greater heating rates. Aluminum melting peak is clearly detected near 660 ºC, it is relatively broad, consistent with earlier melting measurements for nano-sized Al powders [62]. As for the ARM-prepared materials, the weight losses stop at about 500 ºC, when main exothermic events begin

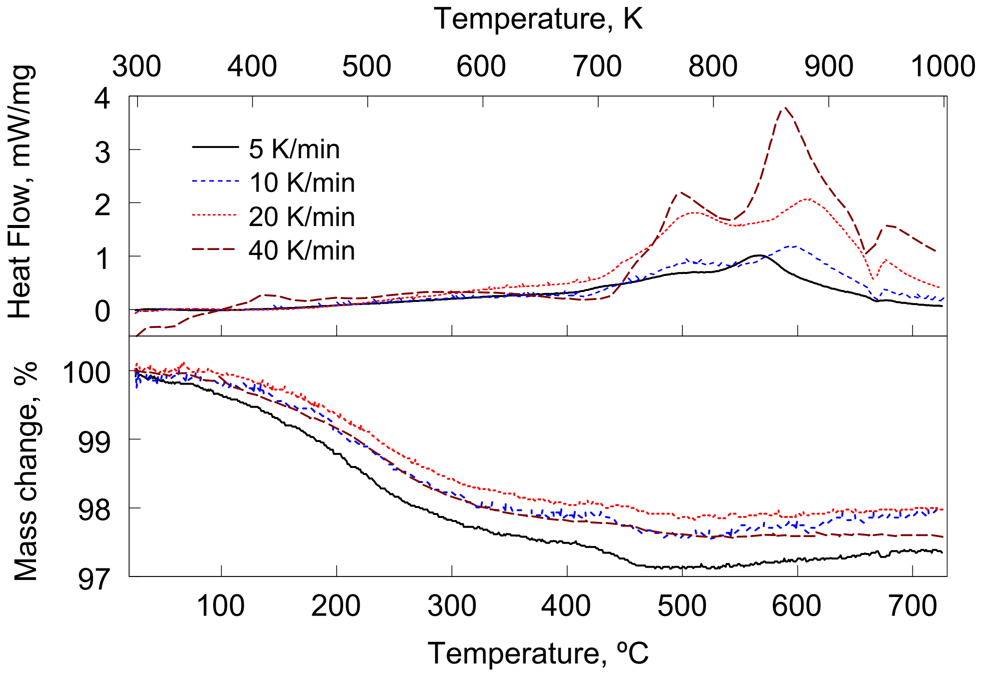

Figure 5.7 DSC/TG curves for MIC powder for several heating rates in pure argon flow.

5.4.2 Heated Filament Ignition

In these experiments, the filament temperature is registered at the instant the powder ignition is detected based on the photodiode signals. In order to compare results for MIC and ARM-prepared powders, it is important to take into account that the particle sizes for these two materials are substantially different. Because of the difference in the particle sizes, the thickness of the coatings formed by these two materials on the nickel-chromium wire was not the same. Based on the electron microscopy of the prepared coated filament samples, it was found that a typical coating for MIC was about 25 µm. For the coarser, ARM-prepared powder, the typical coating thickness was close to 90 µm. A thicker coating results in a greater temperature gradient between the filament and powder. In addition, the filament temperature under the coating is slightly lower than that of the uncoated filament (which is measured optically), with the effect amplified for thicker coatings. To account for such effects, a numerical heat transfer model developed for this experiment [54] was used to calculate the highest temperature in the coating when the filament temperature reached that measured at the ignition instant for different heating rates. The calculations were performed for the coating thicknesses typical of MIC and ARM-prepared powders. Examples of such calculations are shown in Figure 5.8. For both cases shown in Figure 5.8, the heating rate is close to 20,000 K/s. It is observed that under such conditions, the temperature difference between MIC coating and the filament is close to 10 K, while for the ARM-prepared powder this difference reaches about 40 K. Respectively, the filament temperatures measured optically for such experiments need to be corrected accordingly to represent the temperatures of the ignited powders.

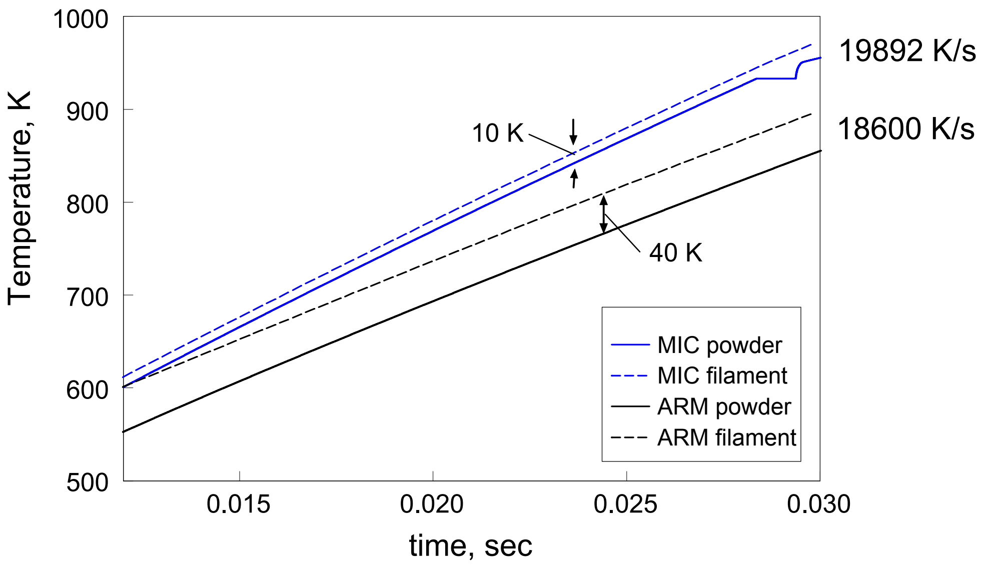

Figure 5.8 Temperature histories for wire filament and powder layer using numerical wire ignition model.

Note that the thermal diffusivity of powder coating is used in calculations; its value was taken as that used in earlier estimates for metal powder coatings, $2.3 \cdot 10^{-7}$ m^2/s. [54] A variation in thermal diffusivity in the range of $1 \cdot 10^{-7} - 5 \cdot 10^{-7}$ m^2/s had negligible effect on the result of calculations considering that in both cases, the coatings were relatively thin.

Corrections obtained by such calculations were applied to shift the measured filament temperatures for ignition experiments with both powders. These corrected ignition temperatures obtained in experiments performed at different heating rates are shown in Figure 5.9. Each data point represents the average of five experimental runs. For MIC, the ignition temperature increases slightly for higher heating rates. An apparent activation energy implied by the shift of ignition temperatures for MIC as a function of the heating rate is 236 kJ/mol, close to the activation energy reported for MIC in ref. [63]. For the ARM-prepared powder, the ignition temperature is nearly constant.

At low heating rates, MIC ignited at a slightly lower temperature; however, as the heating rates increased, ignition occurred at essentially the same temperature for both materials.

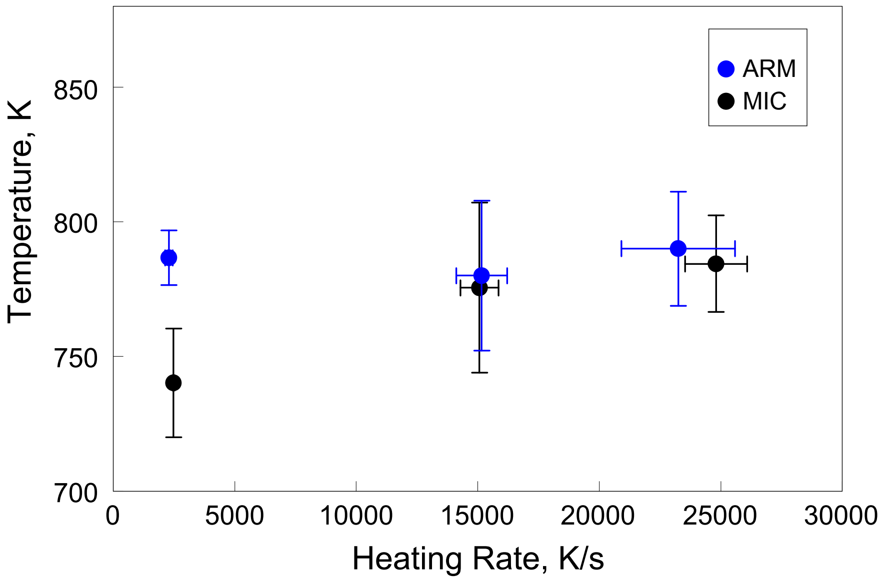

Figure 5.9 Corrected ignition temperatures as function of heating rate from wire ignition experiment.

5.4.3 Comparison of Thermal Analysis and Filament Ignition Experiments

The DSC data from Figures 5.6 and 5.77 as well as the wire ignition data from Figure 5.9 are shown in Kissinger coordinates in Figures 5.10 and 5.11. Figure 5.10 shows the processed results for the ARM-prepared material. Apparent activation energies were obtained from the slope of a straight line fit to each peak. They are shown as labels in Figure 5.10.

For the ARM-prepared material, extrapolating kinetic trends implied by the stronger DSC peaks to higher heating rates points out to the range of temperatures substantially greater than the measured ignition temperatures. A similar extrapolation for the onset of the low-activation energy, broad exothermic hump observed at low temperatures comes close to the experimental range of ignition temperatures. However, because ignition temperatures are not observed to shift as a function of the heating rate, the ignition mechanism must account for additional processes.

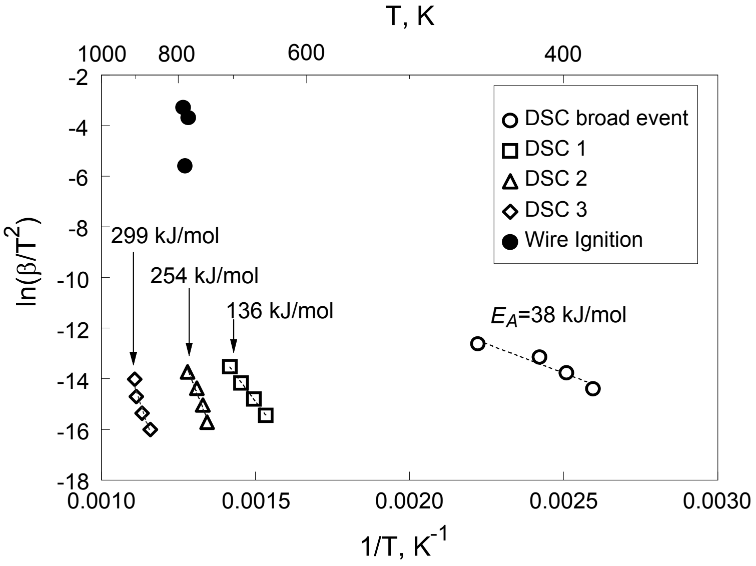

Figure 5.10 Kissinger plot of DSC peaks and wire ignition data for ARM-prepared powder.

Figure 5.11 shows the processed results for the MIC material. The apparent activation energies corresponding to each process are shown as labels. As for the ARM-prepared powders, extrapolation of the DSC kinetic trends to the higher heating rates does not point to the experimental range of ignition temperatures. It is interesting, that similarly to the ARM-prepared material, the ignition temperatures are very close to those at which the most significant exothermic events are measured in DSC traces.

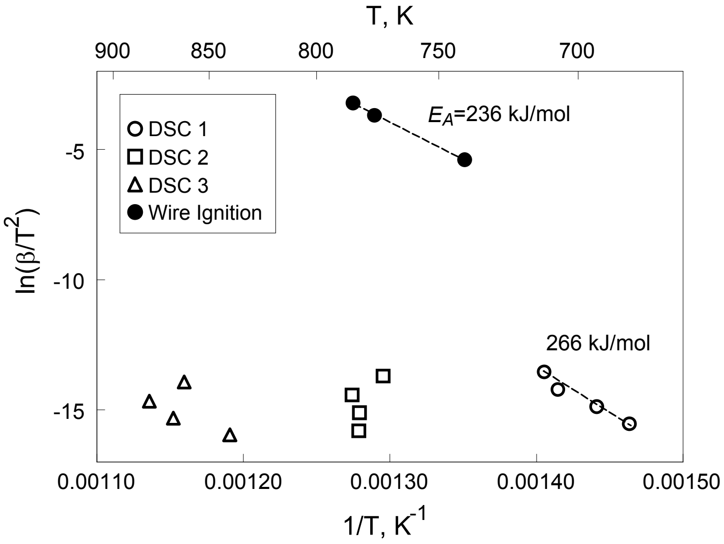

Figure 5.11 Kissinger plot of DSC peaks and wire ignition data for MIC powder.

5.4.4 Thermal Diffusivity for Pellets

Figure 5.12 shows measured thermal diffusivities for the prepared pellets plotted as a function of their densities. Each experimental point is an average of three measurements for a single pellet. Higher densities could not be achieved for MIC pellets despite an increased consolidation pressure. Thermal diffusivity is observed to increase for pellets pressed to greater densities, as expected. The values for MIC pellets are well correlated with the trend observed for the pellets from the ARM-prepared powders.

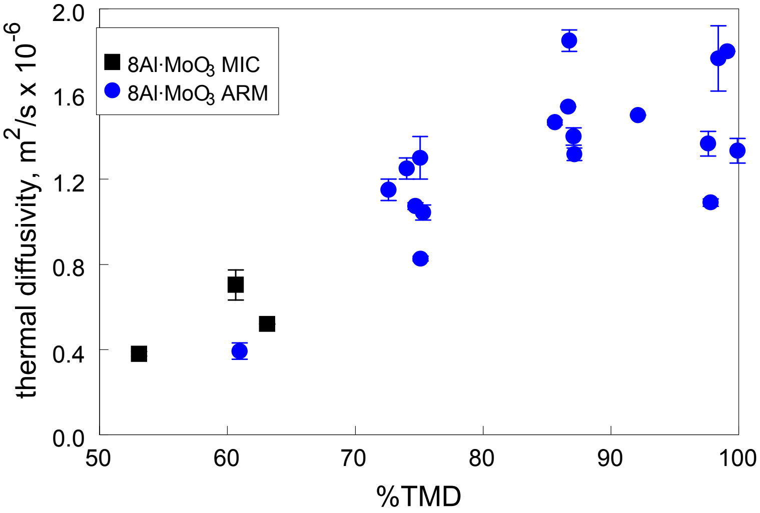

Figure 5.12 Measured thermal diffusivity of MIC and ARM-prepared pellets. The TMD for 8Al·MoO$_3$ is 3.252 g/cm^3.

5.4.5 Laser Ignition Experiments

As noted above, ignition of pellets heated by the laser beam was accompanied by a strong optical emission and pressure pulse. The pellets disintegrated with mm-sized or finer fragments flying inside the experimental chamber. Combustion products were collected and examined using a scanning electron microscope (SEM). Representative SEM images of the collected products for the ARM-prepared and MIC pellets are shown in Figure 5.13. Morphologies of the combustion products are markedly different for the two types of materials. Products of the ARM-prepared pellets contain relatively large alumina spheres with well-distinguished inclusions of Mo. Images shown in Figure 5.13 were taken using a backscattered electron detector, so that metallic Mo inclusions appear significantly brighter than Al_2O_3. In addition, some composite and apparently unreacted particles are detected, which can be readily identified by their non-spherical shapes and lack of the apparent brightness contrast between material components. For the MIC pellets, the products are mostly composed of highly porous agglomerates also made of

Al_2O_3. Metallic Mo inclusions are also observed; typically they are much finer than those detected in the ARM-material products.

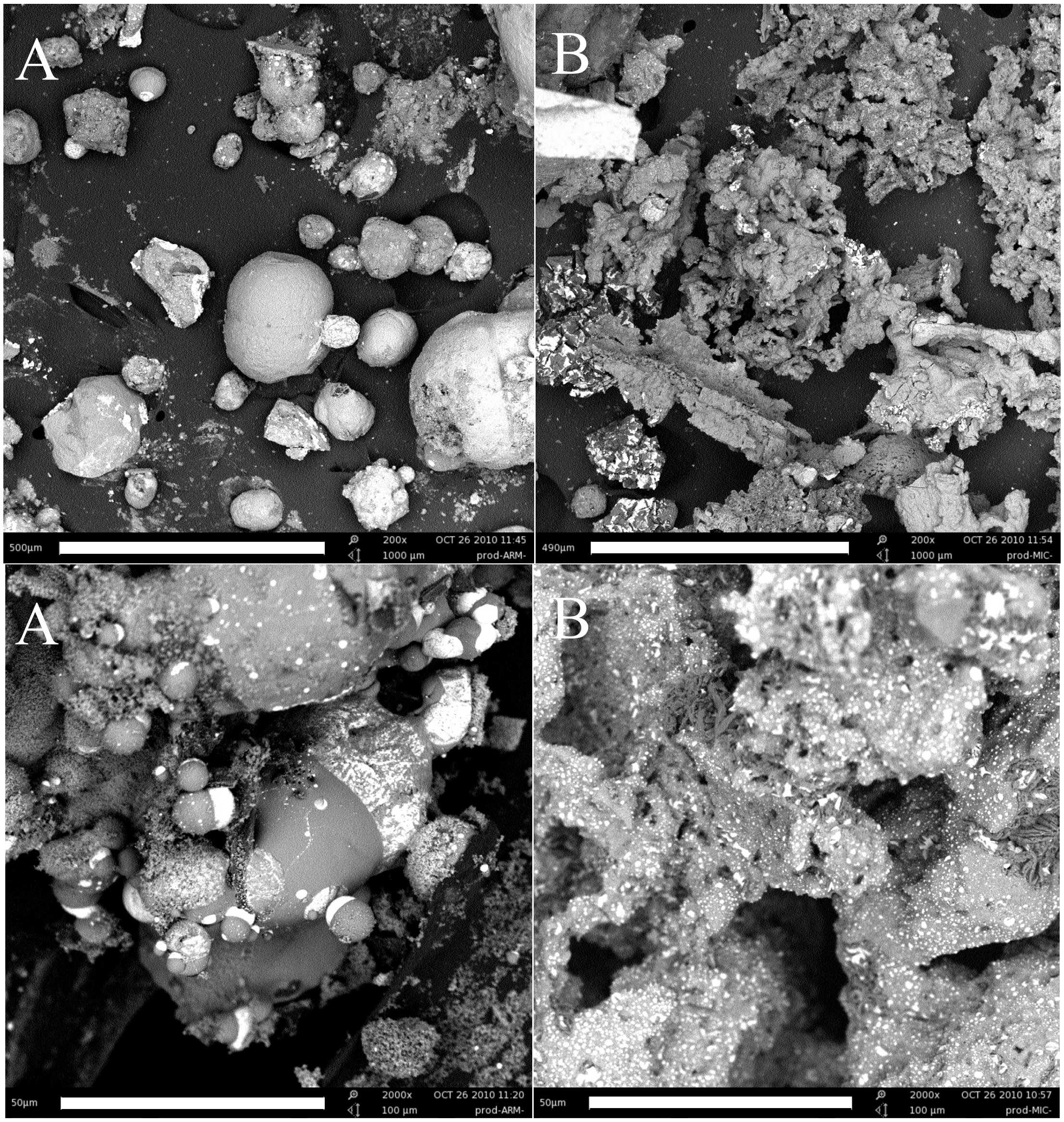

Figure 5.13 SEM images of combustion products for ignited pellets of A) ARM-prepared material and B) MIC material.

Characteristic pressure transducer and photodiode traces recorded in laser ignition experiments are shown in Figures 5.14 and 5.15 for the pellets consolidated using the ARM-prepared powder and MIC, respectively. Both pressure and emission traces show significant spikes upon ignition, with the photodiode signals saturated for both experiments. Time zero corresponds with application of laser beam. Note that weak pressure and photodiode pulses are observed in Figure 5.14 coinciding with application of laser beam; these signals were produced by igniting carbon coating placed on the pellet surface. Both pressure and photodiode signals return to their baseline values as the pellet continues to be heated prior to its ignition.

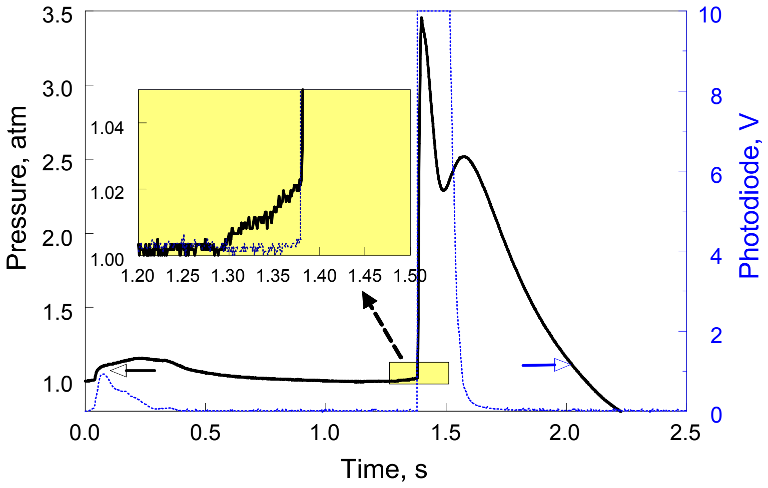

Figure 5.14 Pressure and photodiode traces recorded in a laser ignition experiment with pellet of consolidated ARM-prepared powder. Pellet density is 98.86% of TMD.

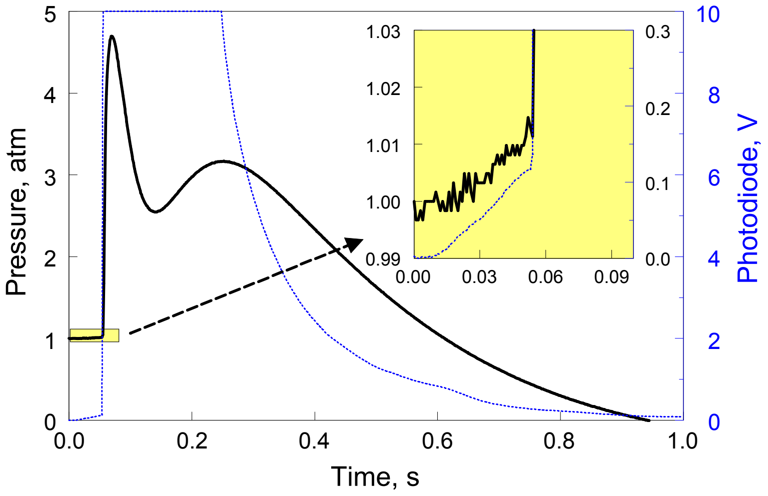

Figure 5.15 Pressure and photodiode traces recorded in a laser ignition experiment with pellet of consolidated MIC. Pellet density is 62.91% of TMD.

Generally, the ignition delay is shorter for the MIC pellet, which has substantially lower density. The pressure pulse is slightly higher for MIC pellet as well.

Differences in measured pressures and rates between the MIC and ARM-prepared material are consistent with the differences in the appearance of their respective combustion products (cf. Figure 5.13). The combustion products of the ARM-prepared materials contain relatively large particles that would form after an extended period of combustion of respectively large composite fragments. Alumina particles and large Mo inclusions are round in shape, indicating that the surface temperature of the entire fragment exceeded the melting points of both alumina (2072 ºC) and molybdenum (2623 ºC). Because of a long combustion time, such fragments are unlikely to result in a sharp and strong pressure pulse. Alternatively, the alumina agglomerates found in MIC products are not spherical; instead, they have developed specific surface. These shapes indicate that the entire agglomerates were unlikely to be heated above the alumina melting point. Instead, MIC likely reacted rapidly, due to the initially available large metal surface exposed to oxidizer; while the formed products were effectively cooled by the surrounding gas. As a result, formed alumina particles were solid or agglomerated and solidified before forming spherical droplets.

Insets in Figures 5.14 and 5.15 show expanded time and vertical scales for the portions of the traces immediately preceding ignition. It is interesting that for both pellets, a small pressure increase is measured shortly before the pellet ignites. For the ARM-prepared material, this pressure increase begins approximately 90 ms before the main ignition pulse. For MIC, this pressure increase begins just after the laser is turned on. It is interesting that for the ARM-prepared material, the initial pressure increase is not accompanied by detectable optical emission. Comparatively, for MIC, the optical emission is clearly detected and correlated with the initial pressure climb.

Figure 5.16 shows ignition delays measured in the laser ignition experiments as a function of the pellet density. Scatter in the experimental measurements is likely attributed to variance in both thermal diffusivity and surface absorption for different pellets. For similar (low) densities, the ignition delays are close to each other for MIC- and ARM-prepared pellets. Experiments with the ARM-prepared pellets available at a wider range of densities show that the ignition delays increase for greater densities. Higher laser power appears to result in shorter ignition delays for both materials at similar densities.

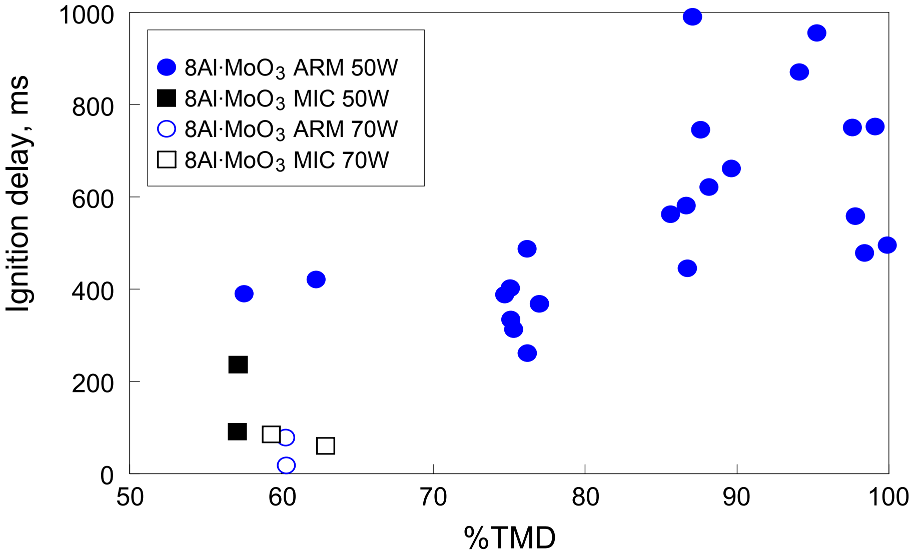

Figure 5.16 Measured ignition delay as a function of pellet density using laser power of 49±0.7 W.

In selected experiments, a thermocouple was mounted at the back surface of the ignited pellet, so that the temperature increase prior to ignition could be measured. An example of the temperature trace measured for a pellet consolidated to 95.6 % of TMD using the ARM-prepared powder is shown in Figure 5.17. Ignition is accompanied by a strong temperature spike, while the temperature increase prior to this spike is very low but clearly measurable. A solid line in Figure 5.17 shows the temperature calculated for the back of the ARM-pellet using a simplified heat transfer model. The model considers a cylindrical geometry with the front surface of the pellet exposed to the laser heat flux as well as radiation and convective losses. The circumferential and rear surfaces are assumed to have adiabatic boundary conditions. Since there is no radial temperature gradient, the model analyzes a simple transient 1-D heat transfer along the pellet axis. Thermal diffusivity used in the model was obtained from the laser flash measurements. Specific heat was calculated using material composition and its measured density. The absorptivity of the carbon-coated pellet surface was assumed to be 0.4 based on earlier experiments [43]. The heat transfer model was validated comparing predictions and measurements for a pellet prepared from blended Al and Al_2O_3 powders, for which no chemical reactions could have occurred upon heating.

For MIC pellets and for low-density pellets prepared using ARM-made powders, no temperature increase at the back of the pellet could be detected, which was not surprising considering their low thermal diffusivities.

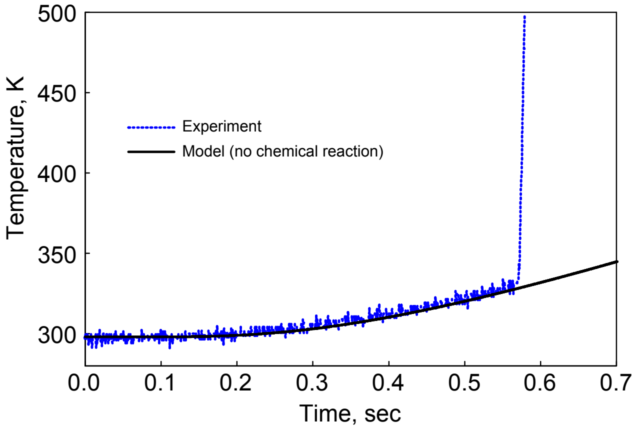

Figure 5.17 Measured and calculated temperatures at the back of the pellet consolidated from the ARM-prepared powder. The pellet density is 95.6% of TMD and laser power is 50 W.

Because of a good match between predicted and measured temperatures at the back of the laser-heated pellet, the calculations were used to analyze the temperature distributions in such pellets during the experiments. The calculations were also performed for the low-density pellets, for which no direct temperature measurements were available. Thus, calculated temperatures for the laser-heated pellet surfaces are shown in Figure 5.18 for two specific ignition experiments with laser powers of 51 W and 50 W for MIC and ARM pellets, respectively. The temperatures are shown as a function of Fourier number defined as $F_o = \alpha t / l^2$ where α and l are respectively thermal diffusivity and height of the pellet, and t is time. The moments of ignition obtained from the photodiode traces are illustrated by vertical arrows. For the specific examples shown in Figure 5.18, the laser heated surface of the igniting MIC pellet is close to 600 K, while the surface of the igniting pellet made of the ARM-prepared material is slightly greater than 500 K. The same calculations predict the temperature distributions across the heated pellets, as shown in Figure 5.19. In agreement with the experiments, there is effectively no temperature increase at the back of the MIC pellet at the moment it ignites.

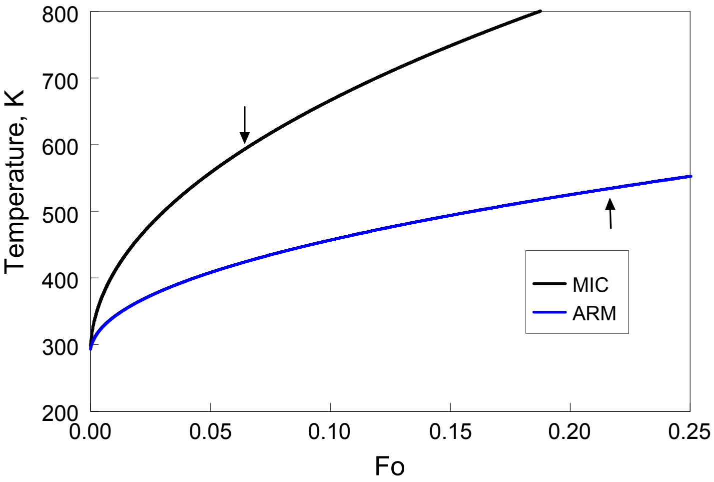

Figure 5.18 Calculated temperature history of front surface of pellet in nondimensional time. The MIC pellet density was 57.15% of TMD and the ARM material pellet density was 98.70% of TMD.

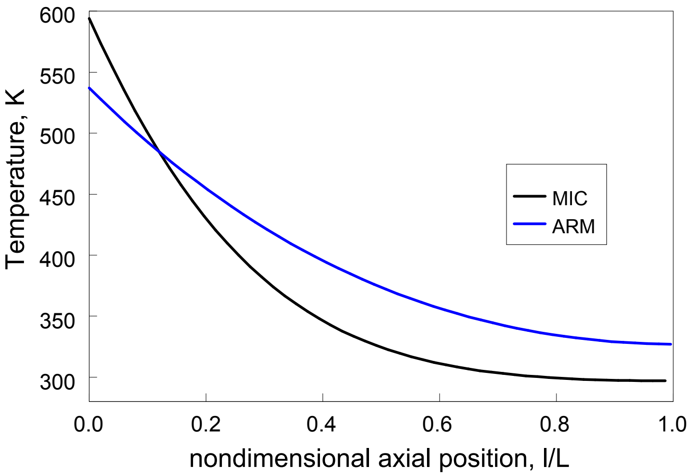

Figure 5.19 Calculated temperature distribution across pellet at the time of ignition.

Similar calculations were performed to simulate experiments with different laser powers and using respective experimental ignition delays to identify the temperature profiles in igniting pellets. For MIC pellets, the laser heated surface ignited when its temperature was predicted to be in the range of 480 – 590 K based on the three experimental data points. For ARM pellets, the temperatures varied in the range of 510 – 545 K.

The laser ignition experiments can also be presented considering the total pressures measured in the ignition chamber. Figure 5.20 shows the maximum pressures recorded as well as the maximum rate of pressure rise as a function of pellet density. Clearly, higher pressures are observed for the MIC pellets.

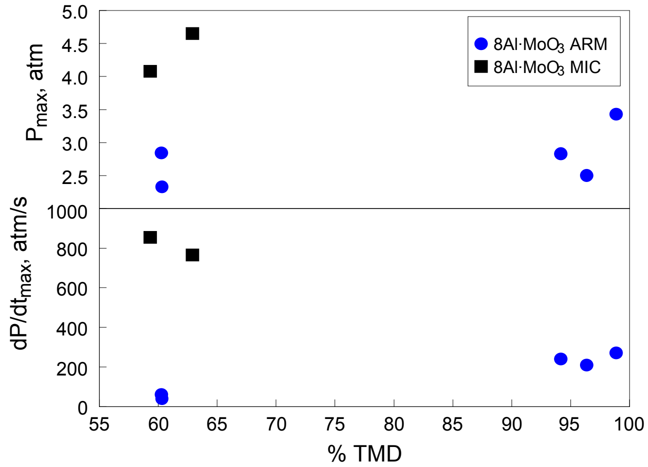

Figure 5.20 Measured pressure and rate of pressure rise from constant volume pellet combustion as function of pellet density.

5.5 Discussion

An initial motivation of this effort was to trace the effect of possible differences in the nature of the interface separating Al metal from MoO_3 on the thermal initiation in differently prepared Al·MoO_3 nanocomposite materials. Indeed, DSC traces for MIC and for ARM-prepared materials show substantial differences in the low-temperature reactions. For the ARM-prepared materials, for which Al surface is not covered by the naturally-grown amorphous alumina layer reactions at low temperatures are more significant. [57] Although, these reactions are relatively slow. The thickness of the Al_2O_3 layer that should grow at the Al/MoO_3 interface to account for the released heat can be roughly estimated assuming a fixed dimension for the MoO_3 inclusions embedded in the

Al matrix. Approximating the MoO_3 inclusions by 100 nm spheres surrounded by Al_2O_3, the thickness of the alumina that needs to grow to account for the measured heat release occurring up to about 400 and 500 ºC is between 2 and 4 nm. Therefore, by the time the main exothermic peaks are observed in the DSC traces for both ARM-prepared materials and MIC, the differences in the nature of the Al/MoO_3 interface are no longer as significant as for the as-prepared materials.

As noted from the DSC and TG traces shown in Figures 5.2, 5.6, and 5.7, the initial sample heating is also accompanied by a small, but not negligible weight loss. This weight loss consistently observed to continue to up to about 500 ºC, which is a higher temperature than could be associated with losses of the absorbed moisture. It is also interesting that the weight loss is observed for both materials, while relatively little to no absorbed moisture is expected for the ARM-prepared composite. As XRD patterns collected for samples heated to 350 ºC show (Figures 5.3 – 5.5), the main change observed for both materials has to do with partial decomposition of MoO_3. Thus, it is reasonable to suggest that the main cause for the observed weight loss is the decomposition of MoO_3 accompanied by release of gaseous oxygen-containing species. The weight losses stop at the temperatures close to the onset of the main exothermic peaks observed in the DSC traces. This can be interpreted considering that at those temperatures, Al becomes a more active reagent and reabsorbs released oxidizing molecules more efficiently than it does at lower temperatures.

It is interesting that main exothermic peaks observed by DSC and the end of the measured weight losses occur at similar temperatures for both materials. Furthermore, the ignition temperatures measured in the filament ignition experiments are also very close to each other for both materials and effectively coincide with the temperatures at which the main exothermic events are observed in the DSC experiments. The effect of heating rate on the ignition temperatures is weak or ambiguous, so it is possible that all three events discussed above, including the strong exothermic peaks in the DSC signals, stopped weight losses measured by TG, and ignition of powders coated on the heated filaments are associated with a thermodynamically rather than kinetically driven change in the properties of the Al/MoO_3 interface. One such change can be transformation of the amorphous Al_2O_3 into a crystalline polymorph (e.g., γ-Al_2O_3) reported to occur in vicinity of 500 ºC [62, 64, 65]. This polymorphic phase transition results in a substantial change of the diffusion resistance of the growing alumina and was recently confirmed to be important for ignition of Al particles [65]. Formation of boundaries between individual Al_2O_3 crystallites would substantially accelerate transport of oxidizer to the metal surface in the composite materials as well, which can explain a significant increase in the Al reactivity. This explanation allows one to understand a relatively minor difference in behaviors of MIC and ARM-prepared materials in the heated filament ignition experiments despite substantial differences in the DSC traces. Indeed, assume that in the ARM-prepared materials, the surfaces of Al and MoO_3 are separated by a very thin Al_2O_3 layer (or its precursor). Despite its limited thickness, this layer represents a diffusion barrier preventing the self-sustaining redox reaction. Upon heating, the transport of reagents through this layer remains slow explaining a relatively weak exothermic reaction detected at low temperatures. For MIC, the initial Al_2O_3 layer is thicker and so the low-temperature exothermic reaction is barely detectable. However, when the amorphous alumina becomes unstable and transforms into γ-Al_2O_3, the grain boundaries are produced in both materials accelerating ensuing mass transfer and redox reaction.

The above reasoning cannot be used directly to interpret the observed similar temperatures to which the pellet surfaces are laser-heated prior to ignition for both MIC and ARM-prepared materials. These temperatures are calculated (cf. Figure 5.18) using the laser power and the experimental thermal diffusivities of the prepared pellets. The specific values of the initiation temperatures for both materials are close to 500 K, which is substantially lower than observed in the filament ignition tests. This discrepancy can be addressed considering the following three points.

First, the temperature of the laser-heated pellet surface implied by calculations (as shown in Figure 5.18) does not account for the heterogeneous exothermic reactions, such as observed to occur in DSC experiments under 500 K. These reactions are expected to increase the pellet surface temperature, although it is unlikely that the increase will be of the order of 300 K, which would make the laser ignition data consistent with the heated filament experiments.

Another factor that could affect the ignition temperature is that the individual particles in pellets used in the laser ignition experiments were mechanically deformed during consolidation. Thus, protective surface layers, e.g., alumina films, could have been sheared and damaged. This damage could result in an altered kinetics of the amorphous to γ-Al_2O_3 phase change and in an earlier deterioration of the protective properties of alumina.

Finally, it should be taken into account that substantial gas release from the heated pellet occurs prior to its ignition, as supported by the measured pressure traces indicating a pressure increase before the main ignition pulse (see insets in Figures 5.14, 5.15). This gas release can damage the integrity of the pellet's surface and result in production of separated fragments, especially, for lower density pellets, such as prepared with MIC. These phenomena substantially reduce the conductive heat transfer to the back of the pellet and thus can result in a significantly greater heating of the pellet surface. In fact, the correlated increase in both pressure and optical signal measured for the laser-heated MIC pellet prior to the ignition pulse (Figure 5.15) is indicative in production of fine burning fragments emitted from the pellet surface. Such fragments can be easily heated substantially higher than predicted by the present calculation.

5.6 Conclusions

Two types of nanocomposite reactive materials with the same bulk compositions $8Al\cdot MoO_3$ were compared to each other. One of the materials was manufactured by mechanical milling (ARM) and the other by mixing of nano-scaled individual powders (MIC). Differences in the interfaces formed between Al and MoO_3 in materials prepared by different techniques resulted in differences in their low-temperature redox reactions well-detectable by DSC. Alternately, when these two types of materials were coated onto an electrically heated filament, their ignition temperatures were nearly identical to each other and were in the range of 750 – 800 K. These ignition temperatures coincided with the temperatures at which main exothermic processes were detected in DSC experiments. In laser ignition experiments performed with consolidated pellets of both materials, MIC pellets produced consistently stronger pressure pulses. The ignition delays were similar for the pellets of both materials prepared with the same porosity. Analysis of the heat transfer in the pellets heated by the laser suggested that the laser-exposed pellet surfaces are heated to approximately the same temperature before ignition for both materials. This temperature was estimated to be close to 500 K, neglecting the exothermic reactions preceding ignition and possible fragmentation of the heated pellets. Taking into account both phenomena is expected to result in a higher surface temperature, which would better represent the experimental situation. It is proposed that the ignition of both MIC and ARM-prepared materials at the same temperature can be explained by a thermodynamically driven transformation of a protective amorphous alumina into a crystalline polymorph.

CHAPTER 6

LOW-TEMPERATURE EXOTHERMIC REACTIONS IN ALUMINUM-COPPER OXIDE NANOCOMPOSITE POWDERS

6.1 Introduction

Recent experiments showed that kinetics of low-temperature exothermic reactions in fully-dense nanocomposite powders differ from the reaction kinetics for the blends of nanopowders with the same bulk composition. For example, thermo-analytical measurements showed that the onset of exothermic reaction for blended thermite nanopowders occurs at the same temperatures as the first oxidation step for aluminum in oxygenated gases [62-64, 66-69]. In both reactions, evolution of the amorphous alumina layers naturally grown on surface of aluminum exposed to air and associated changes in its diffusion resistance were proposed to govern these initial exothermic reactions [68, 69]. These changes are thermally activated and described by conventional Arrhenius kinetics [69]. However, for the fully dense nanocomposite powders, the reaction onset occurs at a lower temperature [14, 55, 70, 71] compared to blended nanopowders. Recent experiments with the fully-dense nanocomposite thermite powders employing a thermal activity monitor (TAM III by TA Instruments) [57] quantified exothermic reactions occurring at very low temperatures, 30 - 100ºC. The effect of temperature on the measured reaction rates could not be explained using Arrhenius type kinetics even when both activation energy and pre-exponent were treated as adjustable parameters [57]. Understanding and quantitative description of such reactions is important and may be directly relevant to describing ignition in such nanocomposite materials.

Unlike relatively well studied amorphous alumina layer growing on the aluminum surface exposed to an oxidizing gas, the interfacial layer between aluminum and solid oxidizer within the fully-dense nanocomposite materials is not well characterized. Such interfacial layers may be substantially thinner than 3 – 5 nm-thick layers of "natural" amorphous Al_2O_3; they may also have different structures and even compositions. For very thin oxide layers separating metal from gaseous oxidizers, aluminum oxidation is conventionally described using Cabrera-Mott reaction model [72, 73], in which mass transfer is accelerated by electric fields formed across the growing oxide films. It was suggested that a similar model may be applied to describe reactions in heterogeneous condensed systems [74], such as fully-dense nanocomposite thermites.

In this paper, the kinetics of the ARM-prepared Al – CuO thermites is studied and interpreted using low-temperature micro-calorimetry and differential scanning calorimetry (DSC) measurements published earlier [70]. A set of microcalorimetry measurements presented in ref. [57] is used and expanded to include higher temperatures (up to 413 K or 140 ºC). Both DSC and microcalorimetry experiments are interpreted using the Cabrera-Mott oxidation mechanism with a new set of kinetic parameters identified for the Al-CuO reactions.

6.2 Experimental

6.2.1 Experimental Details

A nominally stoichiometric, fully-dense 2Al·3CuO thermite nanocomposite powder was prepared by mechanical milling powders of Al and CuO in Ar atmosphere using hexane as a process control agent. The preparation details as well as chemical and morphological analyses for this nanocomposite powder can be found elsewhere [70]. All the samples were dried immediately after preparation for about 18 hrs in Ar atmosphere.

Recent detailed analyses of the ARM-prepared materials showed that only part of the oxide used is embedded in Al matrix and some separate oxide particles remain in the material. The effect is reduced for metal-rich materials, but may be substantial for the nominally stoichiometric compositions considered here. A previous XRD and Scanning Electron Microscopy (SEM) study of these materials [70] revealed some minor content of intermetallic phases as Cu_xAl_y, as well as Cu, Cu_2O, and Al_2O_3 which are most likely the products of thermite reactions occurring locally during milling. The amount of these components is small and is neglected in the present analysis, so that the sample is considered to contain only CuO and Al.

SEM images always show a small number of loose CuO particles, which were not embedded into the nanocomposite material. To quantify the amount of such particles and the final composition of the prepared nanocomposite material, cross-sectioned samples were studied using the energy-dispersive X-ray spectroscopy (EDS) of a field-emission scanning electron microscope (LEO 1530) equipped with an X-ray detector. For analysis, the sample was embedded in epoxy and cross-sectioned. Ten representative rectangular areas with the size 5×5 μm were randomly selected on the sample surface and atomic composition of Al and Cu in each area was measured with EDS. Assuming that the sources of Al and Cu elements in the sample are Al and CuO, i.e., neglecting minor contribution of other phases, the atomic composition can be directly related to the molar content of Al and CuO. By averaging the atomic composition of Al and CuO in all scanned areas, the average mole fractions of Al and CuO (normalized to the total Al-CuO molar content) were found be 0.47 and 0.53, respectively, with the standard deviation of 0.035. A relatively small standard deviation indicates that the components were well mixed on the μm scale. The deviation of the average mole content from that anticipated from the bulk composition of the starting Al and CuO mixture (0.40 and 0.60 for mole fractions of Al and CuO, correspondingly), confirms that not all CuO was embedded into the Al matrix. Therefore, the sample is an aluminum-rich 2.7Al-3CuO nanocomposite material including loose CuO particles, which do not contribute to the expected thermite reaction but affect the heat capacity of the material.

The heat release in a nanocomposite thermite was studied using a microcalorimeter TAM III by TA Instruments under isothermal conditions at different temperatures in the range from 303 to 413 K. The measurement at 303 K used a sample that was just prepared and dried for 18 hours. All other samples were stored at room temperature in Ar prior to the measurements. Table 6.1 gives samples ID's and summarizes their storage times and measurement temperatures.

Table 6.1 Aging/Storage Time and Conditions for Samples Used in TAM Experiments

Sample ID	Temperature, K	Time of storage in Ar prior to experiment
A	303	Used immediately after drying
B	323	2 days
C	323	1 day
D	403	5 days
E	413	2 days

Readily interpretable TAM III measurements are recorded after the sample thermally equilibrates in the furnace and when there is no heat flow disturbances inevitably generated when the sample is moved into the furnace. Figure 6.1 is an example of a typical initial portion of a TAM III trace. Vertical dashed lines schematically separate three stages in the measured signal: during the first stage, the sample was lowered into the temperature equilibration position where it was heated to the target temperature during ~15 min. The second stage indicates a signal disturbance when the sample was lowered further into the measurement position. According to the TAM III measurement protocol, the signal can be considered undisturbed only ~45 min after the sample is placed in its final position. During the first 60 min of the sample's exposure to the furnace temperature, the signal is affected by sample motion and related heat flow disturbances and thus is not readily useful. On the other hand, this is the time when the interfacial layers between the reacting components are just beginning to thicken, resulting in the highest reaction rates. The lack of a good measurement during this initial reaction period makes the data processing and interpretation somewhat difficult.

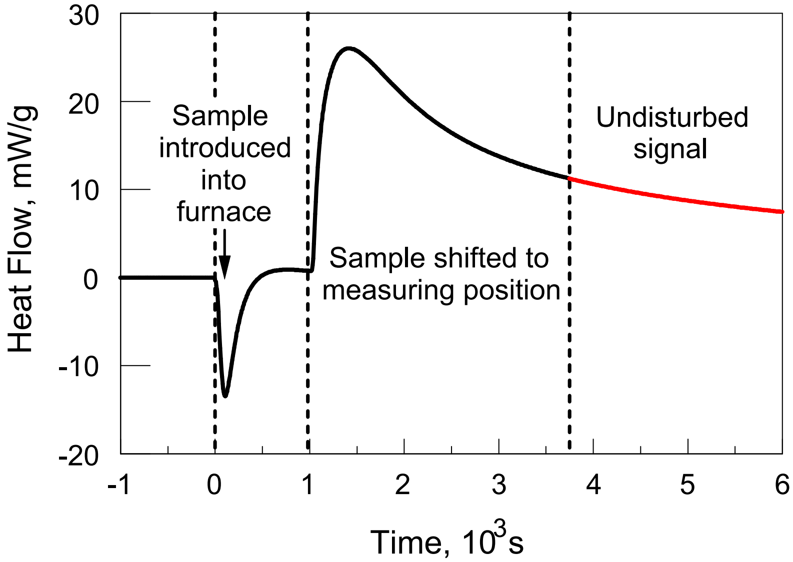

Figure 6.1 Example of a typical initial portion of the TAM trace (Sample E, 413K).

6.2.2 Experimental Results

The results of TAM III measurements are shown in Figure 6.2 in terms of both integral heat release and heat release rate, normalized by the sample mass. The traces are shown after the TAM III signal became free of heat flow disturbances. As expected, the reaction rates are substantially increasing with temperature. For a freshly prepared sample, even at a relatively low temperature of 303 K, a noticeable and quantifiable heat release is measured. Note that for samples stored for a year, a similar measurement did not show any reaction at 303 K (not presented in Figure 6.2). Reaction rates measured at the same temperature (323 K) were effectively identical for the samples C and B, stored prior to the experiments for one and two days, respectively. Note that samples C and B were from different powder batches, so that similarity of the respective TAM III traces suggests good reproducibility of both material preparation and the present experiments.

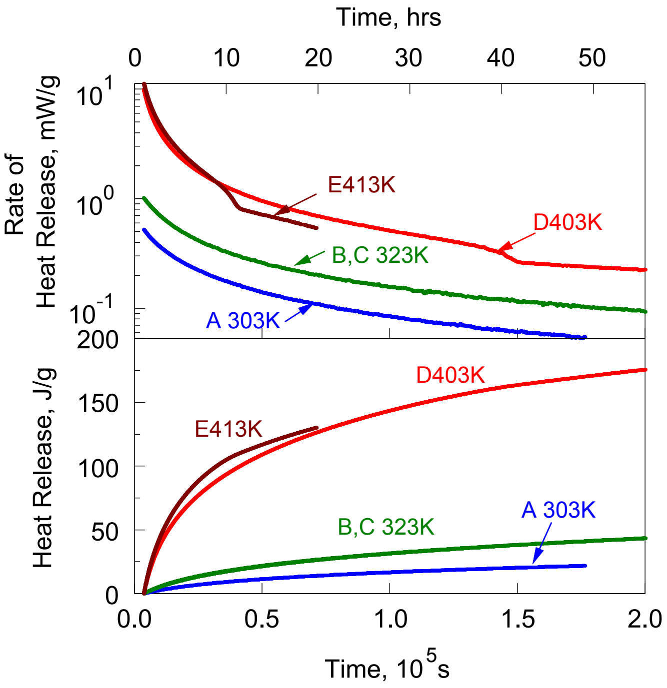

Figure 6.2 TAM III measurements of fully-dense nanocomposite Al·CuO powders: integral heat release and heat release rate, normalized by the sample mass, in the temperature interval 303 – 413 K.

Reaction rate traces measured at higher temperatures, 403 and 413K, exhibit additional features compared to traces acquired at lower temperatures. Each high-temperature trace can be divided into two stages with a relatively short transition period observed after about 10 and 40 hours for the samples reacting at 413 and 403 K, respectively. After the transition, the reaction rates decrease, suggesting a possible change in the mechanism of the thermite reaction. Most likely, this transition is associated with a change in the structure of the growing interfacial Al_2O_3 layer, e.g., from amorphous to γ-crystalline, occurring when the layer grows above some critical thickness, specific for each temperature. Because much thicker interfacial layers are growing at higher temperatures in TAM III experiments (see discussion below), it is not surprising that such transitions are not observed for low-temperature traces. Note that transitions could also be caused by oxygen depletion from the CuO inclusions resulting in changes in their phase make-up or reduced oxygen diffusion rates. Additional studies are needed to further explore the mechanisms of the observed transitions, which were outside the scope of the present paper focused on the initial stage of the Al-CuO reaction.

It was assumed that the initial parts of traces measured at 403 and 413 K are described by the same reaction mechanism as the measurements performed at 303 and 323 K. This reaction mechanism was also assumed to be active during early stages of the DSC experiments reported in ref [70]; the respective portions of the DSC signals are shown in Figure 6.3. For all heating rates, a relatively sharp increase in the reaction rate was observed to occur between 350 and 450 K. As the temperature increased, the reaction rates were observed to stabilize or even decrease at a higher heating rate.

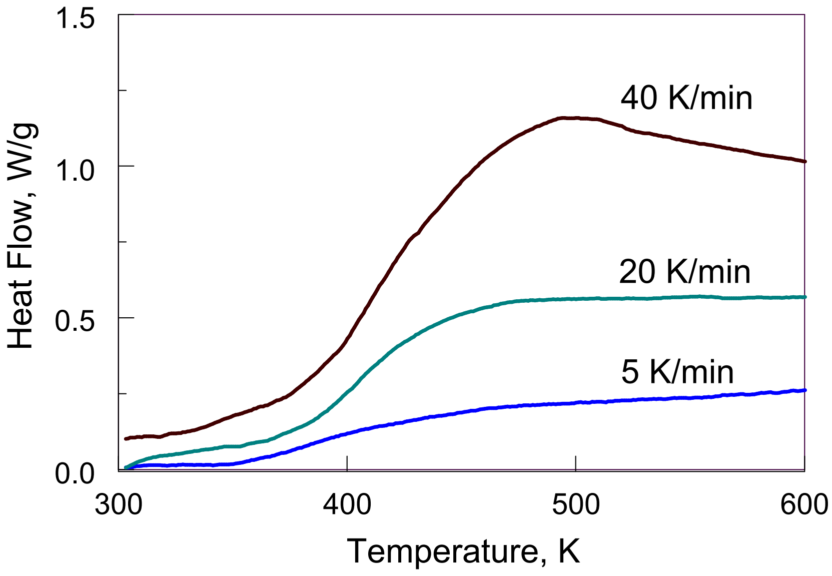

Figure 6.3 Low temperature portions of DSC traces for fully-dense 2Al·3CuO nanocomposite powders measured at different heating rates [33].

6.3 Model and Data Processing

6.3.1 Reaction Kinetics Model

To describe the heterogeneous reaction theoretically, the nanocomposite material was assumed to include mono-sized spherical CuO inclusions in Al matrix [57]. Based on analysis of the SEM images of particle cross-sections, inclusion diameters were taken as 100 nm. Reduction of CuO at relatively low temperatures often results in formation of metallic Cu, without formation of intermediate phases [76]:

$$3CuO + 2Al \rightarrow 3Cu + Al_2O_3 \tag{6.1}$$

Reaction 6.1 was considered in the model. While reaction 6.1 proceeded, the inclusion diameter was being corrected assuming that all Cu formed as a result of reaction 6.1 remained inside the inclusion. The CuO/Cu inclusion (core) was surrounded by a growing Al_2O_3 shell separating it from the Al matrix. Following ref. [57], the rate of reaction was described by the Cabrera-Mott model for the core-shell geometry of a spherical oxidizer inclusion in a fuel matrix [77]:

$$\frac{dr_2}{dt} = K \exp\left(\frac{E_2}{k_B T}\frac{r_1}{r_2 h}\right) \tag{6.2}$$

where k_B is the Boltzmann constant, T is temperature, r_1 and r_2 are the radii of the CuO core and Al_2O_3 shell, respectively, h is the thickness of Al_2O_3 shell: $h=r_2-r_1$, and K is described by an Arrhenius expression with the activation energy E_1 and preexponent k_0:

$$K = k_0 \exp(-E_1 / RT) \tag{6.3}$$

The relation between radii, r_1, and r_2, is defined by the spherical geometry and a parameter z, defined as the oxide volume formed per volume of the oxidizer consumed:

$$r_2^3 - r_1^3 - \left(r_{20}^3 - r_{10}^3\right) = z\left(r_1^3 - r_{10}^3\right) \tag{6.4}$$

where r_{10} and r_{20} are the initial core and external shell radii, respectively. The exponential term in Equation 6.2 represents a contribution from the electric field across the aluminum oxide film that essentially lowers the energetic barrier for the Al ions to traverse the layer towards aluminum oxide – copper oxide interface. The parameter E_2 of the Cabrera-Mott model reflecting the effect of Mott potential on the rate of mass transfer was suggested to increase with temperature [75]. As a first approximation, it was described here by a linear function:

$$E_2\left(T\right) = a + bT \tag{6.5}$$

where a and b are constants.

Four unknown kinetic parameters were used in the model in Equation 6.1-6.5 k_0, E_1, a, b. They were found from joint processing of the results of DSC and TAM III measurements as described below.

6.3.2 Data Processing

Both TAM III and DSC curves were interpreted to calculate changes in the radius of the CuO/Cu core, r_1, and thickness of the growing Al_2O_3 shell, h, implied by the measured heat flow. The measured gravimetric rates of heat release, $\dot{q}_{\exp}$, were first transferred into mass changes, m_i, for individual components in Equation 6.1

$$\dot{q}_{\exp} = \frac{1}{M} \sum_i \Delta H_i \dot{m}_i \tag{6.6}$$

where subscript i stands for Al, Al_2O_3, CuO and Cu; ΔH_i is the specific enthalpy of formation of a respective component at the experimental temperature [52], and M is the total mass of material. Once the mass changes for individual components were calculated, the values of r_1 and h were readily found considering the above introduced spherical core-shell geometry and component densities. For the time-dependent TAM III traces $\dot{q}_{\exp}(t)$, the temporal changes in the radii $r_1(t)$, $r_2(t)$, and thickness $h(t)$ were then inserted in the system of Equations 6.2-6.5 to find the best fit values for k_0, E_1, a, and b, describing these traces at different temperatures.

The main challenge for the meaningful data processing is that the initial thickness of the oxide shell $h_0 = r_{20} - r_{10}$ is not known at the instant when the undisturbed TAM III measurements began to be recorded (or when DSC measurements started). Its experimental assessment is difficult, in particular because the shell thickness existing before the sample is placed in the TAM III furnace is also unknown. Thus, h_0 was also treated as an adjustable parameter. Note that different values of h_0 were expected to characterize TAM III experiments performed at different temperatures and DSC runs, whereas values of k_0, E_1, a, and b, should be the same for all conditions.

To streamline identification of all adjustable parameters, the process was broken down into several steps. In the first step, each TAM III curve was processed individually. The initial alumina shell thickness, h_0, was systematically varied between 0.1 and 5 nm. For each value of h_0, parameters K and E_2 were treated as adjustable variables in Equation 6.2; the combination $\frac{r_1}{r_2 h}$ was treated as an independent variable, and the best fit between the experimental trace $\dot{q}_{\exp}(t)$ cast in terms of $\frac{dr_2}{dt}(t)$ and the calculated exponential function given by Equation 6.2 was found using a nonlinear least squares method. Note that K given by Equation 6.3 was treated as a temporarily introduced new variable parameter which was used later to determine k_0 and E_1. Thus, for each value of h_0, corresponding values of K and E_2 were found. For each of the found combinations of K, E_2 and h_0, the goodness of fit was evaluated using the root mean squared error, *RMSE*:

$$RMSE = \frac{\sum_{i=1}^{n} \sqrt{\left(\frac{dr_2}{dt}\right)_i - \left(\frac{d\hat{r}_2}{dt}\right)_i}}{n-2} \tag{6.7}$$

where $\left(\frac{dr_2}{dt}\right)_i$ and $\left(\frac{d\hat{r}_2}{dt}\right)_i$ are the instantaneous experimental and fitted values of the rate of growth of the external Al_2O_3 shell and n is the number of experimental points. Figure

6.4 shows the calculated *RMSE* vs. h_0 for different TAM III traces. For the traces measured at 303 and 323 K, there are clear minima indicating the best fits achieved for the particular selections of h_0. These minima can be interpreted to suggest that the corresponding h_0 values represent the experiment better than others. Therefore, respective values of K and E_2 could be considered as their final selections. However, no such minima were observed for the *RMSE* vs. h_0 curves for the traces measured at higher temperatures, 403 and 413 K. The lack of minima at higher temperatures can be understood considering that the reaction occurs to a much greater degree, resulting in significant deviations of the forming product morphology from the simplified assumed starting geometry. Some of the inclusions may be fully reduced; some inclusions may be located so close to each other that aluminum between them is consumed, etc. In addition, at higher temperatures, the thickness h_0 is expected to be greater, resulting in the reduced sensitivity of the reaction rate to its small changes. With such considerations in mind, it was suggested that the TAM III trace measured at the lowest temperature, 303 K, was best suited for selection of the values of $K = K(303) = 4.54\text{x}10^{-11}$ [nm/s] and $E_2 = E_2(303) = 1.70\text{x}10^{-20}$ [J-nm], based on the *RMSE* minimum shown in Figure 6.4.

Once the values of K and E_2 were found, the number of unknown parameters was reduced to two. Solving Equations 6.3 and 6.5 for k_0 and a, respectively, and substituting the results in Equation 6.2, one obtains the rate of change for the shell radius expressed using only two unknown parameters, b and E_1:

$$\frac{dr_2}{dt} = K(303)\exp\left(\frac{E_1}{303R}\frac{T-303}{T}\right)\exp\left(\left(\frac{E_2(303)}{k_B T} + b\frac{(T-303)}{T}\right)\frac{r_1}{r_2 h}\right) \qquad (6.8)$$

Equation 6.8 can be applied to process either TAM III (constant temperature) or DSC traces, for which a linear sample heating rate is defined. While not written out explicitly, the value of h_0 affects r_2 and h in Equation 6.8 and thus represents a third adjustable parameter, specific for each temperature for TAM III measurements; it should also be specified for the initial instant in the DSC measurements so that the entire trace can be interpreted.

In practical terms, for matching TAM III measurements, the values of h_0 varied systematically from 0.1 to 5 nm (as mentioned above); for each h_0, a combination of b and E_1 was found to achieve the best fit with the experimental trace. The resulting plots of b vs. E_1 (each point representing also a different selection of h_0) are shown in Figure 6.5. For DSC, the fitting was performed using the rising parts of the heat flow curves shown in Figure 6.3; specifically the least squares fit in the range of temperatures of 350-450 K was used to simultaneously fit all three DSC curves using a custom MATLAB code. Because parameters b and E_1 must be independent of the specific TAM III or DSC experimental conditions, all curves shown in Figure 6.5 were expected to cross in a single point identifying the invariant values for the parameters of interest. While this ideal situation was not observed, all curve intersections were relatively close to one another, identifying therefore a relatively narrow range of b and E_1 that should provide a reasonable description for all experiments. From Figure 6.5, it follows that $28<E_1<61$ [kJ-mol^{-1}] and $3.59\times10^{-22}<b<7.45\times10^{-22}$ [J-nm-K^{-1}] with the average values of $E_1=44$ kJ-mol^{-1} and $b=5.52$ J-nm-K^{-1}.

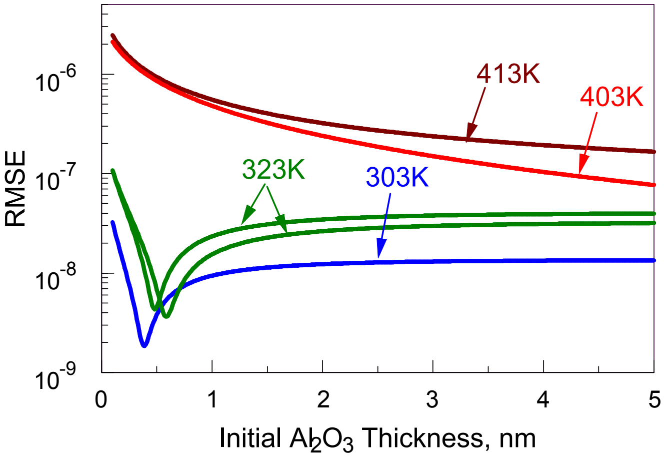

Figure 6.4 Root mean square error of fit as a function of aluminum oxide initial thickness.

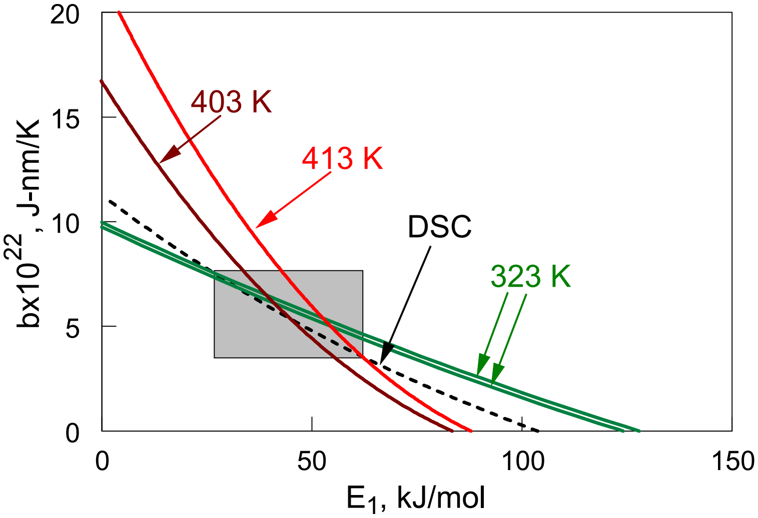

Figure 6.5 Parametric plots obtained by fitting DSC and TAM experimental curves.

6.4 Results

6.4.1 Reaction Kinetics

The final values of the kinetic constants, both average and their ranges, are shown in Table 6.2. Experimental TAM III data were reprocessed readjusting initial thickness of aluminum oxide to provide the best fit with the fixed average kinetic parameters shown in Table 6.2. The experimental and fitted TAM III traces cast in terms of grown thickness of the oxide layer and DSC traces in terms of both heat flow and thickness of the grown oxide are shown in Figures 6.6 and 6.7, respectively.

Table 6.2 Values of Kinetic Constants for their Ranges Obtained from Processing TAM III and DSC Measurements

	Average	Range	
k_0, nm/s	2.1×10^{-3}	2.5×10^{-6}	1.8
E_1, J/mol	44000	28000	61000
E_2, 10^{-22} J-nm	$-1502 + 5.52T$	$-2088 + 7.45T$	$-917+3.59T$

For TAM III traces shown in Figure 6.6, experimental and calculated results overlap very closely; to distinguish between the data sets, experimental curves are marked by symbols. It is also remarkable how good the correlation is between the calculated and measured DSC traces shown in Figure 6.7. It is interesting in particular that the calculated curves predict the observed increase in the heat flow followed by a relatively constant heat flow, as observed experimentally.

Note that each TAM III trace in Figure 6.6 begins at a specific initial thickness h_0; a common initial thickness was assigned for all DSC experiments performed with a similarly aged material stored at room temperature.

The values of h_0 were initially selected as described above, considering them as adjustable parameters specific for each experimental condition. Moreover, once the kinetic constants were identified, as shown in Table 6.2, the initial thickness for each TAM III experiment performed at a temperature above 303 K could also be estimated. The thickness of 0.38 nm identified for the experiments at 303 K was used as a starting point for all calculations. For each experiment, it was assumed that the sample reached the furnace temperature immediately after being inserted into the furnace, so that the respective reaction kinetics was used to describe its oxidation during the first hour of exposure to the pre-set temperature. The results of these estimates are shown in Table 6.3. The values of h_0 found as variable adjustable parameters are in good agreement with those calculated using the identified reaction kinetics mechanism, supporting its validity.

For samples used in DSC experiments, typically aged for several months prior to measurements, an estimate of the aging time was made using the initial oxide thickness and kinetic parameters found. Values for the initial thicknesses of aluminum oxide shell h_0 found as adjustable parameters from fitting the DSC curves vary in the range of 0.77 – 1.04 nm, according to the respective ranges of the identified kinetic parameters (Table 6.2). Because the freshly prepared samples were assumed to have the initial oxide thickness of 0.38 nm, the times required to age such samples at room temperature to grow 0.77 and 1.04 nm-thick oxide layers were calculated to be three months and a year, respectively.

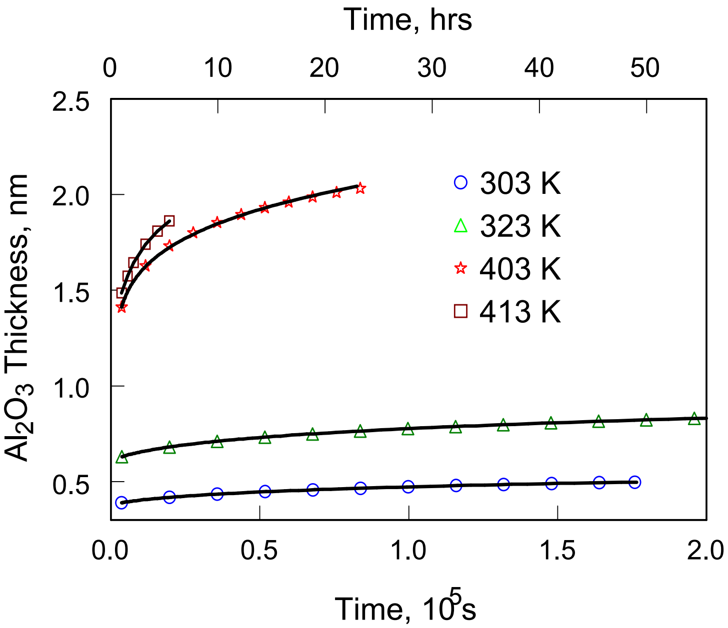

Figure 6.6 Comparison of the alumina oxide thickness inferred directly from TAM III measurements (symbols) and that predicted using the identified reaction kinetics (lines).

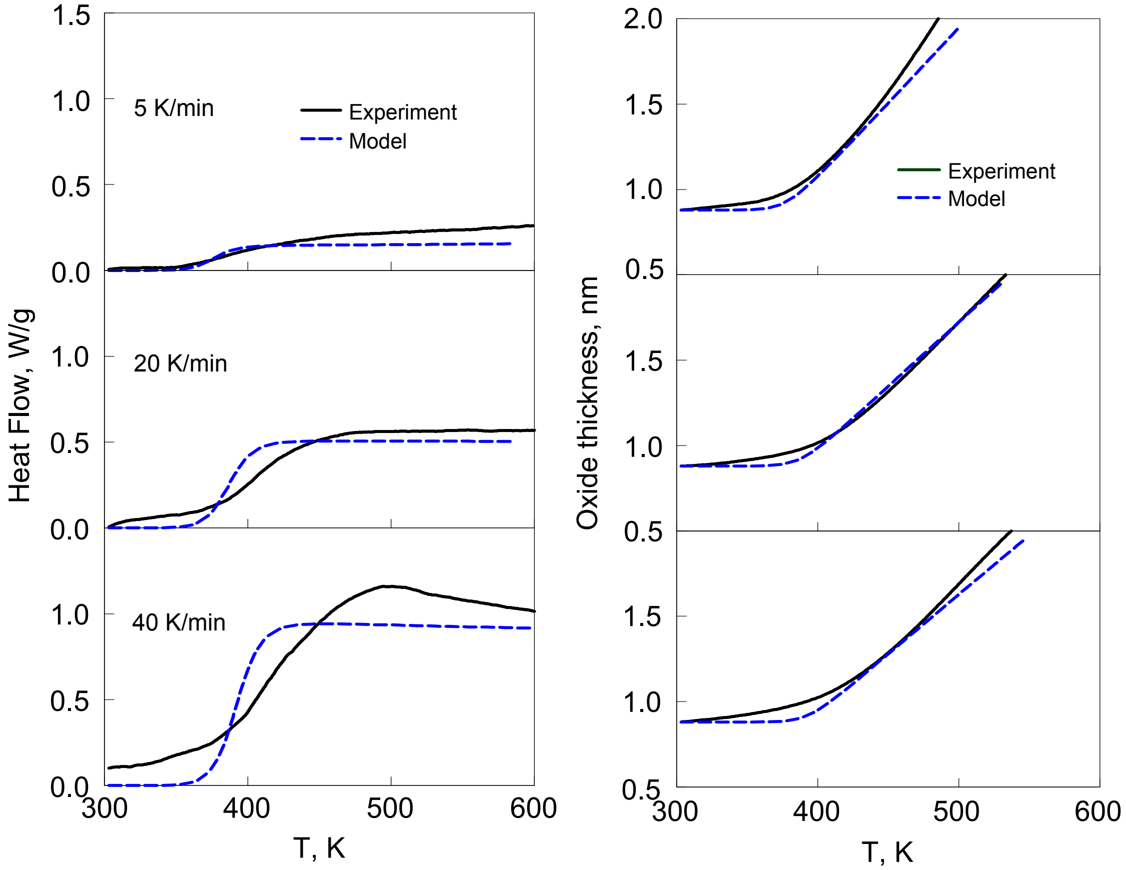

Figure 6.7 Experimental and theoretical DSC curves (on the left) and oxide thickness (on the right) at various heating rates: 5, 20 and 40 K/min (top to bottom). Initial thickness of Al_2O_3 at 303 K is 0.88 nm.

Table 6.3 Comparison of Initial Thicknesses as Obtained Directly from Fitting Procedure and from Calculations Based on Sample History

Sample ID	Temperature, K	Al_2O_3 thickness h_0,nm	
		from the fit	from the sample history
A	303	0.39	N/A
B	323	0.63	0.58
C	323	0.62	0.58
G	403	1.41	1.46
H	413	1.48	1.58

6.4.2 Sensitivity of the Model to Uncertainties of the Identified Parameters

Kinetic parameters were varied within ranges indicated in Table 6.2 and comparisons similar to those shown in Figures 6.6 and 6.7 were made. For TAM III, no significant discrepancies between the calculated and measured traces were observed for the entire range of kinetic parameters. For DSC, the experimental traces were bracketed by the curves calculated using ends of the specified uncertainty ranges.

In separate calculations, effect of the value of h_0 at 303 K was assessed. The value of h_0 was arbitrarily varied within ± 10% of the identified value of 0.39 nm. Results suggested that for a greater h_0, no reasonable ranges for E_1 and b could be established; in other words, parameters required to fit different TAM III experiments diverged substantially. Conversely, selecting a smaller thickness resulted in a set of kinetic parameters very similar to that shown in Table 6.2.

6.5 Conclusions

Simultaneous processing of the experimental data from DSC and microcalorimetry enabled us to determine the parameters for the Cabrera-Mott reaction kinetics describing redox reaction in the nanocomposite Al-CuO thermite prepared by arrested reactive milling. The parameters specified in Table 6.2 enable one to describe the initial portions of the DSC curves (up to 600 K) measured at different heating rates as well as microcalorimetry traces recorded in the temperature range of 303 – 413 K. Furthermore, introduced reaction kinetics enables one to predict how such materials are aging at room or elevated temperatures. This reaction kinetics is expected to be useful in describing initial stages of thermal initiation of such reactive materials subjected to heating, including conditions with high heating rates experienced in many practical systems. For a more complete description of thermal initiation and ignition, the current reaction mechanisms should be coupled to the reaction kinetics describing processes occurring at higher temperatures, such as thermally activated diffusion-limited oxidation, polymorphic phase changes in the growing oxide layers, and consumption of oxygen from the solid (or liquid) oxidizer.

CHAPTER 7

IGNITION OF ALUMINUM-COPPER OXIDE NANOCOMPOSITE POWDERS AT HIIGH HEATING RATES

7.1 Introduction

Reactive nanocomposite materials have been developed, which can achieve high reaction rates combined with high reaction enthalpies due to a very large reactive interface area. These materials have many potential applications in propellants, explosives, pyrotechnics, etc. Implementation of the new materials in specific applications would greatly benefit from a quantitative description for the kinetics of heterogeneous exothermic reactions leading to their ignition; it would be particularly important to validate these kinetic models for high heating rates occurring in practical systems.

This effort aimed to develop a validated kinetic model describing ignition in nanocomposite reactive powders includes both experimental and modeling parts. The nanocomposite materials used in this study are prepared by ARM and have compositions of 2Al·3CuO and 8Al·3CuO. DSC measurements were performed to complement earlier data [70] and enable identification of the reaction kinetics in a relatively broad temperature range. Ignition of the prepared powders is studied experimentally using both laser ignition [78, 79] and heated filament ignition [54] methods.

A reaction model is developed to interpret both ignition experiments. The initial reaction stages occurring at low temperatures are described using the reaction kinetics model considering Cabrera-Mott mechanism developed in the previous chapter [57]. The Cabrera-Mott kinetics is coupled with the model describing aluminum oxidation reaction controlled by the thermally activated mass transfer of reagents through an alumina film, which grows in thickness and experiences polymorphic phase changes [64, 65, 69].

Earlier work established parameters for such aluminum oxidation occurring in gaseous oxygen. In this work, the kinetic parameters describing phase changes between amorphous and γ-Al_2O_3 polymorphs and oxidative growth of these alumina phases are tuned to fit with the DSC measurements for the prepared nanocomposite powders. Note that formation of α-Al_2O_3 and its oxidative growth are not considered because these reactions typically occur at temperatures substantially higher than the experimental range of ignition temperatures for Al-CuO nanocomposite powders.

The reaction kinetics model with the adjusted reaction kinetic parameters is finally implemented into the numerical codes describing ignition of the nanocomposite powder on an electrically heated filament and ignition of individual nanocomposite particles crossing a CO_2 laser beam. Comparisons between calculated and experimental results are presented and discussed.

7.2 Materials

Following the previous chapter, the work focused on Al-CuO nanocomposite materials for which the phase contrast between fuel and oxidizer is well distinguishable in the images of their respective cross-sections [32, 70], and for which the low-temperature reaction mechanisms were developed. Reactive nanocomposites of compositions 2Al·3CuO and 8Al·3CuO used in this work were prepared by ARM as described in Chapter 6.

7.3 Experimental

Reaction behavior at low heating rates was evaluated by DSC. The same equipment and procedure were use as described in Chapter 5. Experiments were run under argon atmosphere at heating rates of 5, 20, and 40 K/min.

Ignition behavior was characterized using two techniques. The first technique used was the wire ignition experiment as described in Chapter 5. Heating rates used with this experiment were in the range of 10^3 to 10^4 K/s.

In order to achieve ignition at very high heating rates, on the order of 10^6 K/s, particles were ignited by a laser beam. As shown in Figure 7.1, individual nanocomposite particles are fed by a vibratory feeder into a gas stream. The gas stream carries the particles through a laser beam which heats the particles up to ignition. The laser power was adjusted in order to find the minimum power at which the particles would ignite [78].

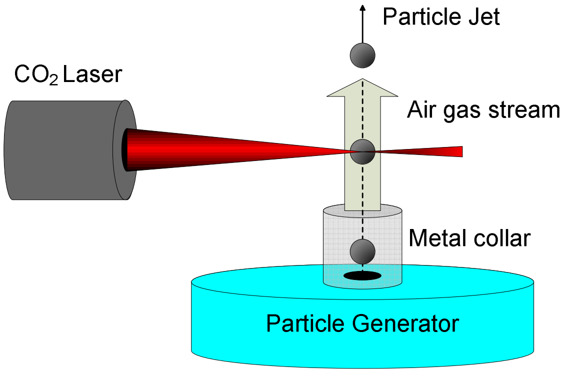

Figure 7.1 Schematic describing the ignition of a single particle by a CO_2 laser beam.

7.4 Numerical Modeling

7.4.1 Reaction Kinetics Model

7.4.1.1 General Description. The reaction kinetics model considers the nanocomposite material as having uniformly sized, spherical CuO inclusions embedded into the Al matrix as described in Chapter 6. Based on SEM images of powder cross-sections, the CuO inclusion diameter is assumed to be 100 nm. Each inclusion is assumed to be surrounded by an initial, very thin amorphous aluminum oxide layer, h_0. This initial oxide layer in the model simulates a poorly characterized interface existing between Al and CuO in the actual materials and preventing the redox reaction from occurring at low temperatures. The thickness of this layer can be assessed using the Cabrera-Mott reaction kinetics identified in the previous chapter and knowing the time the material was stored prior to experiments.

As the reaction progresses, the amorphous aluminum oxide film thickens and eventually transforms to γ-Al_2O_3. Figure 7.2 shows the geometry of the core and shells at different stages during a reaction. Figure 7.2A is the initial configuration consisting of the CuO core surrounded by a thin initial layer of amorphous alumina. As the reaction proceeds, the layer grows while the core shrinks. Eventually, the amorphous layer starts to transform into the γ polymorph. The transformation is set to begin at the outer radius of the amorphous shell; it propagates radially inwards as shown in Figure 7.2B. After all the amorphous alumina is consumed, the remaining γ oxide continues to grow by oxidation due to consumption of the CuO core, as represented in Figure 2C.

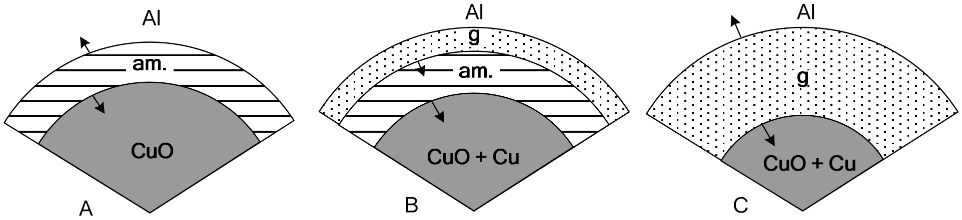

Figure 7.2 Configurations of CuO core and Al_2O_3 shells in different states of reaction progress.

The specific geometry shown in Figure 7.2 implies that the oxidative growth of the amorphous oxide film is rate limited by diffusion of Al ions towards the oxidizer, so that the reaction occurs at the Al_2O_3/CuO interface.

Several mechanisms are used to describe the reaction. The initial growth of the amorphous alumina is described using the Cabrera-Mott mechanism following the previous chapter. Note that before the transformation of the amorphous oxide into γ polymorph, the thickness of the amorphous oxide layer is typically increased, so that the rate of reaction governed by the Cabrera-Mott kinetics decreases. However, during the first polymorphic phase transformation (amorphous oxide $\rightarrow \gamma$), the thickness of the amorphous oxide is decreasing and the rate of reaction governed by the Cabrera-Mott kinetics increases, which additionally accelerates the predicted reaction rate.

Thermally activated growth of the amorphous oxide controlled by Arrhenius type kinetics becomes important at a higher temperature, when the Cabrera-Mott mechanism becomes less significant because of an increased oxide film thickness. A phase change from amorphous to γ-Al_2O_3 and Arrhenius-controlled oxidative growth of γ-Al_2O_3 are further introduced following refs [64, 65, 69].

While more than one alumina polymorphs can exist at the same time, as in earlier work, in the model only one of the polymorphs is allowed to grow due to oxidation at any given moment. The oxide phase allowed to grow has the greatest diffusion resistance.

Note that growth of an oxide polymorph as a result of phase change, e.g., amorphous to γ-Al_2O_3 can occur simultaneously with the oxidative growth. As in Chapter 6, the redox reaction $2Al + 3CuO \rightarrow Al_2O_3 + 3Cu$ is assumed.

The reaction kinetics model is discretized in the time domain. Starting with the initial conditions, the equations are solved for the future time step, *i+1*, iteratively.

7.4.1.2 Cabrera-Mott Mechanism.

The initial growth of amorphous oxide is described by the Cabrera-Mott (CM) mechanism as developed in Chapter 6. The equations used to describe the growth are given below.

Equation 7.1 describes the rate of growth of the amorphous layer radius (77). The parameters k_0 and E_1 represent the preexponent and activation energy.

$$\frac{dr_{am}^{CM}}{dt} = k_0 \cdot \exp\left[-\frac{E_1}{T} + \frac{E_2 \cdot r_{core}}{T \cdot r_{am} \cdot h_{am}} \right] \tag{7.1}$$

The contribution of the electric field (Mott potential) across the oxide layer towards the Al ion transport is given by E_2. The effect of electric field depends on the thickness of the oxide layer h_{am} as well as on the core and shell radii r_{core} and r_{am}, respectively. Equations 7.2 and 7.3, shown in discretized form, describe the amorphous shell and the core radii based on the CM growth.

$$r_{am}^{i+1,*} = r_{am}^{i} + \frac{dr_{am}^{CM}}{dt} \Delta t \tag{7.2}$$

$$r_{core}^{i+1,*} = r_{core}^{i} - \left[\frac{{r_{am}^{i}}^{2}}{{r_{core}^{i}}^{2}(z+1)} \frac{dr_{am}^{CM}}{dt} \Delta t \right] \tag{7.3}$$

$$r_{am}^3 - r_{core}^3 - \left(r_{am,0}^3 - r_{core,0}^3\right) = z\left(r_{core}^3 - r_{am,0}^3\right) \qquad (7.3a)$$

Equation 7.3 is the derivative of Equation 7.3a, which gives the relation between radii of the inclusion r_{core} and external radius of the aluminum oxide shell r_{am}. The relation is defined by the spherical geometry and the ratio z of the oxide shell volume formed per diffusing oxygen ion over the volume of the oxidizer core vacated when the oxygen ion is released. Using Equation 7.4, the instantaneous mass growth rate of the amorphous oxidation by CM mechanism is found based on changes in the core and shell radii.

$$\frac{dm_{am}^{CM}}{dt} = \frac{4\pi\rho_{am}}{3\Delta t}\left({r_{am}^{i+1,*}}^3 - {r_{core}^{i+1,*}}^3 - {r_{am}^{i}}^3 + {r_{core}^{i}}^3\right) \qquad (7.4)$$

7.4.1.2.1 Thermal Diffusion Mechanism. Equation 7.5 describes the mass growth rate of the amorphous oxide formed by thermal diffusion. The preexponent C_{am} and activation energy E_{am} are based on values found in earlier work (65).

$$\frac{dm_{am}^{Diff}}{dt} = f_{am}(\alpha_{am})C_{am}\exp\left(-E_{am}/RT\right)\left(1/r_{core}^{i} + 1/r_{am}^{i}\right)^{-1} \qquad (7.5)$$

The reaction progress for the oxidative growth of the amorphous oxide, α_{am}, is introduced. The value of α_{am} is defined based on the global reaction progress, α. The global progress α is given by Equation 7.6a and is based on the consumption of the CuO. The initial value of α is zero and it converts to 1 upon the complete consumption. The progress for the oxidative growth of the amorphous oxide, α_{am}, is defined in Equation 7.6b, where c_{am} is an adjustable coefficient.

$$\alpha = \frac{\Delta m_{CuO}^{cum}}{m_{CuO}^{ini}} \tag{7.6a}$$

$$\alpha_{am} = c_{am}\alpha \tag{7.6b}$$

Amorphous alumina stops forming well before the entire CuO inclusion is reduced to Cu; thus coefficient c_{am} should be greater than 1 to enable reaching α_{am} =1 when this reaction stage is completed.

Note that the Arrhenius factor in Equation 7.5 is multiplied by a complex reaction model given by $f_{am}(\alpha_{am})\left(1/r_{core}^{i} + 1/r_{am}^{i}\right)^{-1}$. The expression in the second parentheses shows the geometric effect of the shrinking spherical CuO core. The function $f_{am}(\alpha_{am})$ depends on the concentration of oxygen in CuO, decreasing as the reaction is progressing. No such function was used in the previous work [65, 69] considering aluminum oxidation in gaseous oxidizers.

The progress function $f_{am}(\alpha_{am})$ is given by Equation 7.6c corresponding to an Avrami-Erofeev mechanism A2 according to ref. [80]. That equation was selected among different reaction models described in the literature [80] based on the best match of the calculated results with the experiments.

$$f_{am}(\alpha_{am}) = 2(1-\alpha_{am})(-\ln(1-\alpha_{am}))^{1/2} \tag{7.6c}$$

The total mass of alumina formed due to oxidative growth of the amorphous oxide is given as a sum of contributions from both Cabrera-Mott and diffusion reaction mechanisms:

$$\Delta m_{am}^{tot} = \frac{dm_{am}^{CM}}{dt}\Delta t + \frac{dm_{am}^{Diff}}{dt}\Delta t \tag{7.7}$$

7.4.1.3 Growth of Gamma Alumina. The amorphous layer will eventually begin transforming into the γ-A_2O_3 polymorph. The transformation velocity is given by Equation 8 [69]:

$$v_{am\rightarrow\gamma} = F_{am\rightarrow\gamma} T \left[1 - \exp\left(\frac{-K_{am\rightarrow\gamma} h_{am}}{RT} \right) \right] \exp\left(\frac{-E_{am\rightarrow\gamma}}{RT} \right) \tag{7.8}$$

It describes the rate at which the transformation front radially propagates through the alumina layer. Gamma alumina forms at the outer radius of the amorphous alumina layer and moves inwards. The velocity is dependent on both temperature and the thickness of the amorphous layer. The parameters $F_{am\rightarrow\gamma}$ and $K_{am\rightarrow\gamma}$ and $E_{am\rightarrow\gamma}$ are specified in the previous work [65]. The corresponding mass transformation rate is given by Equation 7.9.

$$\frac{dm^{tr}_{am\rightarrow\gamma}}{dt} = 4\pi\rho_{am} r^2_{am} v_{am\rightarrow\gamma} \tag{7.9}$$

During the transformation, either amorphous or gamma alumina, but not both, is permitted to continue growing by oxidation. Oxidative growth of the gamma oxide begins when its diffusion resistance exceeds that of the shrinking layer of the amorphous oxide. Note that following ref. [69], the initial diffusion resistance of gamma alumina is considered to be very small, because the oxide coverage consists of separate individual crystallites growing out of the amorphous oxide. As the thickness of the gamma alumina layer increases, it forms a continuous polycrystalline oxide shell, so that its diffusion resistance can be calculated using bulk properties of the gamma-alumina. The minimum gamma oxide thickness, h_γ^{min}, required for the formation of a continuous polycrystalline layer was also specified in ref. [64]. The mass growth rate of gamma oxide is given by Equation 7.10.

$$\frac{dm_{\gamma}^{ox}}{dt} = f_{\gamma}(\alpha_{\gamma})C_{\gamma}\exp\left(-E_{\gamma}/RT\right)\left(1/(r_{core}+h_{am})-1/r_{\gamma}\right)^{-1} \tag{7.10}$$

Similarly to Equation 7.5, Equation 7.10 also contains a specific progress function describing reaction progress for the oxidative growth of gamma alumina. It is given by Equation 7.11a.

$$\alpha_{\gamma} = c_{\gamma}(\alpha - \alpha^{*}) \tag{7.11a}$$

Where α^* is the global reaction progress at the moment when the gamma oxidation starts and c_γ is an adjustable coefficient. Similar to c_{am}, the value of $c_\gamma>1$ in order to enable achieving $\alpha_\gamma=1$ before the entire CuO reduction is completed.

The reaction progress function in this case is described by an expression for a first order reaction in Equation 7.11b.

$$f_{\gamma}(\alpha_{\gamma}) = 1 - \alpha_{\gamma} \tag{7.11b}$$

As for the growth of amorphous alumina, this model is also selected to enable best fit with the experimental DSC data.

The heat produced per mass of alumina formed is finally given by Equation 7.12. The parameter χ is the number of inclusions per unit of mass in the nanocomposite particle. The enthalpy of formation of Al_2O_3, $\Delta H_{Al_2O_3}$ is based on the stoichiometric redox reaction and is a function of temperature calculated based on the temperature-dependent formation enthalpies of the reacting species and products [52].

$$Q_{chem} = \chi \Delta m_{Al_2O_3} \Delta H_{Al_2O_3} \tag{7.12}$$

7.4.2 Selection of the Model Parameters Based on DSC Measurements

The Cabrera-Mott model parameters found in Chapter 6 were used. The model parameters for the diffusion-controlled reactions were taken from previous work [65] and adjusted as necessary based on the experimental DSC results. It was expected that the reaction kinetics parameters should be adjusted. Indeed, the previous work considered growth of alumina scales in gaseous oxidizers, and the presence of CuO and its respective reduction products in the immediate vicinity of the growing alumina were expected to alter the reaction kinetics. The model parameters used in this work and adjusted compared to those reported earlier are shown in Table 7.1. In addition, Table 7.1 shows two parameters introduced in the present model and describing reaction progress functions for growth of amorphous and γ-alumina layers. Model parameters taken directly from earlier work and used in these calculations are given in Table 7.2.

To model a DSC experiment, the total heat flow is taken as the sum of each reaction process over the temperature range at a specified heating rate. Figure 7.3 illustrates adjustment of the activation energies E_{am} and E_{γ} used in Equations 7.5 and 7.10, respectively. An experimental DSC trace measured at the heating rate of 5 K/min is shown together with the DSC traces predicted using the initial and adjusted values of the activation energies. The experimental trace shows an initial broad exothermic hump followed by two major peaks at about 685 and 885 K. The initial broad feature is well described by the Cabrera-Mott kinetics. The two exothermic peaks are correlating with the oxidative growth processes of amorphous and gamma alumina films, described by Equations 7.5 and 7.10, respectively. An additional sharp spike observed between two exothermic peaks in the calculated DSC traces occurs when diffusion resistance of the growing γ-alumina layer becomes greater than that of the shrinking layer of amorphous alumina, so that a switch in the reaction rate limiting process occurs. The specific instant when this spike is observed is affected most significantly by selection of $h_\gamma^{\min}$. This effect predicted by the model is superficial; it results from a simplifying assumption allowing direct oxidative growth for only one alumina polymorph at a time. It was observed that it was not playing an important role in the processes occurring at high heating rates, when the oxide thickness is always substantially lower than $h_\gamma^{\min}$. Thus, removal of this superficial spike by fine tuning of $h_\gamma^{\min}$ and other model parameters was not attempted.

Positions of the exothermic peaks predicted using initial activation energy values for E_{am} and E_γ are shifted compared to the experimental DSC trace. These positions were adjusted by relatively small changes in the activation energies, as shown in Figure 7.3. Note that a similar adjustment could be achieved by correcting the pre-exponential factors in Equations 7.5 and 7.10. Alternately, a better match of the peak positions observed at different heating rates was obtained by adjusting the activation energies.

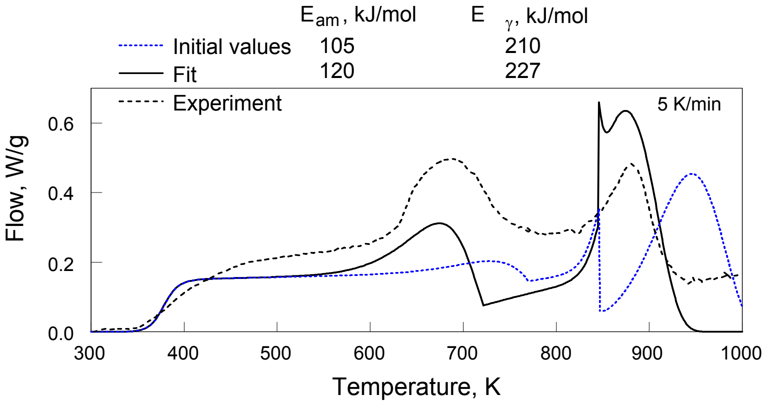

Figure 7.3 DSC curves calculated using initial activation energies from ref. [65] and fitted values compared to experimental curve at 5 K/min.

The adjustment of the peak amplitudes without significantly affecting their positions was achieved by selecting appropriate values of c_{am} and c_γ shown in Table 7.1.

Sensitivity of the model to changes in the parameters $E_{am\rightarrow\gamma}$, $K_{am\rightarrow\gamma}$, and $F_{am\rightarrow\gamma}$, was tested in a set of calculations; ultimately, all these parameters were left unchanged since they did not significantly improve the match between the calculated and measured DSC curves.

Table 7.1 List of Model Parameters Used in the Reaction Kinetics Model with their Initial and Final Adjusted Values After Fitting to Experiment

Parameter	Description	Initial Value	Final Value
E_{am}	*Activation energy for diffusion-limited growth of amorphous oxide*	*120 kJ/mol*	*105 kJ/mol*
E_γ	*Activation energy for diffusion-limited growth of gamma oxide*	*227 kJ/mol*	*210 kJ/mol*
c_{am}	*Coefficient for reaction progress for growth of amorphous* Al_2O_3	-	*5*
c_γ	*Coefficient for reaction progress for growth of* γ–Al_2O_3	-	*8*

Initial values are found in ref. [65].

Table 7.2 List of Unadjusted Parameters and their Values

Parameter	Description	Value
b	*coefficient used in linear function of* E_2	*40*
E_1	*activation energy used in Cabrera-Mott equation*	*5351 K*
h_0	*Initial thickness of amorphous oxide layer*	*0.90 nm*
C_{am}	*Preexponent for amorphous oxidation by diffusion*	$5.098x10^{-8}$ *kg/m-s*
C_γ	*Preexponent of gamma oxidation by diffusion*	$4.0784x10^{-3}$ *kg/m-s*
$E_{am \rightarrow \gamma}$	*Activation energy for amorphous to gamma transformation*	*458 kJ/mol*
$K_{am \rightarrow \gamma}$	*Exponential coefficient in gamma transformation equation*	$1x10^{12}$ *J/mol-m*
$F_{am \rightarrow \gamma}$	*Preexponent for transformation equation*	$2x10^{-15}$ *m/s-K*
h_γ^{min}	*Minimum thickness of gamma layer in order to contribute to real diffusion resistance*	*3.47 nm*

Figure 7.4 is shown to clarify contributions of different processes considered in the reaction model to the shape of the calculated DSC curve. The heat flow corresponding to a DSC experiment at a heating rate of 5 K/min is shown together with mass growth rates and thicknesses for both amorphous and γ-alumina layers. In addition, changes in mass growth rate and thicknesses of amorphous and γ-alumina layers as a result of their direct oxidative growth (either by Cabrera-Mott or diffusion-controlled reaction) and polymorphic phase changes are shown separately.

Comparing different parts of Figure 7.4, it becomes clear that the initial oxidation is controlled by the Cabrera-Mott mechanism; that reaction begins to slow down as the amorphous layer becomes thicker. The mass rates in the temperature range between 500 and 800 K are expanded in the inset to show clearly how the Cabrera-Mott reaction becomes overtaken by growth of the amorphous oxide layer as a result of regular, thermally activated diffusion. It is interesting that when temperatures exceed ca. 710 K, the rate of mass increase of amorphous oxide due to diffusion decreases and the Cabrera-Mott reaction accelerates. This predicted effect is due to the beginning transformation of amorphous to γ-alumina, resulting in the reduction in the amorphous oxide thickness. The reduced oxide thickness accelerates reaction rate calculated using Equation 7.1. At higher temperatures, the γ-Al_2O_3 layer begins forming as a result of a polymorphic amorphous-γ-Al_2O_3 phase change. When it just appears, its diffusion resistance is negligible so that oxidation continues to be controlled by the diffusion through the remaining layer of amorphous alumina. When the thickness of γ-Al_2O_3 exceeds h_γ^{min} (at about 850 K) its diffusion resistance increases sharply to match that of a regular polycrystalline γ-Al_2O_3 [73]. At this point, diffusion through the γ-Al_2O_3 becomes the rate-controlling step of reaction.

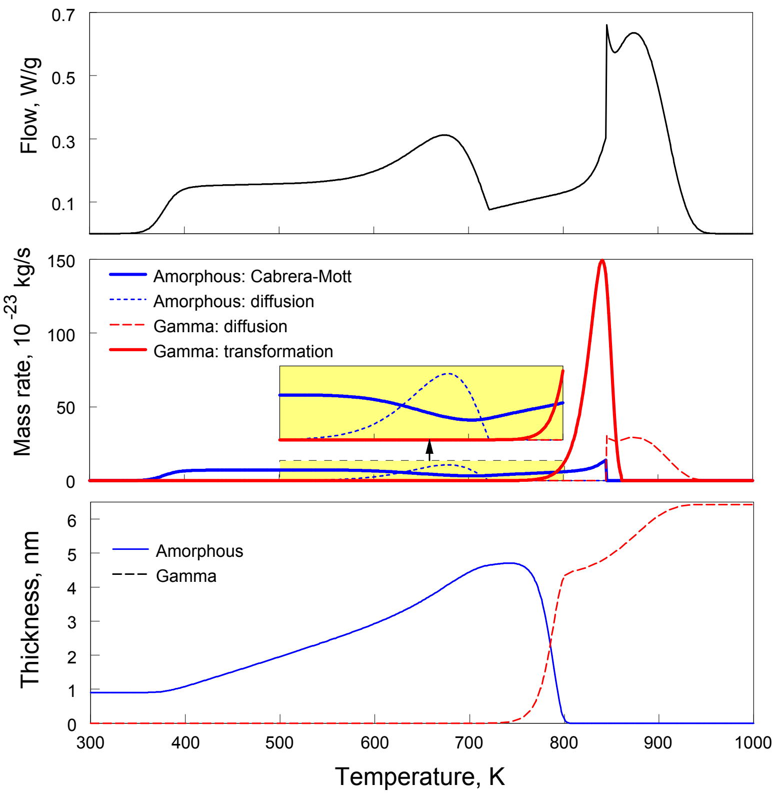

Figure 7.4 Calculated heat flow (top), rates of mass change for different alumina polymorphs (middle), and radii of individual alumina polymorph layers (bottom) at 5 K/min for DSC experiments.

The final result obtained in fitting the model to the DSC traces measured at different heating rates is shown in Figure 7.5. The model describes the main features of the DSC curves fairly well. Peak shapes, their positions, and relative heat effects are captured, which is expected to be important when the model is applied to explore ignition phenomena in these materials. There is a discrepancy between predicted and measured initial slopes of the DSC traces. These discrepancies are likely explained by the use of a single, uniform inclusion size for calculations. The match can be substantially improved by using a realistic size distribution for the oxide inclusions. In experiments, several small features are observed between the amorphous and gamma oxidation peaks, which are not represented in the model. These features are associated with the formation of intermetallic compounds [70], these effects are minor and were not incorporated into the current model.

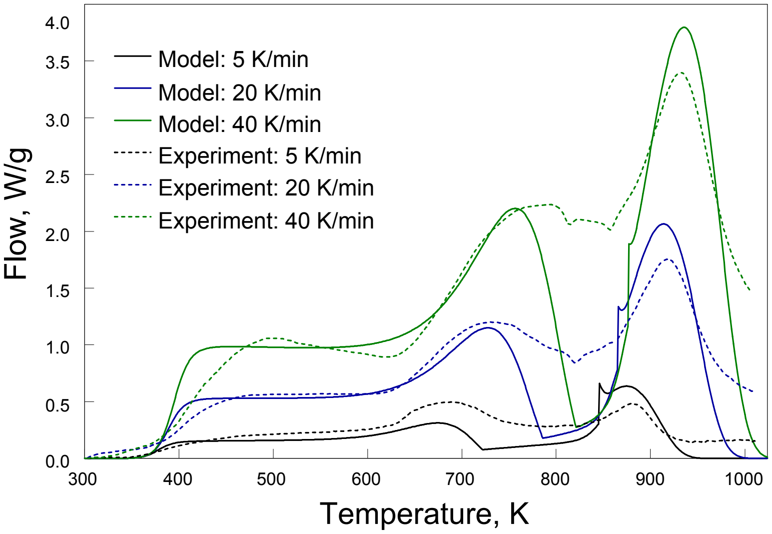

Figure 7.5 Experimental and calculated DSC curves for 2Al·3CuO at heating rates of 5, 20, and 40 K/min.

Extrapolating to a higher heating rate, the model gives the results shown in Figure 7.6. Qualitatively, the behavior is similar to that observed in Figure 7.3, with all thermally activated processes shifted to higher temperatures. The predicted acceleration in the Cabrera-Mott reaction rate that accompanies beginning of the amorphous to γ-alumina transformation precedes the diffusion peak describing oxidative growth of amorphous oxide.

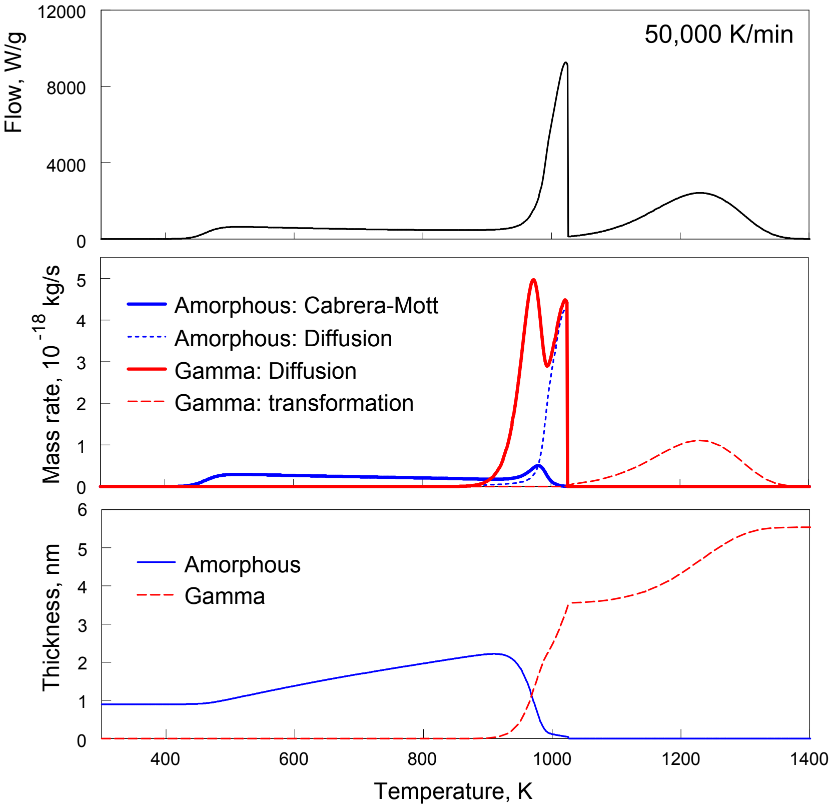

Figure 7.6 Calculated heat flow (top), rates of mass change for different alumina polymorphs (middle), and radii of individual alumina polymorph layers for DSC experiments at 50,000 K/min (bottom).

7.4.3 Heated Filament Ignition Model

The filament ignition model is the same as used previously in Chapter 4. The only modification made is that the chemical heat generation is calculated using the reaction model developed here. The model uses the thermal diffusivity of Al-CuO nanocomposite powders, which is not known. It is also difficult to measure using the flash method [51] because the powder is readily ignited by the applied heat pulse. Therefore, the value for thermal diffusivity measured for $8Al{\cdot}MoO_3$ powder, $8{\cdot}10^{-6}$ m^2/s, was adapted here. The model also assumes a uniform spherical particle size which is a substantial simplification. Although, it was found that the predicted powder temperature histories for the present experimental conditions are not very sensitive to both the thermal diffusivity and assumed particle size.

7.4.4 Particle Laser Ignition Model

The laser ignition numerical model is based upon the model developed in [78, 79]. The model considers a particle traveling at a specific velocity, about 0.36 m/s, through a laser beam. As the particle crosses the laser beam, it is heated due to absorption of the laser energy. Heat losses by convection and radiation are accounted for. Chemical heat generation is described by the present reaction kinetics model. It was shown previously [78] that the particle size affects substantially the efficiency of the CO_2 laser light absorption; particles with diameters 3.37 μm are heated most effectively. Therefore, following the previous work [78], it is assumed here that the particles ignited at the lowest laser energy have this specific diameter. Note that the aluminum particle absorption factor varies in the range of 0.08-0.15 for the range of particle temperatures achieved in the laser beam. This absorption factor is likely to be much greater for the nanocomposite powders including copper oxide inclusions; the absorption coefficient for CuO was reported to vary in the range of 0.52-0.58 [81]. In calculations, it was assumed that the maximum absorption factor for the particles is an average between those for pure Al and for CuO, i.e., 0.34. In other words, the particle-size dependent absorption efficiency was multiplied by a factor of 2.2, so that its temperature dependent values varied from 0.18 to 0.34.

7.5 Results and Discussion

7.5.1 Filament Ignition

Figure 7.7 shows the measured ignition temperature as a function of heating rate for the 2Al·3CuO and 8Al·3CuO materials. These are temperatures of the heated filaments taken at the instants the powders were observed to ignite. The stoichiometric composition appears to have a trend of increasing ignition temperature with increasing heating rate. The data is within the range found in previous work for a similarly prepared material [70]. The fuel-rich composition seems to have a fairly constant ignition temperature over the range of heating rates. Its measured ignition temperatures are somewhat higher than those reported previously for a similarly prepared material [32].

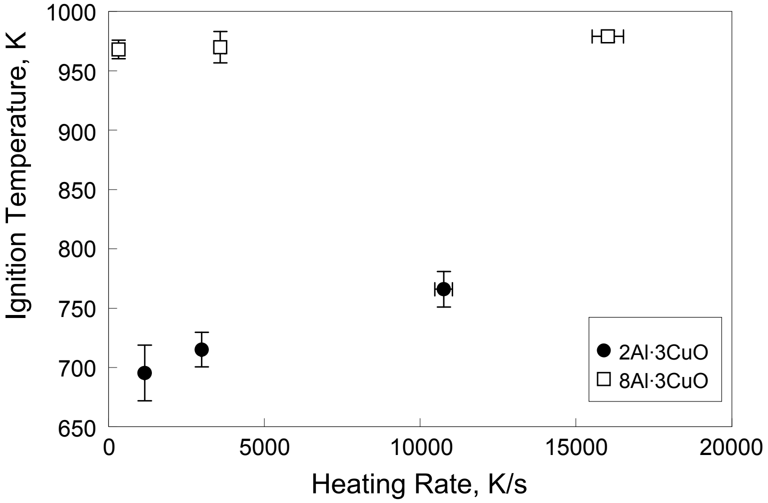

Figure 7.7 Experimental data showing ignition temperature as a function of heating rate for the 2Al·3CuO and 8Al·3CuO nanocomposite powders.

Using the numerical model, temperature histories are calculated for the powder layers as well as for the heated filament. Generally, powder temperature follows closely that of the heated filament. Figure 7.8 shows the temperature histories for different powder layers of 2Al·3CuO coating heated at the heating rates of 10^3 and 10^4 K/s. The temperature histories are shown as the differences between the powder layer temperature and the filament temperature directly underneath the powder layer as a function of the filament temperature at the pyrometer location (referred to as pyrometer temperature). The pyrometer temperature can be directly compared to the experimental data. Also shown, are the alumina mass growth rates for individual processes corresponding to the first powder layer at the heating rate of 10^3 K/s.

Exothermic processes occurring in the powder result in its temperature approaching, or sometime even exceeding the filament temperature. The overall shapes of the temperature difference curves shown in Figure 7.8 are reminiscent of the DSC traces presented earlier. A closer look at the calculation results suggests that the first exothermic process, with a peak around 570 and 620 K for the low and high heating rates, respectively, is associated with the Cabrera-Mott reaction. The sharp second peak occurring at about 1050 K for the low heating rate (10^3 K/s) is a combined effect of the accelerated Cabrera-Mott reaction and rapid growth of amorphous alumina. The oscillatory temperatures observed before that peak are due to the powder layers entering the aluminum melting phase one at a time. For the high heating rate case (10^4 K/s), the amorphous alumina appears after aluminum began melting, so that the temperature spike observed for the lower heating rate disappears despite acceleration in the rate of exothermic reaction accompanying the polymorphic phase change in alumina. Instead, the rapidly released chemical heat results in an accelerated rate of aluminum melting.

It is interesting that the pyrometer temperatures at which these two exothermic events are observed are relatively well correlated with the experimental ignition temperatures for the stoichiometric and Al-rich powders, as shown in Figure 7.7. The third peak observed in Figure 7.8 occurs near 1400 K. It corresponds to the diffusion-limited growth of γ-Al_2O_3. This process is of little importance to ignition because it occurs at much higher temperatures than the experimentally detected ignition events.

It is clear that heterogeneous exothermic processes considered in the model never directly predict the temperature runaway expected for ignition. However, the powder temperatures were observed to increase and, in some instances, exceed the filament temperature, when the respective pyrometer temperature was very close to that measured at ignition. Therefore, the present results should be interpreted to describe a process triggering ignition rather than ignition itself. The missing exothermic processes are most likely associated with the release of gaseous oxygen by decomposing CuO [56, 82] and subsequent reactions of that additional gaseous oxygen with aluminum. It is hypothesized here that such oxygen release is triggered by an accelerated heterogeneous Al-CuO reaction, as described by the proposed mechanism. Indeed, decomposition of CuO is known to be substantially affected by environment. For example, it occurs following different pathways in hydrogen [76], in presence of Al_2O_3 or doped Al_2O_3 [83], or in nitrogen [84]. In this particular case, it can be suggested that while the CuO inclusions are surrounded by an effectively inert matrix (Al_2O_3 at low temperatures), the oxygen ions are accumulated at the Al_2O_3/CuO interface preventing further CuO decomposition. When diffusion resistance of the Al_2O_3 layer diminishes, oxygen is being removed rapidly from the region close to the Al_2O_3/CuO interface.

Therefore, the structure of the CuO core close to the Al_2O_3/CuO interface changes enabling an effectively volumetric release of oxygen from the CuO inclusion. The oxygen flow may become greater than can directly participate in the heterogeneous reaction. This oxygen flow may result in mechanical disruption of the composite particles and in additional aluminum oxidation at any available exposed Al surfaces. Unfortunately, such processes cannot be described in the framework of the current heterogeneous reaction model; regardless, their onset is closely associated with an increase in the heterogeneous reaction described in the model.

Positions of the exothermic events predicted to occur in the nanocomposite material in reference to the pyrometer temperature are only slightly affected by selection of the thermal diffusivity. Thus, if the current results are interpreted in terms of predicting processes triggering rather than directly causing ignition, precise selection of the thermal diffusivity does not appear to be critical.

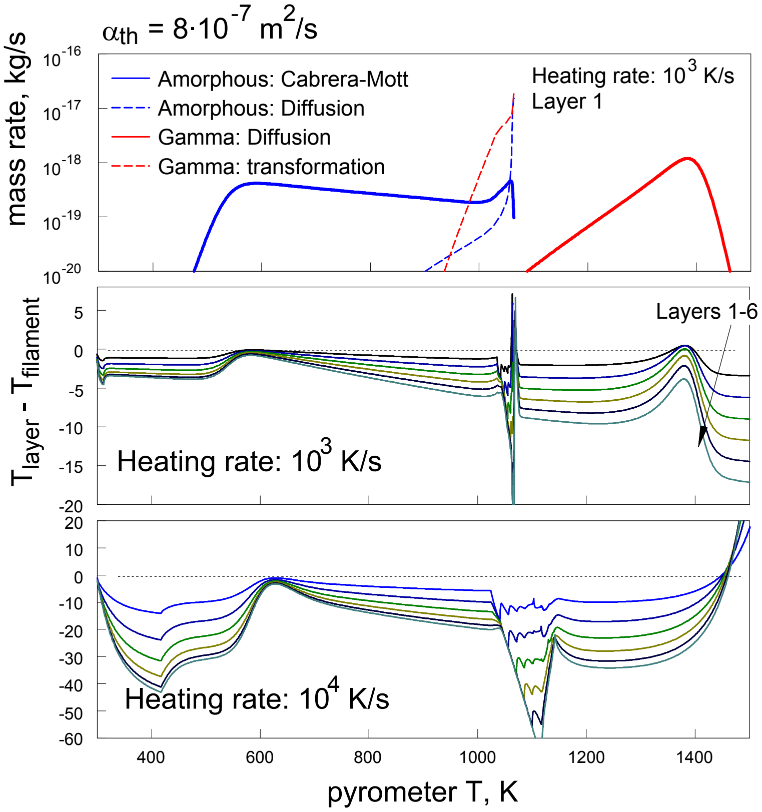

Figure 7.8 Mass growth rates of individual processes and calculated temperature differences between powder layers and filament at different heating rates using reference thermal diffusivity value.

7.5.2 Laser Ignition

For the laser ignition experiments, only the 8Al·3CuO was tested. This was the material used for initial laser ignition experiments and, as described below, the measured laser power required for ignition was very low. The stoichiometric composition is even more reactive, so we would be unable to accurately measure the laser power threshold required for ignition of that material. Therefore, experiments were limited to only the aluminum-rich composition.

The minimum laser beam power found to ignite the particles of 8Al·3CuO nanocomposite was 5.3 W. Photographs taken with an open camera aperture, 66 ms exposure time, showed that the ignited particles were exploded while being heated in the laser beam, as illustrated in Figure 7.9. This effect certainly cannot be explained by the heterogeneous reaction mechanisms developed in this paper; although, it further supports the earlier hypothesis of substantial role of oxygen release in ignition of the fully-dense Al-CuO nanocomposite materials.

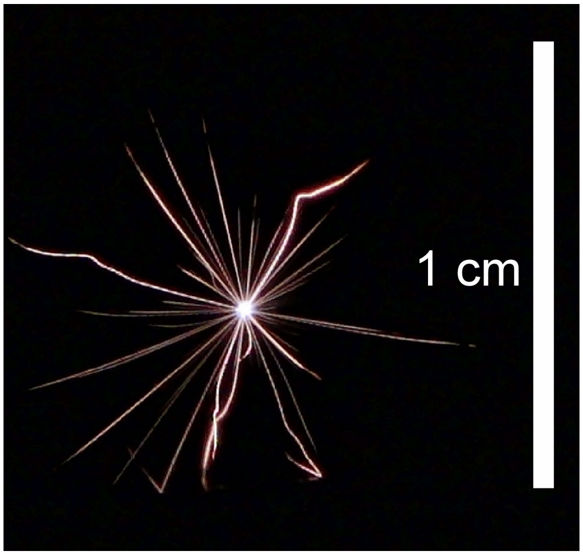

Figure 7.9 Open aperture photograph of 8Al·3CuO nanocomposite particles ignited in the CO_2 laser beam.

Figure 7.10 shows the results of calculations from the laser ignition model. Temperature profiles are shown for two laser powers. The dotted line was calculated using the experimentally determined threshold laser power, 5.3 W, which results in a very strong and sudden temperature increase. Also shown by the solid line, is the particle temperature history when the laser power is 4.3 W, the lowest value determined by the numerical model to give a strong temperature increase indicative of the particle ignition. Thus, the minimum laser power of 4.3 W predicted to cause ignition for individual composite particles is reasonably close to the experimental power of 5.3 W. Note that some variation in the particle absorption efficiency assumed to be the average value for pure Al and CuO, could shift the predicted minimum ignition threshold power slightly.

Heat flow terms for the chemical, convective, and laser radiation as well as the oxide mass growth rates are also shown in Figure 7.10 for the predicted laser power ignition threshold (4.3 W) case. Similar to the filament ignition results, the strong chemical heat release is due to the accelerating Cabrera-Mott and diffusive oxidation reactions. Unlike the filament ignition experiment, the accelerated heat release causes substantial increase in the particle temperature which can be directly interpreted as ignition. Clearly, as supported by Figure 7.9, gas release processes also occur and contribute to the ignition reactions.

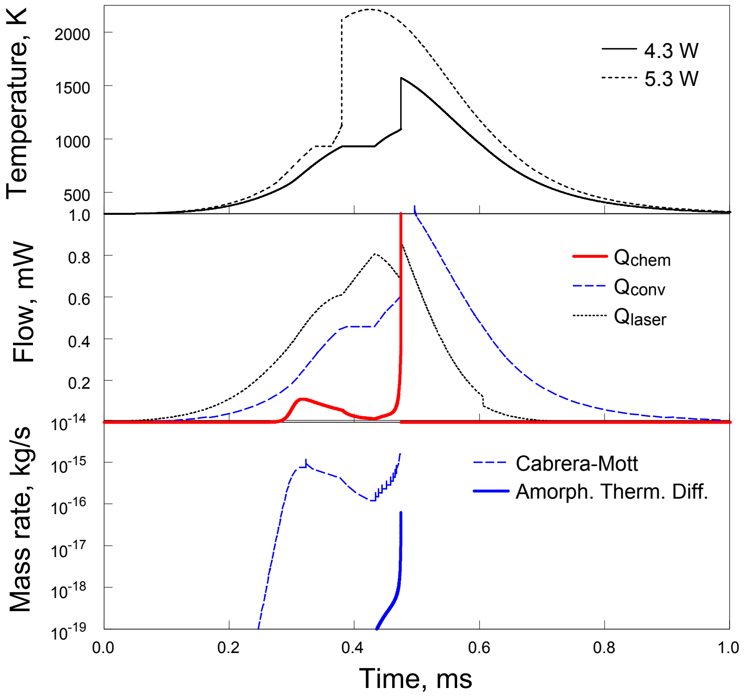

Figure 7.10 Calculated temperature and heat flow curves based on the laser ignition model.

7.6 Conclusions

A reaction model based on the Cabrera-Mott mechanism and describing the very early stages of redox reaction in fully-dense Al-CuO nanocomposite thermites prepared by arrested reaction milling is coupled with the multistep oxidation model describing diffusion controlled growth of amorphous and γ-Al_2O_3 polymorphs. Kinetic parameters of the multistep oxidation model obtained originally for reactions of aluminum with gaseous oxidizers are adjusted to describe the DSC traces measured for the fully-dense nanocomposite powders. The developed model of heterogeneous reactions in Al-CuO system is used to interpret results of ignition experiments with such materials using both powder coating on an electrically heated filament and individual particles ignited by the CO_2 laser beam. It is observed that the temperatures at which strong exothermic processes are predicted to occur in the nanocomposite materials correlate with the experimental ignition temperatures. However, for the heated filament ignition experiments, ignition as a thermal runaway is not predicted based on the considered heterogeneous reactions. Instead, it is proposed that such reactions should be considered as ignition triggers, while additional ensuing processes, such as oxygen release by decomposing CuO, contribute to additional heat release and temperature runaway in experiments. For the laser ignition experiments, a very strong temperature increase is predicted to occur as a result of exothermic reaction induced by the laser heating for the laser powers very close to those identified as an experimental ignition threshold. Particles ignited in the laser beam are observed to explode, further supporting the importance of additional gas release processes not included in the present model.

CHAPTER 8

CONCLUSIONS

Nanocomposite powders prepared by ARM were studied and found to have potential use in diverse applications such as burn rate modifiers and reactive structures and components. As presented in Chapter 2, $8Al{\cdot}MoO_3$ and $2B{\cdot}Ti$ nanocomposite powders were effective, as aluminum burn rate modifiers, in increasing both maximum pressure and rate of pressure rise when a relatively small addition of such modifier materials was made to micron-sized aluminum powder. The improvements in the burning were observed experimentally in oxygenated environments with hydrocarbon combustion products which would be found in practical applications.

Mechanical and physical properties of the ARM-prepared nanocomposite materials important for reactive structural materials were characterized in Chapter 3. Reactive nanocomposite powders prepared by ARM with bulk compositions $8Al{\cdot}3CuO$, $8Al{\cdot}MoO_3$ and $12Al{\cdot}MoO_3$ were successfully consolidated into reactive pellets with diameters varied from 0.25” to 0.5” and rectangular pellets with dimensions of 1.25”× 0.50”× 0.250”. Densities close to or exceeding 90% TMD were achieved while maintaining high reactivity of the consolidated samples. An increase in the tensile strength was achieved with addition of small amounts of binders. For $8Al{\cdot}MoO_3$, the highest density (~ 2.9 g/cm^3) and strongest (~ 17.5 MPa tensile strength) samples were obtained when indium was added as a binder and consolidation was performed at the temperature exceeding the melting point of indium. It was concluded that consolidation does not substantially alter the reactivity of the material as determined in a comparison of unconsolidated powders and respective pellets using DSC and XRD analysis.

Reactivity and ignition behavior of samples comprising consolidated $8Al \cdot MoO_3$ nanocomposite powder prepared by ARM was characterized in Chapter 4. The measured thermal diffusivity of consolidated samples was found to be a weak function of the pellet density. Pellets were ignited by a defocused CO_2 laser beam and the reaction was accompanied by pellet disintegration and violent combustion of the produced fragments. An experimental technique was developed to find ignition delay as a function of the laser power and pellet density. A numerical model was created to describe the heat transfer in the pellet and quantify the chemical reaction leading to its thermal initiation. Experimental ignition delays for different laser powers and pellet densities as well as the pellet temperatures prior to ignition were adequately described by the proposed thermal initiation model. The nanocomposite materials heated by laser ignited at a relatively low temperature, under 600 K.

Two types of nanocomposite reactive materials with the same bulk compositions $8Al \cdot MoO_3$ were compared to each other in Chapter 5. One of the materials was manufactured by mechanical milling (ARM) and the other by mixing of nano-scaled individual powders (MIC). Differences in the interfaces formed between Al and MoO_3 in materials prepared by different techniques resulted in differences in their low-temperature redox reactions well-detectable by DSC. Alternately, when these two types of materials were coated onto an electrically heated filament, their ignition temperatures were nearly identical to each other and were in the range of 750 – 800 K. The ignition delays were similar for the pellets of both materials prepared with the same porosity, and analysis of the heat transfer in the pellets heated by the laser suggested that the laser-exposed pellet surfaces are heated to approximately the same temperature before ignition for both materials. It was proposed that the ignition of both MIC and ARM-prepared materials at the same temperature can be explained by a thermodynamically driven transformation of a protective amorphous alumina into a crystalline polymorph.

Low temperature exothermic processes observed for ARM prepared materials in Chapter 5 were further explored in Chapter 6 for the Al-CuO system. Simultaneous processing of the experimental data from DSC and microcalorimetry enabled us to determine the parameters for the Cabrera-Mott reaction kinetics describing redox reaction in the nanocomposite Al-CuO thermite. The parameters determined enable one to describe the initial portions of the DSC curves (up to 600 K) measured at different heating rates as well as microcalorimetry traces recorded in the temperature range of 303 – 413 K. Furthermore, introduced reaction kinetics enables one to predict how such materials are aging at room or elevated temperatures.

In Chapter 7 a reaction model based on the Cabrera-Mott mechanism, developed in Chapter 6 and describing the very early stages of redox reaction in fully-dense Al-CuO nanocomposite thermites prepared by ARM, is coupled with the multistep oxidation model describing diffusion controlled growth of amorphous and γ-Al_2O_3 polymorphs. Kinetic parameters of the multistep oxidation model obtained originally for reactions of aluminum with gaseous oxidizers are adjusted to describe the DSC traces measured for the fully-dense nanocomposite powders. The developed model of heterogeneous reactions in Al-CuO system is used to interpret results of ignition experiments with such materials using both powder coating on an electrically heated filament and individual particles ignited by the CO_2 laser beam. It is observed that the temperatures at which strong exothermic processes are predicted to occur in the nanocomposite materials correlate with the experimental ignition temperatures. However, for the heated filament ignition experiments, ignition as a thermal runaway is not predicted based on the considered heterogeneous reactions. Instead, it is proposed that such reactions should be considered as ignition triggers, while additional ensuing processes, such as oxygen release by decomposing CuO, contribute to additional heat release and temperature runaway in experiments. For the laser ignition experiments, a very strong temperature increase is predicted to occur as a result of exothermic reaction induced by the laser heating for the laser powers very close to those identified as an experimental ignition threshold. Particles ignited in the laser beam are observed to explode, further supporting the importance of additional gas release processes not included in the present model.

APPENDIX A

EXTRA PELLET IGNITION RESULTS

This section contains additional results for the pellet ignition experiments.

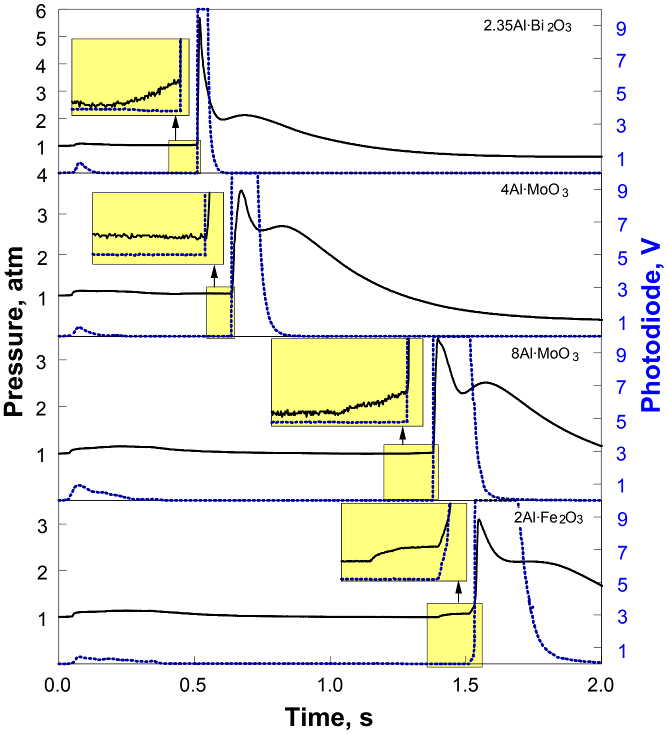

Figure A.1 Experimental results for pressure and photodiode signals measured for different pellet compositions.

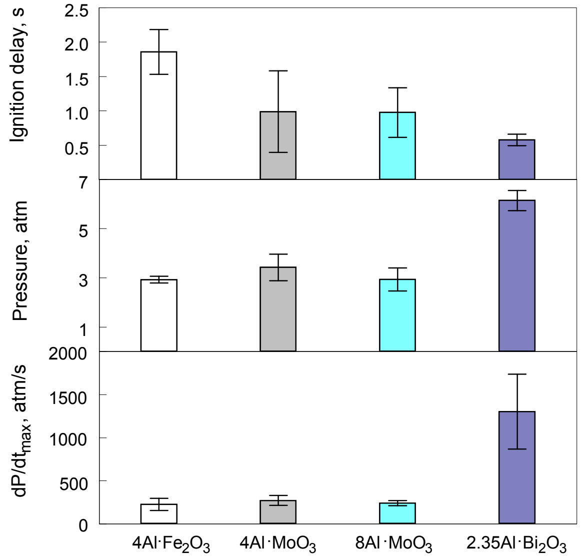

Figure A.2 Summary of measured ignition delays, maximum pressures, and rates of pressure rise for different pellet compositions.

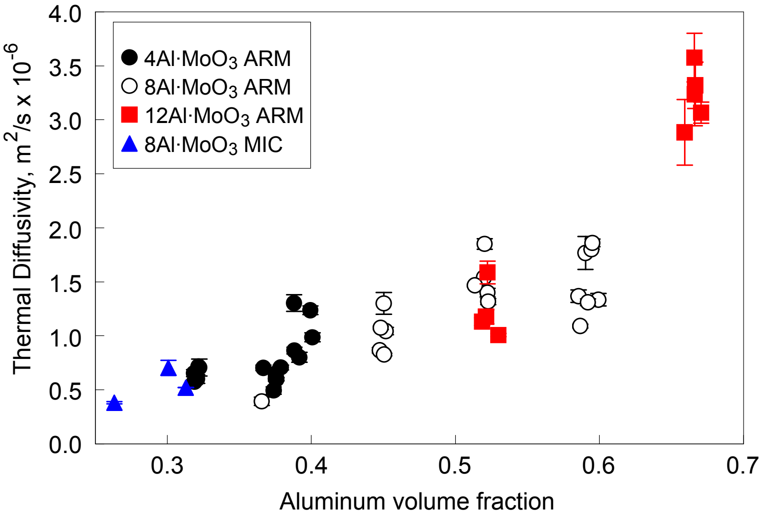

Figure A.3 Measured thermal diffusivity for different pellet compositions and pellet densities as a function of aluminum volume fraction per pellet.

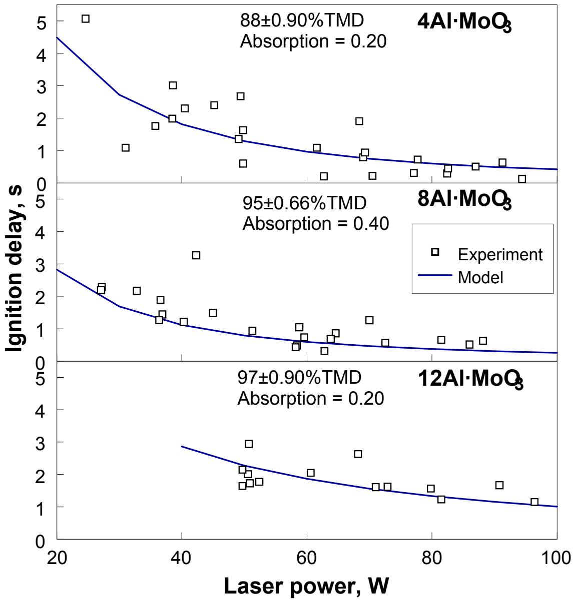

Figure A.4 Ignition delay vs. laser power for different compositions.

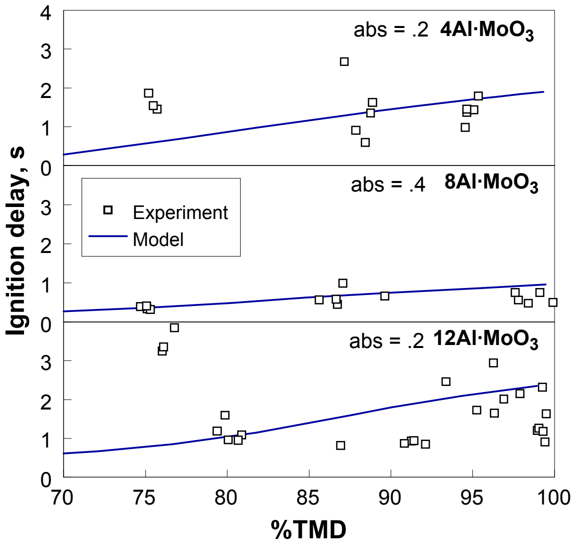

Figure A.5 Ignition delay vs. pellet density for different compositions. Applied laser power is 50 W.

APPENDIX B

CHARACTERIZATION OF AL-CUO MILLING REFINEMENT

In this appendix, characterization results for the Al-CuO materials prepared to achieve different degrees of refinement are shown.

Table B.1 Milling Conditions for 8Al·3CuO Prepared in Shaker Mill to Achieve Different Degrees of Refinement

	Time, min	PCA, mL	BPR
Sample 1	15	10	10
Sample 2	25	10	10

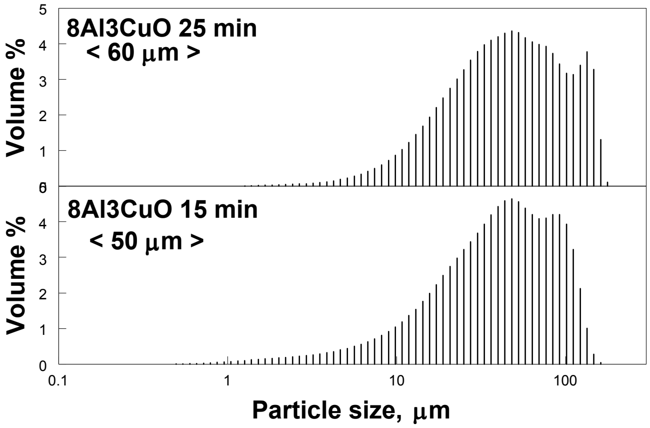

Figure B.1 Particle size distributions for the two samples with different milling conditions.

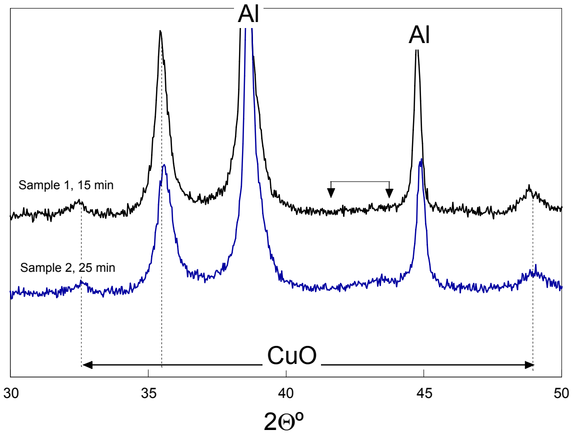

Figure B.2 XRD patterns for the two samples. The arrows between 40° and 45° show positions of where Cu would be.

APPENDIX C

ADDITIONAL WIRE IGNITION RESULTS

This appendix shows additional wire ignition experimental results for cases of fresh and aged material as well as different gas environments.

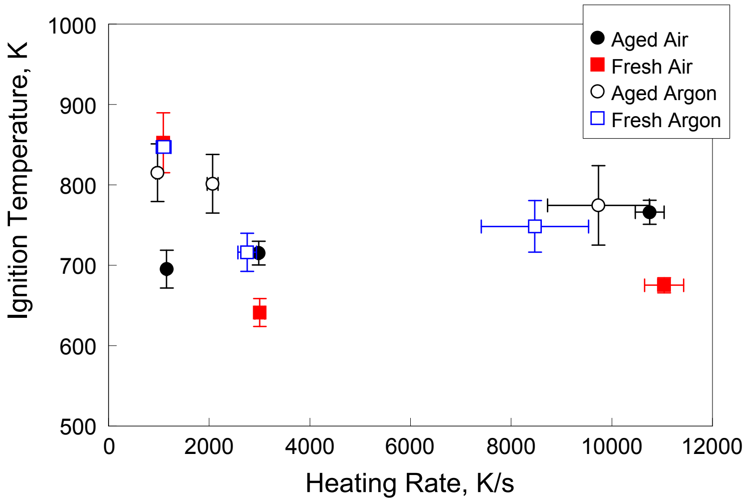

Figure C.1 Wire ignition results for 2Al·3CuO in different environments and for different sample ages.

APPENDIX D

PARTICLE COMBUSTION RESULTS

Results obtained for the processed data from the single particle laser ignition experiment.

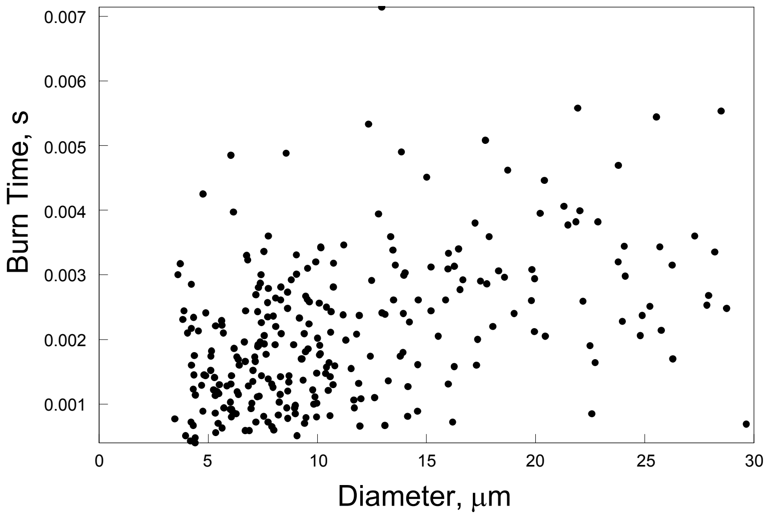

Figure D.1 Burn time of 8Al·3CuO (sample 2) particles as function of particle diameter. Processing performed 3-3-11.

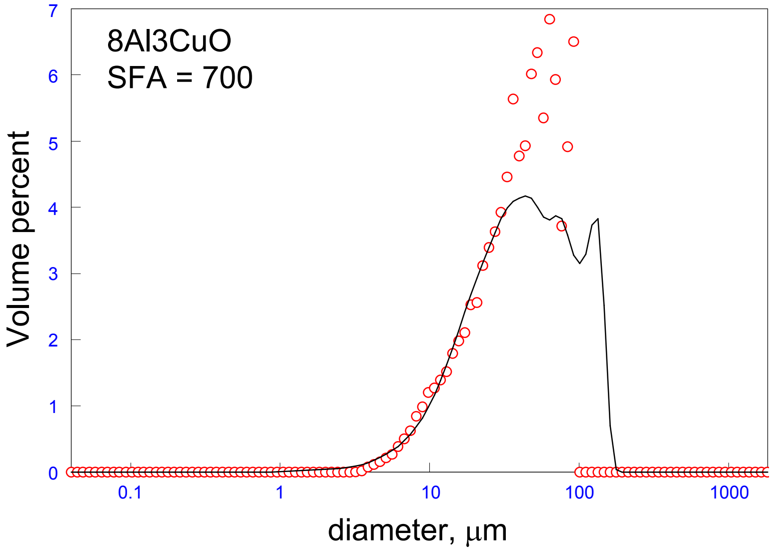

Figure D.2 Particle size distribution match between scattered signal and LALLS measurement.

APPENDIX E

ADDITIONAL TAM III MEASUREMENTS

TAM III measurements for the 8Al·MoO_3 nanocomposite are included in this section.

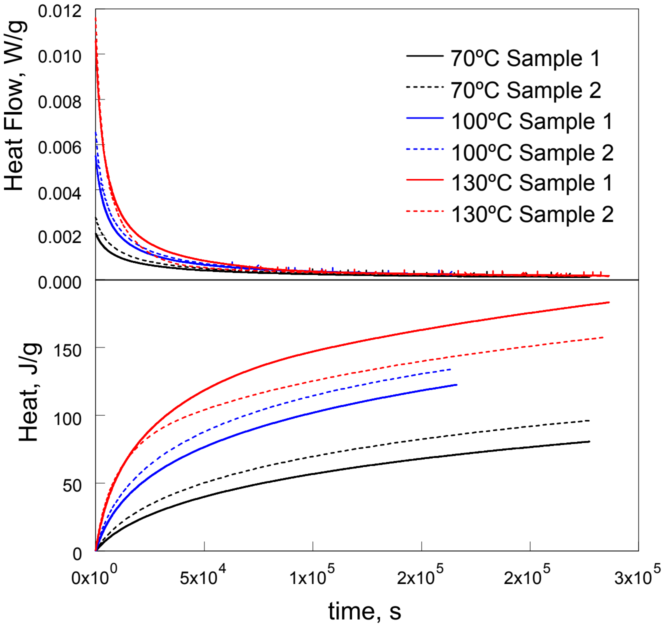

Figure 10 TAM III measurements for 8Al·MoO_3 prepared using two different milling parameters. Sample 1 is the more refined sample.

Table E.1 Measurement Dates for TAM III Samples

Temperature, ºC	Measurement Date
30	3-28-11 (no signal)
70	4-1-11
100	4-5-11
130	4-8-11

Samples 1 and 2 were both made 3-1-11 and stored under hexane in argon. Both were made in shaker mill using BPR 10 (10mm balls) with 10mL hexane and 5g powder load. Sample 1 was milled for 45 minutes while sample 2 was milled for 30 min.

APPENDIX F

CONTENTS ON DATA DISC

The data disc contains a copy of this dissertation as a PDF file as well as a WORD file. The front matter is contained in *Front_Matter.pdf* and the main body including appendices and reference is named *Main.pdf*. Also found on the disc, is a folder labeled *MATLAB Files* which contains additional folders labeled as *DSC Model*, *Laser Ignition Model*, *Wire Ignition Model*, and *Pellet Ignition Model*. These sub-folders contain the MATLAB functions for the DSC, wire ignition, laser ignition, and pellet ignition numerical models.

The WORD file is named *Main.doc* and includes all the figures embedded as PSIPLOT files.

REFERENCES

1. E.L. Dreizin, "Metal-based Reactive Nanomaterials," *Progress in Energy and Combustion Science*, 35, **2009**.
2. R.J. Jouet, J.R. Carney, R.H. Granholm, H.W. Sandusky, A.D. Warren, "Preparation and Reactivity Analysis of Novel Perfluoroalkyl Coated Aluminum Nanocomposites," *Material Science and Technology*, 22, 422, **2006**.
3. W.L. Perry, B.L. Smith, C.J. Bulian, J.R. Busse, C.S. Macomber, R.C. Dye, S.F. Son, "Nano-Scale Tungsten Oxides for metastable intermolecular Composites," *Propellants, Explosives, Pyrotechnics*, 29, 99, **2004**.
4. W.C. Danen, B.S. Jorgensen, J.R. Busse, M.J. Ferris, B.L. Smith, Los Alamos Nanoenergetic Metastable Intermolecular Composite (Super Thermite) Program, Abstracts of Papers, *221st ACS National Meeting*, CA, United States, April 1-5, **2001**.
5. S.F. Son, M.A. Hiskey, D.L. Naud, J.R. Busse, B.W., Asay, "Lead-Free Electric Matches," Proceedings of the 29th International Pyrotechnics Seminar, Defence Science and Technology Organisation, Pyrotechnics Group, **2002**.
6. A. Prakash, A.V. McCormick, M.R. Zachariah, "Synthesis and Reactivity of a Super-Reactive Metastable Intermolecular Composite Formulation of Al/$KmnO_4$," *Advanced Materials*, 17, 900, **2005**.
7. E.L. Dreizin, M. Schoenitz, *Nano-Composite Energetic Powders Prepared by Arrested Reactive Milling*, US Patent Application 20060053970, **2006**.
8. M. Schoenitz, T.S. Ward, E.L. Dreizin, "Fully Dense Nano-Composite Energetic Powders Prepared By Arrested Reactive Milling," *Proceedings of the Combustion Institute*, 30, 2071, **2005**.
9. S.M. Umbrajkar, M. Schoenitz, E.L. Dreizin, "Control of Structural Refinement and Composition in Al-MoO_3 Nanocomposites Prepared by Arrested Reactive Milling," *Propellants, Explosives, Pyrotechnics*, 31, 382, **2006**.
10. K.C. Walter, D.R., Pesiri, D.E. Wilson, "Manufacturing and Performance of Nanometric Al-MoO_3 Energetic Materials," *Journal of Propulsion and Power*, 23, 4, **2007**.
11. E.W. Price, "Combustion of Metallized Propellants," *Progress in Astronautics and Aeronautics*, 90, **1984**.
12. B. Palaszewski, L.S. Ianovski, P. Carrick, "Propellant technologies: Far-reaching Benefits for Aeronautical and Space-vehicle Propulsion," *Journal of Propulsion and Power*, 14, 5, **1998**.
13. F. Zhang, S.B. Murray, K.B. Gerrard, "Aluminum particles-air detonation at elevated pressures," *Shock Waves*, 15, 5, **2006**.

14. S.M. Umbrajkar, S. Seshadri, M.Schoenitz, V.K. Hoffmann, E.L. Dreizin, "Aluminum-Rich Al-MoO3 Nanocomposite Powders Prepared by Arrested Reactivie Milling," *Journal of Propulsion and Power*, 24, 192, **2008**.
15. M. Schoenitz, E.L. Dreizin, E. Shtessel, "Constant Volume Explosions of Aerosols of Metallic Mechanical Alloys and Powder Blends," *Journal of Propulsion and Power*, 19, 405, **2003**.
16. B.Z. Eapen, V.K. Hoffmann, M. Schoenitz, E.L. Dreizin, "Combustion of Aerosolized Spherical Aluminum Powders and Flakes in Air," *Combustion Science and Technology*, 176, **2004**.
17. M.A. Trunov, V.K. Hoffmann, M. Schoenitz, E.L. Dreizin, "Combustion of Boron-Titanium Nanocomposite Powders in Different Environments," *Journal of Propulsion and Power*, 24, 184, **2008**.
18. N.I. Poletaev, A.V. Florko, "Spectral Studies of the gas component of an aluminum dust flame: Condensed Phase," *Combustion, Explosion, and Shock Waves*, 44, 437, **2008**.
19. N.I. Poletaev, A.V. Florko, "Spectral Studies of the Gas Component of an Aluminum Dust Flame," *Combustion, Explosion, and Shock Waves*, 44, 437, **2008**.
20. A. Saigal, V.S. Joshi, "Strength and stiffness of aluminum/PTFE reactive composites," American Society of Mechanical Engineers, Pressure Vessels and Piping Division (Publication) PVP 432, **2000**.
21. W. Mock Jr., J.T. Drotar, "Effect of aluminium particle size on the impact initiation of pressed PTFE/Al composite RODS," *AIP Conference Proceedings*, 955, **2007**.
22. S.-Q. Yang, S.-L. Xu, T. Zhang, "Preparation and performance of PTFE/Al reactive materials," Guofang Keji Daxue Xuebao, *Journal of the National University of Defense and Technology*, 30, 62, **2008**.
23. J. Cai, S.M. Walley, R.J.A. Hunt, W.G. Proud, V.F. Nesterenko, M.A. Meyers, "High-strain, high-strain-rate flow and failure in PTFE/Al/W granular composites," *Material Science and Engineeringi A*, 427, **2008**.
24. J. Addiss, J. Cai, S. Walley, W. Proud, V.F. Nesterenko, "High strain and strain-rate behavior of PTFE/aluminum/tungsten mixtures," *AIP Conference Proceedings*, 955, **2007**.
25. E.B. Herbold, J. Cai, D.J. Benson, V.F. Nesterenko, "Simulation of particle size effect on dynamic properties and fracture of PTFE-W-Al composites," *AIP Conference Proceedings*, 955, **2007**.
26. S. Xu, S. Yang, P. Zhao, J. Li, F. Lu, "The study on the compressive behavior of PTFE/Al energetic composites," Lixue Xuebao, *Chinese Journal of Theoretical and Applied Mechanics*, 41, **2009**.

27. E.B. Herbold, V.F. Nesterenko, D.J. Benson, J. Cai, K.S. Vecchio, F. Jiang, J.W. Addiss, S.M. Walley, W.G. Proud, "Particle size effect on strength, failure, and shock behavior in poly-tetrafluoro-ethylene-Al-W granular composite materials," *Journal of Applied Physics*, 104, **2008.**

28. J.D. Kuntz, O.G. Cervantes, A.E. Gash, Z.A. Munir, "Tantalum-tungsten oxide thermite composites prepared by sol-gel synthesis and spark plasma sintering," *Combustion and Flame*, 157, **2010**.

29. B.W. White, N.N. Thadhani, J.L. Jordan, J.E. Spowart, "The effect of particle reinforcement on the dynamic deformation of epoxy-matrix composites," *AIP Conference Proceedings*, 1195, **2009**.

30. J.C. Trenkle, L.J. Koerner, M.W. Tate, S.M. Gruner, T.P. Weihs, T.C. Hufnagel, "Phase transformations during rapid heating of Al/Ni multilayer foils," *Applied Physics Letters*, 93, **2008**.

31. P.E. Specht, N.N. Thadhani, A. K. Stover, T.P. Weihs, "Meso-scale computational study of the shock-compression of cold-rolled Ni-Al laminates," *AIP Conference Proceedings*, 1195, **2009**.

32. D. Stamatis, Z. Jiang, V.K. Hoffmann, M. Schoenitz, E.L. Dreizin, "Fully dense, aluminum-rich Al-CuO nanocomposite powders for energetic formulations," *Combustion Science and Technology,* 181, **2009**.

33. M.W. Beckstead, "Overview of combustion mechanisms and flame structures for advanced solid propellants," in V. Yang, T.B. Brill, W.Z. Ren (Eds.), Solid Propellant Chemistry, Combustion, and Motor Interior Ballistics*, Progress in Astronautics and Aeronautics,* AIAA, 185, **2000**.

34. ASTM International, "Standard Test Method for Green Strength for Compacted Metal Powder Specimens," Designation: B 3133-95 (Re-approved 2002), **1996**.

35. J.L. Amoros, V. Cantavella, J.C. Jarque, C. Feliu, "Green Strength testing of pressed compacts: an analysis of the different methods," *Journal of the European Ceramic Society*, 28, **2008**.

36. P. Stanley, "Mechanical strength testing of compacted powders," *International Journal of Pharmaceutics*, 227, **2001**.

37. P. Jonsen, H.-A. Haggblad, K. Sommer, "Tensile strength and fracture energy of pressed metal powder by diametral compression test," *Powder Technology*, 176, **2007**.

38. P.J. Denny, "Compaction equations: a comparison of the Heckel and Kawakita equations," *Powder Technology*, 127, **2002**.

39. H. Abdoli, E. Salahi, H. Farnoush, K. Pourazrang, "Evolutions during synthesis of Al-AlN nanostructured composite powder prepared by mechanical alloying," *Journal of Alloys and Compounds*, 461, **2008**.

40. L.P. Martin, A.M. Hodge, G.H. Campbell, "Compaction behavior of uniaxially cold-pressed Bi-Ta composites," *Scripta Materialia*, 57, **2007**.

41. ASM International, Metals handbook, 10th ed., "Properties and Selection: Nonferrous Alloys and Special-Purpose Materials," 2, **1990**.

42. S.F. Yap, M.J. Adams, J.P.K. Seville, Z. Zhang, "Single and bulk compression of pharmaceutical excipients: evaluation of mechanical properties," *Powder Technology*, 185, **2008**.

43. D. Stamatis, P. Redner, E.L. Dreizin, "Preparation and characterization of consolidated samples of reactive nanocomposite materials," *Proceedings of the Central States Combustion Institute*, **2010**.

44. R.J. Lee, W. Mock Jr., J.R. Carney, W.H. Holt, G.I. Pangilinan, R.M. Gamache, J.M. Boteler, D.G. Bohl, J. Drotar, G.W. Lawrence, "Reactive Materials Studies," AIP *Conference Proceedings*, 845, **2006**.

45. J.D.E. White, R.V. Reeves, S.F. Son, A.S. Mukasyan, "Thermal explosion in Ni-Al system: Influence of mechanical activation," *Journal of Physical Chemistry A*, 113, **2009**.

46. L. Thiers, A.S. Mukasyan, A. Varma, "Thermal explosion in Ni-Al system: Influence of reaction medium microstructure," Combu*stion and Flame*, 131, **2002**.

47. A.Y., Dolgoborodov, M.N. Makhov, I.V. Kolbanev, A.N. Streletskii, V.E. Fortov, "Detonation in an aluminum-teflon mixture," *JETP Letters*, 81, **2005**.

48. A.Y., Dolgoborodov, M.N. Makhov, I.V. Kolbanev, A.N. Streletskii, V.E. Fortov, "Detonation in an aluminum-teflon mixture," *JETP Letters*, 81, **2005**.

49. K.W. Watson, M.L. Pantoya, V.I. Levitas, "Fast reactions with nano- and micrometers aluminum: A study on oxidation versus fluorination," *Combustion and Flame*, 155, **2008**.

50. D. Stamatis, X. Zhu, M. Schoenitz, E.L. Dreizin, P. Redner, "Consolidation and mechanical properties of reactive nanocomposite powders," *Powder Technology*, 208, **2011**.

51. W.J. Parker, R.J. Jenkins, C.P. Butler, G.L. Abbott, "Flash method of determining thermal diffusivity, heat capacity, and thermal conductivity," *Journal of Applied Physics*, 32, 9, **1961**.

52. NIST Chemistry WebBook., http://webbook.nist.gov/chemistry, **Feb. 2011**.

53. F.P. Incropera, D.P. DeWitt, "Fundamentals of Heat and Mass Transfer," John Wiley & Sons, **2002,** pp. 554-557.

54. T.S. Ward, M.A. Trunov, M. Schoenitz, E.L. Dreizin, "Experimental methodology and heat transfer model for identification of ignition kinetics of powdered fuels," *International Journal of Heat and Mass Transfer*, 49, **2006**.

55. M. Schoenitz, S. Umbrajkar, E.L. Dreizin, "Kinetic analysis of thermite reactions in Al-MoO_3 nanocomposites," *Journal of Propulsion and Power*, 23, **2007**.

56. K. Sullivan, M.R. Zachariah, "Simultaneous pressure and optical measurements of nanoaluminum thermites: Investigating the reaction mechanism," *Journal of Propulsion and Power*, 26, **2010**.

57. A. Ermoline, M. Schoenitz, E.L. Dreizin, “Reactions leading to ignition in fully dense nanocomposite Al-Oxide systems,” *Combustion and Flame*, 158, 6, **2011**.

58. A.L. Ramaswamy, P. Kaste, “A ‘Nanovision’ of the physiochemical phenomena occuring in nanoparticles of aluminum,” *Journal of Energetic Materials*, 23, 1, **2005**.

59. M.L. Pantoya, J.J. Granier, “The effect of slow heating rates on the reaction mechanisms of nano and micron composite thermite systems,” *Journal of Thermal Analysis and Calorimetry*, 85, 1, **2006**.

60. K.T. Higa, “Energetic nanocomposite lead-free electric primers,” *Journal of Propulsion and Power*, 23, 4, **2007**.

61. I. Levin, D. Brandon, “Metastable alumina polymorphs: crystal structures and transition sequences,” *Journal of the American Ceramic Society*, 81, 8, **1998**.

62. M.A. Trunov, S.M. Umbrajkar, M. Schoenitz, J.T. Mang, E.L. Dreizin, “Oxidation and Melting of Aluminum Nanopowders,” *Journal of Physical Chemistry B*, 110, 26, **2006**.

63. J. Sun, M.L. Pantoya, S.L. Simon, “Dependence of Size and Size Distribution on Reactivity of Aluminum Nanoparticles in Reactions with Oxygen and MoO_3,” *Thermochimica Acta*, 444, 2, **2006**.

64. M.A. Trunov, M. Schoenitz, X. Zhu, E.L. Dreizin, “Effect of Polymorphic Phase Transformations in Al_2O_3 Film on Oxidation Kinetics of Aluminum Powders,” *Combustion and Flame*, 140, 4, **2005**.

65. M. Schoenitz, B. Patel, O. Agboh, E.L. Dreizin, “Oxidation of Aluminum Powders at High Heating Rates,” *Thermochimica Acta*, 507-508, **2010**.

66. R.-H. Fan, H.-L. Lu, K.-N. Sun, W.-X. Wang, X.-B. Yi, “Kinetics of thermite reaction in Al-Fe_2O_3 system,” *Thermochimica Acta*, 440, 2, **2006**.

67. K.S. Martirosyan, L. Wang, D. Luss, “Novel nanoenergetic system based on iodine pentoxide,” *Chemical Physics Letters*, 481, 1-3, **2009**.

68. M.A. Trunov, M. Schoenitz, E.L. Dreizin, “Ignition of aluminum powders under different experimental conditions,” *Propellants, Explosives, Pyrotechnics*, 30, 1, **2005**.

69. M.A. Trunov, M. Schoenitz, E.L. Dreizin, “Effect of polymorphic phase transformations in alumina layer on ignition of aluminum particles,” *Combustion Theory and Modeling*, 10, 4, **2006**.

70. S.M. Umbrajkar, M. Schoenitz, E.L. Dreizin, “Exothermic Reactions in Al-CuO Nanocomposites,” *Thermochimica Acta*, 451, 1-2, **2006**.

71. S.M. Umbrajkar, C.-M. Chen, M. Schoenitz, E.L. Dreizin, “On problems of isoconversion data processing for reactions in Al-rich Al-MoO_3 thermites,” *Thermochimica Acta*, 477, 1-2, **2008**.

72. N. Cabrera, N.F. Mott, “Theory of the oxidation of metals,” *Reports on Progress in Physics*, 12, 1, **1949**.

73. L.P.H. Jeurgens, W.G. Sloof, F.D. Tichelaar, E.J. Mittemeijer, "Growth kinetics and mechanisms of aluminum-oxide films formed by thermal oxidation of aluminum," *Journal of Applied Physics*, 92, 3, **2002**.

74. Q. Fu, T. Wagner, "Interaction of nanostructured metal overlayers with oxide surfaces," *Surface Science Reports*, 62, 11, **2007**.

75. F. Reichel, L.P.H. Jeurgens, E.J. Mittemeijer, "The thermodynamic stability of amorphous oxide overgrowths on metals," *Acta Materialia*, 56, 3, **2008**.

76. J.A. Rodriguez, J.Y. Kim, J.C. Hanson, M. Perez, A.I. Frenkel, "Reduction of CuO in H_2: In situ time-resolved XRD studies," *Catalysis Letters*, 85, 3-4, **2003**.

77. A. Ermoline, E.L. Dreizin, "Equations for the Cabrera-Mott kinetics of oxidation for spherical nanoparticles," *Chemical Physics Letters*, 505, 1-3, **2011**.

78. S. Mohan, M.A. Trunov, E.L. Dreizin, "Heating and Ignition of Metallic Particles by a CO_2 laser," *Journal of Propulsion and Power*, 24, 2, **2008**.

79. S. Mohan, M.A. Trunov, E.L. Dreizin, "Heating and ignition of metal particles in the transition heat transfer regime," *Journal of Heat Transfer*, 130, 10, **2008**.

80. S. Vyazovkin, A.K. Burnham, J.M. Criado, L.A. Perez-Maqueda, C. Popescu, N. Sbirrazzuoli, "ICTAC Kinetics Committee recommendations for performing kinetic computations on thermal analysis data," *Thermochimica Acta*, 520, **2011**.

81. G. Daurelio, "Cutting copper sheets using CO_2 lasers," *Hyperfine Interactions*, 37, 1-4, **1987**.

82. L. Zhou, N. Piekiel, S. Chowdhury, M.R. Zachariah, "Time-resolved mass spectrometry of the exothermic reaction between nanoaluminum and metal oxides: The role of oxygen release," *Journal of Physical Chemistry C*, 114, 33, **2010**.

83. R. Zhou, X. Jiang, G. Lu, X. Zheng, "Desorption of Surface Oxygen on CuO/ZrO2-γ-Al_2O_3 and its influence on the Catalytic Performance," *Acta Physico-Chimica Sinica*, 13, 2, **1997**.

84. N.S. Torocheshnikov, A.N. Ketov, O.G. Mikulina, "Thermal Decomposition of Copper Oxide in a Nitrogen Stream," *Zhurnal Vsesoyuznogo Khimicheskogo Obshchestva*, 11, 1, **1966**. (Russian)